



Horizon 2020  
Programme

***METIS***

*Research and Innovation Action (RIA)*

This project has received funding from the European  
Union's Horizon 2020 research and innovation programme  
under grant agreement No 945121

Start date : 2020-09-01 Duration : 48 Months

---

**Methodology for site specific rockhazard consistent record**

---

Authors : Mrs. Marianne GROS (LGI), Sipicic Nevena IUSS Pavia; García de Quevedo Inarritu Pablo IUSS Pavia,  
Alvarez-Sanchez Luis IUSS Pavia, Kohrangi Mohsen Bazzurro Paolo

METIS - Contract Number: 945121

Project officer: Katerina PTACKOVA

Document title	Methodology for site specific rockhazard consistent record
Author(s)	Mrs. Marianne GROS, Sipcic Nevena IUSS Pavia; García de Quevedo Inarritu Pablo IUSS Pavia, Alvarez-Sanchez Luis IUSS Pavia, Kohrangi Mohsen Bazzurro Paolo
Number of pages	67
Document type	Deliverable
Work Package	WP5
Document number	D5.1
Issued by	LGI
Date of completion	2022-09-21 17:56:51
Dissemination level	Public

---

**Summary**

The work presented herein is a part of WP5, which focuses on a selection of earthquake ground motion record sets consistent with the hazard at the site of interest, as estimated by WP4. The provided suites of records will then be used in WP6 to estimate the structural response and derive fragility functions of systems, structures and components (SSCs) of nuclear power plants (NPPs). This report describes the state-of-the-art record selection methods, which ensure that the chosen ground motions have similar characteristics to those that may be experienced by the SSCs during their lifetime. This consistency is a crucial requirement for the development of adequate fragility functions. These methods range from more straightforward spectral-quantity-based approaches, such as the conditional mean spectrum...

---

**Approval**

Date	By
2022-09-21 17:57:18	Mrs. Paolo BAZZURRO (IUSS)
2022-09-21 17:57:48	Dr. Irmela ZENTNER (EDF)



# METIS

Seismic Risk Assessment  
for Nuclear Safety

Research & Innovation Action

NFRP-2019-2020

## **Methodology for site-specific rock-hazard-consistent record selection for mainshock-only seismicity**

### **Deliverable D5.1**

Version N°2

Authors:

**Šipčić Nevena**

**García de Quevedo Iñarritu Pablo**

**Alvarez-Sanchez Luis**

**Kohrangi Mohsen**

**Bazzurro Paolo**



## Disclaimer

The content of this deliverable reflects only the authors' view. The European Commission is not responsible for any use that may be made of the information it contains.





## Document Information

Grant agreement	945121
Project title	Methods And Tools Innovations For Seismic Risk Assessment
Project acronym	METIS
Project coordinator	Dr. Irmela Zentner, EDF
Project duration	1 <sup>st</sup> September 2020 – 31 <sup>st</sup> August 2024 (48 months)
Related work package	WP5 - Ground motion selection for engineering analyses, including site response
Related task(s)	Task 5.1 - Methodology for site-specific rock-hazard-consistent record selection for mainshock-only seismicity
Lead organisation	IUSS
Contributing partner(s)	EDF, NTUA, IRSN, GFZ, GRI, GEM
Due date	30 <sup>th</sup> April 2022
Submission date	5 <sup>th</sup> September 2022
Dissemination level	

## History

Version	Submitted by	Reviewed by	Date	Comments
N°1	Paolo Bazzurro	Dimitrios Vamvatsikos	29/08/2022	
		Irmela Zentner	21/06/2022	
N°2	Paolo Bazzurro		08/09/2022	



# Table of Contents

1.	Definition of ground motion “site-specific rock-hazard-consistency” for mainshock-only seismicity	11
1.1.	CMS and CS .....	12
1.2.	Generalized Conditional Intensity Measure (GCIM) .....	13
1.3.	Conditional spectra faithful to causative parameters (CS-MR) .....	14
1.4.	Record selection and IM choice.....	15
1.5.	Record selection for multi-directional analysis .....	17
2.	Recorded and synthetic ground motions for engineering analyses .....	20
2.1.	Database of real motions.....	20
2.2.	Database of synthetic motions .....	23
2.2.1.	Stochastic ground motion simulation methodology (SGMSM).....	23
2.2.2.	Calibration of the SGMSM.....	23
2.2.3.	Generation of a simulated database.....	27
2.3.	Identification of rock ground motions .....	28
2.3.1.	Reference Site Classification Methods .....	28
2.3.2.	Complex Method .....	28
2.3.3.	Pilz’s Method .....	29
2.3.4.	Rock ground motions .....	31
3.	Selection procedure of hazard-consistent ground motions.....	33
3.1.	Soil and rock ground motions for CS-based hazard .....	37
3.1.1.	Record sets and selection.....	37
3.1.2.	Structural Response to CS based hazard consistent records .....	38
3.1.3.	Structural Response to pairwise rock-soil ground motion records.....	43
3.1.4.	Seismological parameter tests .....	44
3.2.	Scaled ground motions for CS-based hazard .....	48
3.2.1.	Record sets and selection.....	48
3.2.2.	Structural response to CS-based hazard consistent records .....	48
3.2.3.	Seismological tests .....	50
3.2.4.	Hazard consistent record selection accounting for duration and Arias intensity .....	52
3.3.	Synthetic ground motions for CS-based hazard .....	55
3.3.1.	Record sets and selection.....	55
3.3.2.	Distribution of IMs .....	57
3.3.3.	Structural Response.....	59
4.	Conclusions and recommendations .....	62
5.	Acknowledgments .....	63

6. Bibliography.....	63
----------------------	----

## List of figures

Figure 1: WP5 in the METIS workflow .....	10
Figure 2: Conditional distribution of (a) $S_a$ and (b) $D_{5-75}$ , conditioned on $S_a(1s)$ obtained using the GCIM method .....	14
Figure 3: Mean of the target and sample distribution using: (a) $CS[S_a(1.5s)]$ and (b) $CS[AvgS_a(0.2:0.1:2.0s)]$ .....	17
Figure 4: Illustration of the CS record sets used for the analysis of the 3-story building excerpted from Kohrangi et al. (2019). Top: target CS and ground motion response spectra; Middle: target and candidate match mean CS; Bottom: target and candidate match standard deviation .....	19
Figure 5: Schematic structure of the MAT file that contains all considered ground motions.....	21
Figure 6: Map of epicenters of the earthquakes included in the assembled dataset, color-coded based on the original databases.....	21
Figure 7: – Distribution of (a) magnitude, (b) $V_{s30}$ and (c) Joyner and Boore distance. Vertical dashed line refers to the median values. ....	22
Figure 8: Comparison of reference and simulated ground motion features for scenarios inside the calibration for group with $5 < M_w \leq 6$ , $R_{hypocentral} \leq 50 \text{ km}$ and $V_{s30} \geq 600 \text{ m/s}$ . (a) Moment magnitude ( $M_w$ ), (b) – Hypocentral distance ( $R_{hypocentral}$ ), (c) – Hypocentral depth ( $Z$ ), and (d) - $V_{s30}$ .....	25
Figure 9: Comparison of reference and simulated distributions of the IMs of interest considered during the calibration process of scenarios for group with $5 < M_w \leq 6$ , $R_{hypocentral} \leq 50 \text{ km}$ and $V_{s30} \geq 600 \text{ m/s}$ . (a) – Geometric mean of the horizontal response spectra, (b) – Geometrical mean of the horizontal Husid durations, (c) – Geometrical mean of the horizontal AI, (d) – Response spectra of the vertical component, and (e) Comparison of time histories for one of the scenarios replicated scenarios ( $M_w = 5.90$ , $R_{hypocentral} = 41.78 \text{ km}$ , $Z = 7.50 \text{ km}$ , $V_{s30} = 1100 \text{ m/s}$ ) .....	26
Figure 10: Comparison of the Magnitude and site hypocentral distance for (a) – ESM and (b) – SDB. (c) – Comparison of the ESM and SDB response spectra of the GM component for all scenarios (individual spectra are shown in light grey) , and (d) – Distribution of the $V_{s30}$ characterizing the scenarios in each database .....	27
Figure 11: Distribution of considered stations. Stations fulfilling all reference-site criteria outlined in the text are shown as red dots. Green dots represent additional reference site identified through machine learning. Black dots represent all analysed stations while yellow dots indicate stations for which fewer than 10 events with sufficient SNR have been recorded. Brown colour represents rock conditions from a surface geologic map while soft soils are shown in ochre. Hachures indicate the chronostratigraphic era.....	31
Figure 12: Magnitude distance distribution (left) and full response spectra (right) .....	32
Figure 13: (a) location of the site used as case study and (b) rock hazard curves for different IMs ....	34
Figure 14: Hazard disaggregation at site for the ten $S_a(1.0s)$ levels.....	34
Figure 15: Material models of the SDOF systems .....	35
Figure 16: comparison (a) $SSE_s$ test, and (b) spectral shape for AvgSa-based CS selection of rock and soil records .....	38

Figure 17: Scale factor for <i>AvgSa</i> -based <i>CS</i> -consistent soil and rock ground motions at the 10 <i>IMLs</i>	38
Figure 18: Ductility response of SDOF systems	39
Figure 19: Peak acceleration response of SDOF systems	40
Figure 20: Peak velocity response of SDOF systems	40
Figure 21: Hysteretic energy response of SDOF systems	41
Figure 22: Duration distribution of (a) selected records and (b) full database	41
Figure 23: Spectral shape for different durations	42
Figure 24: Fragility functions for DS1 ( $\mu \geq 2$ ) and DS2 ( $\mu \geq 8$ ) for <i>AvgSa</i> (Top) and <i>Sa(T1)</i> (Bottom)..	43
Figure 25: Spectral matching of rock and soil motions	44
Figure 26: Ratios of soil to rock responses measured by maximum drift, acceleration, velocity and dissipated energy computed using the pairwise record analyses	44
Figure 27: Magnitude-distance scattergram of the causative earthquakes of the four record sets, colours indicate IM level	45
Figure 28: <i>Vs30</i> distribution for the selected record sets arranged by <i>IML</i>	46
Figure 29: Distribution of different <i>IMs</i> , namely peak ground acceleration ( <i>PGA</i> ), Husid duration, Cumulative absolute velocity ( <i>CAV</i> ), Arias intensity ( <i>AI</i> ), and Spectral intensity ( <i>SI</i> ), from first to the last row, respectively, in terms of median and standard deviation for the case of <i>AvgSa</i> .....	47
Figure 30: <i>SSEs</i> for the (a) LSF and (b) HSF records sets for different conditioning periods	48
Figure 31: Results of nonlinear time history analysis using 40 selected records at each <i>IML</i> , for the LSF and HSF sets of ground motions. Median (solid line) and 5 <sup>th</sup> and 95 <sup>th</sup> percentiles (dashed lines) are illustrated for different EDPs: (a) max ductility, (b) max acceleration, (c) max velocity, and (d) hysteretic energy.	49
Figure 32: Comparison between the fragility curves obtained from LSF (solid line) and HSF (dashed line) groups for three different ductility levels and SDOF with: (a) $T_1=0.2s$ , (b) $T_1=1s$ and (c) $T_1=2s$ . Label on the x axis refers to <i>Sa</i> [g] at the fundamental period of the corresponding SDOF system.	50
Figure 33: Distribution of <i>MW</i> , <i>Vs30</i> and <i>Rjb</i> in terms of median and standard deviation for the case of $T_1=1s$ .	51
Figure 34: Distribution of different <i>IMs</i> , namely peak ground acceleration ( <i>PGA</i> ), Husid duration, Cumulative absolute velocity ( <i>CAV</i> ), Arias intensity ( <i>AI</i> ), and Spectral intensity ( <i>SI</i> ), from first to the last row, respectively, in terms of median and standard deviation for the case of $T=1s$ .	52
Figure 35: <i>SSEs</i> for the (a) LSF and (b) HSF records sets, selected using the modified <i>CS</i> that accounts for <i>AI</i> (i.e., <i>CS(AI)</i> ), for different conditioning periods	53
Figure 36: Comparison between the fragility curves obtained from LSF (green line) and HSF (grey line) groups using <i>CS</i> and <i>CSAI</i> for ductility levels of: (a) $\mu=2$ , (b) $\mu=5$ and (c) $\mu=8$ . Label on the x axis refers to <i>Sa</i> [g] at the fundamental period of the corresponding SDOF system, i.e., <i>Sa(T1 = 0.2s)</i> .	53
Figure 37: Comparison between the fragility curves obtained from LSF (green line) and HSF (grey line) groups using <i>CS</i> and <i>CSAI</i> for ductility levels of: (a) $\mu=2$ , (b) $\mu=5$ and (c) $\mu=8$ . Label on the x axis refers to <i>Sa</i> [g] at the fundamental period of the corresponding SDOF system, i.e., <i>Sa(T1 = 1s)</i> .	54



Figure 38: Comparison between the fragility curves obtained from LSF (green line) and HSF (grey line) groups using <i>CS</i> and <i>CSD</i> for ductility levels of: (a) $\mu=2$ , (b) $\mu=5$ and (c) $\mu=8$ . Label on the x axis refers to $S_a$ [g] at the fundamental period of the corresponding SDOF system, i.e., $S_a(T_1 = 2s)$ . .....	54
Figure 39: $SSE_s$ error for the LSF and HSF records sets and different conditioning periods .....	55
Figure 40: Distribution of $M_w$ , $V_{s30}$ and $R_{jb}$ in terms of median and standard deviation for the case of $T=0.2s$ .....	56
Figure 41: Distribution of $M_w$ , $V_{s30}$ and $R_{jb}$ in terms of median and standard deviation for the case of $T=1.0s$ .....	57
Figure 42: Distribution of different IMs, namely peak ground acceleration (PGA), Husid duration, Cumulative absolute velocity (CAV), Arias intensity (AI), and Spectral intensity (SI), from first to the last row, respectively, in terms of median and standard deviation for the case of $T=1s$ . .....	58
Figure 43: Distribution of different IMs, namely peak ground acceleration (PGA), Husid duration, Cumulative absolute velocity (CAV), Arias intensity (AI), and Spectral intensity (SI), from first to the last row, respectively, in terms of median and standard deviation for the case of $T=2s$ . .....	59
Figure 44: Results of nonlinear time history analysis using 40 selected records at each IML, for the ESM and SDB sets of ground motions. Median is illustrated for different EDPs: (a) max ductility, (b) max acceleration, (c) max velocity, and (d) hysteretic energy. The dashed lines represent the 5 <sup>th</sup> and 95 <sup>th</sup> percentiles of the distributions.....	60
Figure 45: Comparison between the fragility curves for three SDOFs obtained from ESM and SDB-selected records for: (a) $\mu \geq 2$ , (b) $\mu \geq 5$ and (c) $\mu \geq 8$ . Label on the x axis refers to $S_a$ [g] at the fundamental period of the corresponding SDOF system. Solid and dashed lines refer to the curves computed with the response from records selected from the ESM and SDB databases, respectively. ....	61

## List of tables

Table 2: Number of records and analysed sites for each data set considered. ....	30
Table 3: Values of the four <i>IMs</i> , , $S_a(0.2s)$ , , $S_a(1s)$ and , $S_a(2s)$ and , $AvgS_a(0.2:0.1:2)$ , at the 10 poe levels at the Perugia site. <i>IML</i> 4 corresponds to the 10% in 50 years level (i.e., 475 yr return period, which is used for design. ....	33
Table 4: Numerical models summary .....	36

## Abbreviations and Acronyms

Acronym	Description
AI	Arias intensity
CAV	Cumulative absolute velocity
CMS	Conditional mean spectrum
CS	Conditional spectrum
D <sub>5-75</sub>	5-75% significant duration
D <sub>5-95</sub>	5-95% significant duration
EDP	Engineering demand parameter
GCIM	Generalized conditional intensity measure
GMPE	Ground motion prediction equation
IM	Intensity measure
IML	Intensity level
MAF	Mean annual frequency
NLTHA	Nonlinear time history analysis
NPP	Nuclear power plant
PBEE	Performance based earthquake engineering
PGA	Peak ground acceleration
PGV	Peak ground velocity
poe	Probability of exceedance
PSHA	Probabilistic seismic hazard analysis
Rjb	Joyner and Boore distance
Rrup	Rupture distance
S <sub>a</sub>	Spectral acceleration
SDOF	Single degree of freedom
SSE	Sum of squared errors
SSC	Systems, structures and components
UHS	Uniform hazard spectrum
V <sub>s30</sub>	Average shear wave velocity in the upper 30m
WP	Work package
HSF	High Scaling Factor
LSF	Low Scaling Factor

## Summary

The work presented herein is a part of WP5, which focuses on a selection of earthquake ground motion record sets consistent with the hazard at the site of interest, as estimated by WP4 and adequate for structural response analysis, performed by WP6. The provided suites of records will then be used in WP6 to estimate the structural response and derive fragility functions of systems, structures and components (SSCs) of nuclear power plants (NPPs). This report describes the state-of-the-art record selection methods, which ensure that the chosen ground motions have similar characteristics to those that may be experienced by the SSCs during their lifetime, considering the extreme scenarios that they need to withstand. This consistency is a crucial requirement for the development of adequate fragility functions. These methods range from more straightforward spectral-quantity-based approaches, such as the conditional mean spectrum (*CMS*) and the conditional spectra (*CS*) with its variants (e.g., *CS – MR*, which is more faithful to causative parameters of the earthquakes contributing the most to the site hazard) to more complex procedures, such as the generalized intensity measure (*GCIM*) approach. Herein, we also delve into the applicability of these methods investigating different scalar and vector ground motion Intensity Measures (*IMs*) as the hinge between seismic hazard and fragility function computation and we consider multi-directional record selection. Furthermore, we describe the assembly of a uniform database of ground motions built from aggregating different databases available worldwide that encompass a wide array of intensities and causative parameters. We also describe the construction of a simulated database, consistent with a reference database of recorded ground motions in terms of causative parameters and median spectral content. Lastly, this document addresses some long-standing issues vexing the selection of ground motion records for fragility analysis, namely the adequacy of a) mixing accelerograms recorded both on soil and rock conditions, b) scaling real records to replace missing ground motions having naturally high intensity measures, and c) using synthetic ground motions in lieu of real ones. To this goal, we carried out a battery of tests to evaluate the structural response of a set of SDOF systems with different hysteretic models and fundamental periods to various groups of hazard consistent records, selected using the *CS* method. The results show no significant statistical differences in seismological characteristics and structural responses for SDOF systems tested (i.e. SDOF systems modeled with two hysteretic force-displacement behaviors, namely the pinching model with cyclic and in-cycle degradation, and the (non-degrading) elastic-hardening model) as long as hazard consistency is accurately enforced in the ground motion record selection. Fragility curves obtained showed a slight bias for some groups at the highest damage levels, caused mainly due to lack of sufficiency of certain *IMs* and suboptimal matching of the target spectra at high *IML*.

## Keywords

Hazard consistency, record selection, rock site identification, soil ground motions, scaling, simulated ground motions.

## Introduction

Performance-Based Earthquake Engineering (PBEE) (Cornell & Krawinkler, 2000) focuses on the probabilistic assessment of the performance of structures subjected to earthquakes and separates the contributions from seismic hazard analysis and structural analysis. Within this framework, the seismic hazard at a site is defined by the Mean Annual Frequency (*MAF*) of exceeding certain levels of a conditioning ground motion Intensity Measure (*IM*) from all seismic scenarios that contribute to the hazard. This procedure is usually referred to as Probabilistic Seismic Hazard Analysis, or PSHA (e.g., McGuire, 2004). The structural response assessment is traditionally communicated via sets of fragility functions for different limit states that are conditioned on an *IM* value. To derive fragility curves, it is common to perform nonlinear time history analysis (*NLTHA*) using selected sets of ground motions. Such record sets should be statistically consistent to the motions that the structure may experience at the site in its intended lifetime. Loosely, speaking, this is referred to as “hazard consistency” (Lin et al., 2013). To ensure hazard consistency, sets of records should be carefully selected to avoid inaccurate or biased fragility curves, and in turn, risk estimates (Kohrangi et al., 2017).

The objective of WP5 in the METIS project is to ensure that hazard consistency is attained by selecting appropriate ground motions representative of the hazard at the site on rock conditions in accordance with the outputs of WP4. This results in the unbiased and robust estimation of fragility curves (WP6) tailored for the given site.

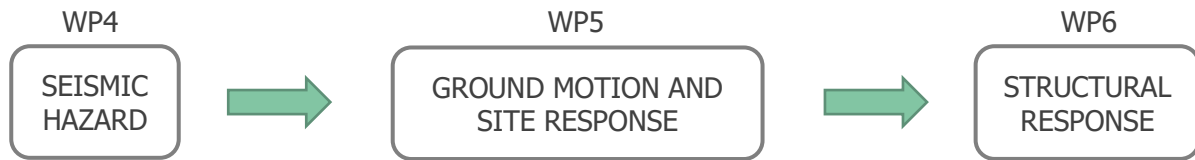


**Figure 1: WP5 in the METIS workflow**

Within this report, Section 1 describes the state-of-the-art methods for selecting hazard-consistent ground motions, addressing some of their critical aspects. For the time being, we focus only on mainshock events with no account of clustered seismicity. In Section 2, we collect the available waveforms from multiple worldwide repositories to compile a single large database of ground motion recordings. Additionally, we assemble the database of synthetic ground motions using the stochastic ground motion simulation methodology, fully described in Alvarez et al. (2022b) and proposed as part of WP4. After devising and carrying out a battery of engineering and seismological tests, in Section 3 these databases are then used to assess the adequacy of employing for structural fragility computations (a) ground motions recorded on soil sites in lieu of those recorded on rock, (b) ground motions scaled in amplitude, and (c) synthetic ground motions rather than recorded ones.



# 1. Definition of ground motion “site-specific rock-hazard-consistency” for mainshock-only seismicity

Record selection is critical in the seismic risk assessment process as it links the hazard to the structural analysis. The response of a structure to three-component ground motions depends, in general, on many characteristics of the motions, such as Peak Ground Acceleration (*PGA*) and Velocity (*PGV*), spectral content, Arias Intensity (*AI*), Cumulative Absolute Velocity (*CAV*), and significant duration (*D*). Regardless of the complex behaviour of the shaking, the link with the hazard is left, in the great majority of cases, to one single *IM* and seldom to a vector of *IMs*. PSHA then computes the site hazard in terms of that *IM* (or *IMs*) and the structural engineers use that *IM* (or *IMs*) to compute the probability of exceedance of the limit state, should different levels of that *IM* (or *IMs*) be experienced at the structure's site. This computation leads to the development of fragility curves (or surfaces) for the structure under consideration. The issue is that other characteristics of the ground motion (e.g., duration) in addition to the selected *IM*(or *IMs*) affect the said probability of exceedance, given a level of *IM*, but those characteristics are usually neither monitored nor enforced when ground motion records are selected to be used for fragility curve (or surface) computations. The result of neglecting the effect of all the other *IMs* besides the chosen one(s) is that the structural response can be biased by an amount and direction that the analyst cannot know a priori. The methodologies presented here intend to obviate this bias problem. To obtain robust, unbiased fragility curves, it is necessary to select hazard-consistent sets of records for the site and SSCs of interest. However, what is meant in practice by hazard consistency of an *IM* or group of *IMs* and how to achieve it is rather unclear and clarifying these issues is the main objective of this report.

In current practice, we can identify two approaches for selecting hazard-consistent records: a) the scenario-based approach and b) the target-spectrum-based approach.

The scenario-based methods are those in which ground motions are selected simply based on the causative parameters obtained through PSHA disaggregation (Bazzurro & Cornell, 1999). Such parameters include (but are not limited to) magnitude (*M*), source-to-site distance (*R*) and epsilon ( $\epsilon$ ) (i.e., the number of standard deviations that the ground motion for the given causative scenario is away from the median, see Baker & Cornell, 2006), for a given *IM* level (Stewart et al., 2001). Selecting records through this method works under the assumption that the distribution of all the *IMs* that affect the structural response are well represented in the selected set of ground motions simply based on the consistency of the *M*, *R*,  $\epsilon$  of the events that generated those records and those identified by the PSHA disaggregation. This assumption may be met if one had at one's disposal a very large (infinite, in the limit) number of records from all the *M*, *R*,  $\epsilon$  scenarios of interest and if one had time and resources to compute the response of the structure for all those records. Otherwise, if one uses a practical number of records this assumption may be met just by luck, a consideration that makes this method unacceptable for our purposes.

In the target-based selection approach (Baker, 2011; Bradley, 2010; Jayaram et al., 2011), on the other hand, the chosen ground motion suites must match a target distribution of *IMs*, such as spectral ordinates, duration, *AI*, or any other *IM* of interest.

Traditionally, records were often selected such that their response spectra matched, within some tolerance, a target Uniform Hazard Spectrum (UHS) from PSHA with often little regard to the causative *M* and *R* parameters. This method, however, can lead to conservative estimates since the contribution of myriad events generates it and, therefore, it is an envelope of the spectral accelerations of a given annual probability of exceedance that, in general, cannot be caused by any single event. This method, which has been used to check the structural fitness of existing structures or for design purposes, is not recommended for risk analysis. To support probabilistic risk calculations, significant advances have been made in recent years, and methods such as the Conditional Mean Spectrum (*CMS*) (Baker, 2011) and, more comprehensively, the Conditional Spectrum (*CS*) (Jayaram et al., 2011) were proposed. These

methods enforce hazard consistency only for spectral quantities, such as spectral accelerations. However, it was recognized that in some cases, characteristics beyond the spectral shape, e.g., duration, could be relevant to the structure's response. This consideration led to the development of the Generalized Conditional Intensity Measure (*GCIM*) approach (Bradley, 2010), which is simply a generalization of the *CS* to include other *IMs* that are not spectral quantities. More recently, Spillatura et al. (2021) proposed a *CS – MR* method, which offers a simple approach to account for metrics that depend on *M – R* implicitly (e.g., duration, Arias intensity) but are not captured in the response spectra.

In the following sub-sections, we describe these methods in more detail.

## 1.1. CMS and CS

As explained in the previous section, the *CMS* and *CS* were derived as alternative target spectra to the UHS in recognition that the short-period and the long-period parts of the spectrum were likely caused by very different earthquakes. Forcing ground motions from a single scenario to “match” the entire UHS would not be defensible for risk computations where conservatism should not be included. The former alternative method, the *CMS*, considers only the mean acceleration response spectrum for a given scenario event (e.g., magnitude, rupture-to-site distance, and fault mechanism) conditional on the occurrence of a spectral acceleration at a period of interest,  $S_a(T^*)$ , of a given value while the latter, the *CS*, accounts also for the variability of spectral accelerations at periods other than  $T^*$ .

The steps that are followed to compute the target spectrum and select a set of records consistent with it are:

1. Perform PSHA for a site (including local soil conditions) and *IM* of choice; this step may involve the use of one or more Ground Motion Prediction Equations (GMPEs);
2. Perform disaggregation to identify the event characteristics most contributing to the mean hazard;
3. Calculate the target spectrum for the given scenario (or, better, the multitude of scenarios that contribute to the mean hazard);
4. Select a set of records that match the target.

The first step involves the selection of the conditioning period, which depends on the structure and the type of assessment one wants to perform. More details about the *IM* choice will be given in Section 1.4. The PSHA provides the value of  $S_a(T^*)$  at any given return period of interest and disaggregation provides the earthquake scenarios that are more likely to cause the occurrence of that value of  $S_a(T^*)$  at the site. One can either choose one scenario from the disaggregation (e.g., mean or mode) or account for the contribution of all scenarios (Lin et al., 2013a). Once the scenario is determined, the logarithmic mean and standard deviation (in case of *CS*) of the spectral acceleration at the period  $T_i$ , conditioned on the  $\ln S_a(T^*)$  are estimated as follows:

$$\mu_{\ln S_a(T_i) | \ln S_a(T^*)} = \mu_{\ln S_a(T_i)} + \rho(T_i, T^*) \varepsilon(T^*) \sigma_{\ln S_a(T_i)} \quad (1)$$

$$\sigma_{\ln S_a(T_i) | \ln S_a(T^*)} = \sigma_{\ln S_a(T_i)} \sqrt{1 - \rho^2(T_i, T^*)} \quad (2)$$

Where  $\mu_{\ln S_a(T_i)}$  and  $\sigma_{\ln S_a(T_i)}$  are estimated using the selected GMPE,  $\varepsilon(T^*)$  represents the number of standard deviations that the ground motion for the given causative scenario is away from the (log) mean of  $S_a(T^*)$  and  $\rho(T_i, T^*)$  is the correlation coefficient between  $\ln S_a(T_i)$  and  $\ln S_a(T^*)$  which can be estimated, for instance, as explained in Baker & Jayaram (2008). Once the target is derived, we can use a simulation approach to select the set of suitable records (step 4). By suitable, we refer to a set of records that collectively matches, within some tolerance, the mean target spectrum (in the case of the *CMS*) or the mean target spectrum and the dispersion around it (in the case of the *CS*). Once the record set is selected, one can use a so-called “greedy” optimization technique to improve the match (Jayaram et al., 2011). This technique involves an iterative evaluation of all the initially selected records and a search in the entire record database for replacements, which are retained only if they improve the match between the selected suite and the target spectrum.

To quantify the misfit of the final set of records, we can use the sum of squared errors ( $SSE_s$ ) metric (Baker & Lee, 2018):

$$SSE_s = \sum_{k=1}^p \left[ (m_{lnIM_k} - \mu_{lnIM_k})^2 + w(s_{lnIM_k} - \sigma_{lnIM_k})^2 \right] \quad (3)$$

Where  $m_{lnIM_k}$  is the sample mean of  $lnIM_k$  and  $s_{lnIM_k}$  is the sample standard deviation of  $lnIM_k$  values of the selected motions. The quantities  $\mu_{lnIM_k}$  and  $\sigma_{lnIM_k}$  are the target conditional means and standard deviations,  $p$  is the number of periods of interest, and  $w$  is a weight factor that assigns relative importance to the mismatches in the mean versus standard deviation values.

## 1.2. Generalized Conditional Intensity Measure (GCIM)

The aforementioned *CMS* and *CS* methods used for hazard consistent records selection enforce the hazard consistency in terms of spectral accelerations, which are, by definition, representing the peak response of elastic SDOFs of specific oscillation periods. Other features of ground motions (e.g., duration, *AI*, *CAV*, energy) are not explicitly accounted for, while they could conditionally affect the structural response in some cases. To overcome these limitations, (Bradley, 2010) proposed the *GCIM* approach that accounts for the distribution of any ground motion intensity measure (e.g., *PGA*, *PGV*, *CAV*,  $S_a$ ) identified as potential good predictors of seismic response. A vector of *IMs* can be expressed as:

$$\mathbf{IM} = \{IM_1, IM_2 \dots IM_{N_{IM}}\} \quad (4)$$

Similar to *CMS* and *CS*, a conditioning intensity measure  $IM_j$  is chosen, followed by the construction of the target distribution of the  $\mathbf{IM}|IM_j$ , which is commonly, but not necessarily, assumed to have a multivariate lognormal distribution. The conditional distribution of a single intensity measure  $IM_i$ , given  $IM_j = im_j$ , can be calculated using the total probability theorem as follows:

$$f_{IM_i|IM_j} = \sum_{k=1}^{N_{rup}} f_{IM_i|Rup_k,IM_j} P_{Rup_k|IM_j} \quad (5)$$

Where  $f_{IM_i|Rup_k,IM_j}$  is the probability density function (pdf) of  $IM_i$  given  $Rup = rup_k$  and  $IM_j = im_j$ , while  $P_{Rup_k|IM_j}$  is the probability that the ground motion with  $IM_j = im_j$  is caused by  $k^{th}$  rupture.

From the assumption that the distribution of  $\mathbf{IM}|IM_j$  follows a multivariate lognormal distribution (Jayaram & Baker, 2008), it is implied that conditional distribution  $f_{IM_i|Rup_k,IM_j}$ , for each  $IM_i$  in  $\mathbf{IM}$ , follows a univariate lognormal distribution:

$$f_{IM_i|Rup_k,IM_j} \sim LN(\mu_{lnIM_i|Rup,IM_j}, \sigma_{lnIM_i|Rup,IM_j}^2) \quad (6)$$

Parameters of this distribution, i.e., mean  $\mu_{lnIM_i|Rup,IM_j}$  and variance  $\sigma_{lnIM_i|Rup,IM_j}^2$  for every  $IM_i$  of interest can be found using the appropriate GMPEs and a correlation coefficient between intensity measures  $IM_i$  and the conditioning intensity measure  $IM_j$  ( $\rho_{lnIM_i,lnIM_j}$ ). The quantity  $P_{Rup_k|IM_j}$  can be found from seismic hazard disaggregation results for the site of interest. Using the equations above, one can derive the conditional distributions for different *IMs* of interest. Theoretically, any vector of *IMs* can be used in this procedure; however, one should keep in mind practical constraints in terms of the availability of GMPEs and correlation coefficients for different combinations of *IMs*, which may not be readily available.

Using the methodology described above, we developed Python scripts that can be used to derive the target distribution using  $S_a$  ordinates and Significant duration ( $D$ ) as of *IMs* interest. As conditioning *IM*, the  $S_a$  at any period can be used. If other *IMs* are relevant for assessing the response of a particular SSC and a variance-covariance matrix were not be available, one would need to be derived from empirical data.

## D5.1 Methodology for selecting ensembles of rock-hazard consistent ground motions for fragility curve computations and datasets for WP6

For the sake of illustration, we carried out a record selection for a site in Perugia, Central Italy, with  $V_{s30} = 800$  m/s and an intensity level corresponding to 10% probability of exceeding (poe) in 50 years. (Boore & Atkinson, 2008) and (Afshari & Stewart, 2016) GMPEs are used for  $S_a$  and  $D_{5-75}$ , respectively, and  $S_a(1s)$  is chosen as conditioning  $IM$ . Empirical equations to predict the correlation coefficients between  $S_a(T)$  and the conditioning  $S_a(1s)$  are based on the model of (Baker & Jayaram, 2008), while those to predict the correlation coefficients between  $D_{5-75}$  and the conditioning  $S_a(1s)$  are taken from (Bradley, 2011).

Once the target distribution is derived, to select a set of suitable records we use a simulation approach, similar to those described for  $CMS$  and  $CS$ . In the particular case, we selected the set of 25 records and evaluated its adequacy to represent the target distribution using the  $SSE_s$  metric of Equation (3). Figure 2 illustrates the target and sample distributions of acceleration response spectra and  $D_{5-75}$ . It can be seen that the selected set represents well the  $GCIM$  distribution, which implies that, in cases when characteristics other than spectral shape are relevant for the response of the structure of interest, a proposed record selection methodology that utilizes the  $GCIM$  approach is a suitable alternative.

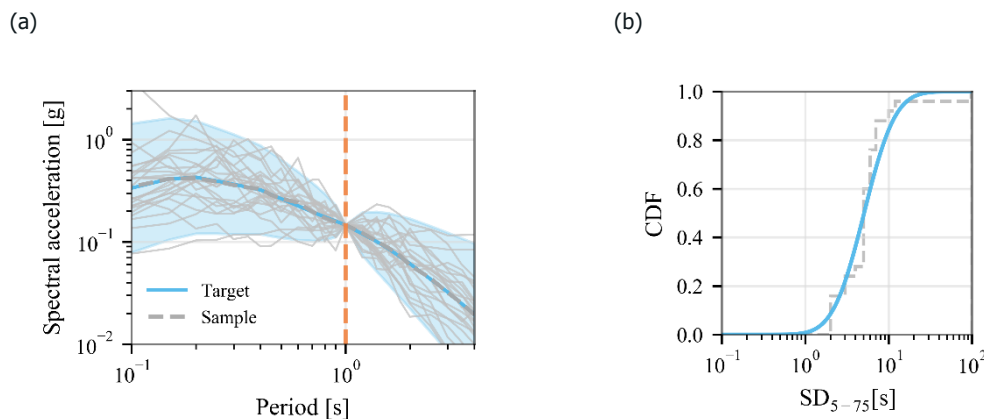


**Figure 2: Conditional distribution of (a)  $S_a$  and (b)  $D_{5-75}$ , conditioned on  $S_a(1s)$  obtained using the  $GCIM$  method**

### 1.3. Conditional spectra faithful to causative parameters (CS-MR)

As discussed above, when enforcing the hazard consistency of the spectral quantities is not sufficient, the  $GCIM$  method can be applied. However, its application requires that the engineer knows a priori which  $IMs$  other than the spectral quantities are good response predictors and deserve to be made hazard consistent when selecting ground motion records. An improvement in terms of hazard consistency was proposed by Tarbali & Bradley (2016), which constrained the ground motion database in terms of the possible  $M$ ,  $R$  and site conditions before performing selection using  $GCIM$ . The main drawback of this and similar works is that the overall  $M - R$  distribution obtained from the hazard disaggregation cannot be captured. A more recent method, the  $CS - MR$  proposed by Spillatura et al. (2021) seeks to implicitly enforce the consistency of any such  $IMs$  by selecting records whose response spectra not only match the target  $CS$  but also are faithful to the  $M - R$  distribution extracted from hazard disaggregation. During the selection, the percentage of ground motions from a given  $M - R$  bin chosen to match the target  $CS$  is consistent with the percentage of the contribution to the hazard from the same  $M - R$  bin. For example, if 40 ground motions are sought to match a  $S_a(T)$ -based  $CS$  and the contribution to the occurrence of that  $S_a(T)$  level is 20% from  $M - R$  bin 1, 50% from bin 2 and the remaining 30% from bin 3, then the algorithm will pick 8, 20 and 12 records from bins 1, 2 and 3, respectively.

Although arguably less precise than  $GCIM$  because the hazard consistency of  $IMs$ , other than for spectral quantities, is not explicitly enforced, the proposed method is conceptually simpler and more intuitive. Moreover,  $CS - MR$  has some additional advantages to  $GCIM$ . Firstly,  $CS - MR$  discards records from

earthquake scenarios that are unlikely to strike the site. Hence, the ensemble of response spectra does not only match the target distribution of spectral ordinates, but also the selected spectra are, one by one, more representative of the ground motions that may be occurring at the site. Secondly, *CS – MR* has the advantage over *GCIM* of not needing the ex-ante knowledge of which other *IMs* may be important for predicting the structural response. In addition, the *GCIM* method requires the analyst to assign weights to the *IMs* whose distributions should be made hazard consistent, an operation that is inherently arbitrary and, therefore, questionable. All other *IMs* are accounted for implicitly and more naturally by the *CS – MR* method without the need to assign weights.

However, using the *CS – MR* method is not without issues. First and foremost, the limited number of records available in some *M – R* bins may result in selected records whose hazard consistency is only approximately met. This issue is, of course, less prevalent when *CS – only* is used, or any other target-based selection method, as the restrictions of imposing causative parameters are less strict.

All things considered, this method may provide a good balance of consistency, in both spectral shape and causative parameters, with the target distributions. This can help keep valuable information in the ground motion selection that would otherwise be missed.

## 1.4. Record selection and IM choice

The connection between hazard and structural response within a PBEE framework is conducted by selecting sets of records whose *IM* distribution matches that prescribed by the conditioning *IM* defined in the PSHA. This procedure, however, assumes that the structure's response is accurately predicted by the conditioning *IM* and that all the other *IMs* have, conditionally speaking, a much lower importance in affecting the severity of the engineering demand parameters (EDPs). This is often not the case for most types of structures and also different *IMs* may be good predictors for different EDPs. Therefore, selecting an appropriate *IM* will directly affect the record selection procedure and, consequently, the development of the ensuing fragility curves and, in the end, the outcome of the seismic risk assessment. Ideally, the selected *IM* should be efficient and sufficient (Luco & Cornell, 2007). An *IM* is deemed to be efficient when the dispersion of an EDP given that *IM* is small, whereas an *IM* is deemed to be sufficient when the impact on the EDP of any *IM* other than the conditioning one is negligible (Kohrangi et al., 2016). Several authors have looked at the efficiency and sufficiency of different *IMs* in the prediction of the response of different types of structural systems. For example, the spectral acceleration at the first period of vibration,  $S_a(T_1)$  has been observed to be sufficient and efficient for predicting the response of first-mode dominated low-rise buildings not experiencing extensive damage. However, the sufficiency of this conditioning *IM* drops when considering structures whose response is either affected by higher vibration modes or is way beyond the onset of damage such that the vibration period “elongates” significantly (Shome & Cornell, 1999).

Considering the fact that no single *IM* is, strictly speaking, both efficient and sufficient in predicting different EDPs describing the structural response of complex models, researchers have considered combinations of different *IMs* in vectorial fashion. The extension of the scalar case requires the computation of a vector-valued PSHA (i.e., VPSHA) (Bazzurro & Cornell, 2002) to compute the joint hazard probability distributions of the *IMs* in the considered vector. This procedure is computationally more demanding than the scalar *IM* case but, in general, is superior in the prediction of EDPs than any of the typical scalar *IMs* or of more complex *IMs* defined as a combination of scalar *IMs* as shown by many authors (Bojórquez & Iervolino, 2011; Cordova et al., 2000; De Biasio et al., 2014; Kazantzi & Vamvatsikos, 2015; Kohrangi et al., 2016). Since using vector *IMs* comes at a price that, in many cases, is arguably higher than the benefits obtained by a more accurate EDP prediction, some authors have proposed a well-crafted scalar *IM* that is a reasonably good predictor for all the considered EDPs both in the quasi-linear response domain and close to collapse, although not necessarily the best one in estimating any one of them. The average spectral acceleration ( $AvgS_a$ ), is one such candidate.  $AvgS_a$  is the mean of the log spectral accelerations at a set of vibration periods of interest that typically are chosen to span from  $0.2T^*$  to  $1.5T^*$ , where  $T^*$  is the fundamental period of the structure, thus accounting for the influence of higher modes and the period elongation caused by response nonlinearities, usually noted as  $AvgS_a(0.2T^*:\text{step}:1.5T^*)$ , where “step” is the constant interval in seconds between subsequent periods used for averaging the logs of the spectral ordinates. Kohrangi et al. (2017) details the use of  $AvgS_a$  for record selection, like the one shown in Figure 3b, using a modified





version of the algorithm proposed by Jayaram et al. (2011), and performs a set of tests to compare the performance of various building models using  $CS(Sa(T))$  at different periods and  $CS(AvgS_a)$ . That study lists some of the advantages and disadvantages of considering  $AvgS_a$  as conditioning  $IM$ :

- ▶ Since  $CS(AvgS_a)$  is a compromise between multiple CS targets conditioned at several periods, the spectral content of the selected records is neither very aggressive nor benign at any period range, removing any possible inaccuracies or bias, which could be present for periods far from the conditioning period when records are chosen based on  $CS(Sa(T))$  as shown in Kohrangi et al. (2017).
- ▶  $CS(AvgS_a)$  provides records with a moderate conditional variability across a wide range of periods, while  $CS(Sa(T))$  provides zero variability of the spectral acceleration at the anchoring period and increasing higher values at all other periods as moving away from the conditioning one. Thus, the target spectrum is less restrictive for  $CS(AvgS_a)$  making it easier to find hazard consistent records from a limited catalogue.
- ▶  $AvgS_a$  will give an overall smaller variability on the EDPs for nonlinear response, but it will typically increase the variability for elastic first-mode dominated response relative to  $Sa(T_1)$ , where  $T_1$  is the first-mode period. This may become an issue for NPPs, which are elastic, although not necessarily dominated by any particular mode as typical low-rise buildings.
- ▶ Normally, the dispersion in the GMPE obtained from  $AvgS_a$  is lower than that on any of the  $Sa(T)$ , which can be beneficial for risk assessment.
- ▶ Conditioning the response on a single  $IM$  and at a given intensity level using  $Sa(T)$  can cause events that are particularly intense to that  $IM$  to be weighted more and dominate the hazard, while events that would dominate the hazard for other types of intensity are weighted less. This issue was mentioned in (Bradley, 2013). On the contrary, since  $AvgS_a$  considers a wider array of periods, it gives a better representation of those other events without favouring events with a large epsilon at a particular period.

$CS(AvgS_a)$  can give well-balanced estimates when assessing losses since results both in terms of peak floor acceleration (PFA) and inter-story drift ratio (IDR) have been observed to be reasonably close to those given by  $CS(Sa(T))$  at the most relevant period (typically longer for IDR, shorter for PFA). Contrarily, single period estimations tend to favor one over another, either underestimating some responses or providing conservative estimates. Based on these findings, we can speculate that using  $CS(AvgS_a)$ -based record selection can also be advantageous when one intends to assess the fitness for purpose of a structure for multiple limit states (e.g., serviceability and ultimate) without changing the conditioning period. On the other hand, it has mainly been tested on nonlinear multi-story buildings, which do not conform to the NPP paradigm of elastic response and multiple important eigenfrequencies. Whether it will offer good performance in this case as well is something that remains to be seen.

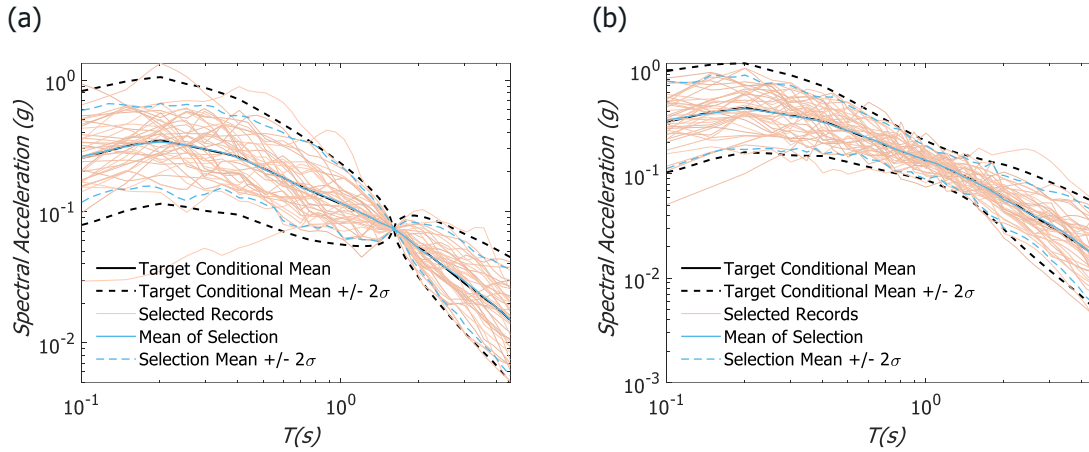


**Figure 3: Mean of the target and sample distribution using: (a) CS[Sa(1.5s)] and (b) CS[AvgSa(0.2:0.1:2.0s)] (i.e., average spectral acceleration in the 0.2s to 2.0s range computed at steps of 0.1s). Both distributions are derived for the site of Perugia and intensity level corresponding to 5% poe in 50 years. 40 records are selected.**

## 1.5. Record selection for multi-directional analysis

When one needs to analyze 3D structural models, it is intuitive that record selection procedures described in the previous sections need be extended in a way that utilizes information from the three components of the ground motion.

In the literature, most extensions developed so far address the two horizontal components of the ground motion. To our knowledge, the most comprehensive such study is the one recently performed by Kohrangi et al. (2019). They presented several methodologies of different complexities that can be used to select the records for bi-directional analysis in a hazard-consistent way using either *CS* for vector *IMs* (as explained in the previous sub-section) or different variants of *CS* for a scalar *IM*. A brief description of the methods considered is given below:

1.  $CS[S_{a,g.m}(\bar{T})]$   
Records are selected and scaled to match the target spectrum of the geometric mean of the spectral accelerations of two components; this is general practice
2.  $CS[S_{ax}(T_{1x})] - R$  or  $CS[S_{ay}(T_{1y})] - R$   
Records are selected and scaled to match the target conditional spectrum of one of the two components. The other component is inherited and used **regardless** of its spectral shape hazard consistency;
3.  $CS[S_{ax}(T_{1x})] - C$  or  $CS[S_{ay}(T_{1y})] - C$   
Records are selected and scaled to match the target conditional spectrum of both components, considering the correlation of the spectral accelerations in the two orthogonal directions. Therefore, the spectral shapes at both components are **compatible** with the hazard.
4.  $CS\{S_{ax}(T_{1x}), S_{ay}(T_{1y})\}$   
A vector *IM* consisting of spectral accelerations at the first modal periods of the structure in the *x* and *y* axes of the building of the horizontal components of the ground motion. Records are selected and scaled to match the target conditional spectra of both components considering the correlation of the spectral accelerations in the two orthogonal directions;
5.  $CS\{AvgS_{ax}, AvgS_{ay}\}$   
A vector *IM*, consisting of accelerations averaged in a period range extracted from arbitrary components of the ground motion. Records are selected and scaled to match the target

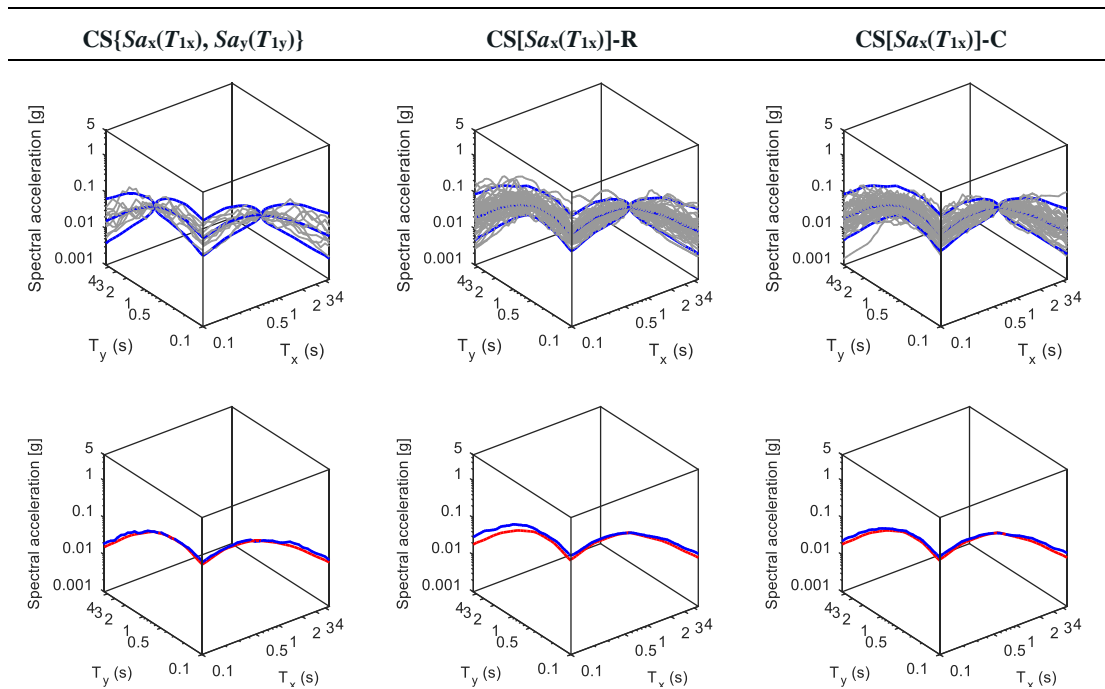
conditional spectra of both components considering the correlation of the spectral accelerations in the two orthogonal directions;

Using the above-listed variants of record selection and five case study buildings, Kohrangi et al. (2019) selected 50 ground motion pairs for six intensity levels and compared the results in terms of mean annual frequency (MAF) of exceeding specific engineering demand parameter thresholds. They showed that as long as the hazard consistency is ensured in both directions, it is not relevant if vector or scalar IMs are utilized because the results obtained using the CS variants 1, 3, 4 and 5 above are, in most cases, statistically indistinguishable.

However, it should be noted that doing record selection using a vector of IMs as conditioning variables (i.e., Options 4 and 5) might not be the very practical as (i) the risk assessment requires assessing the hazard in vectorial form via VPSHA (possible via VPSHA approach), ii) vector fragility needs to be computed, and (iii) it is sometimes challenging to select records to match the target spectrum conditioned on two *IMs*. When a scalar *IM* is used, on the other hand, we have three viable options:

- Use the geometric mean of the two horizontal components calculated at the mean of the fundamental periods in the two directions (Option 1). This might be the preferable approach as it does not require any changes in the original *CS* method. However, it is not recommended to use it for structures whose fundamental periods in the two horizontal directions are significantly different;
- Use an *IM* of only one component but ensure the hazard consistency for the *IM* of the other component as well (Option 3);
- Use *CS*-regardless (Option 2) but only when the building is expected to be significantly weaker in one direction and limit states are expected to be reached because of damage caused by the ground motion along that direction.

As an example, Figure 4 illustrates the bi-directional ground motions selected for a three-story building with fundamental periods of  $T_{1x} = 0.57s$  and  $T_{1y} = 0.66s$  via the three *CS* variants corresponding to Options 4, 2 and 3, from left to right, respectively.





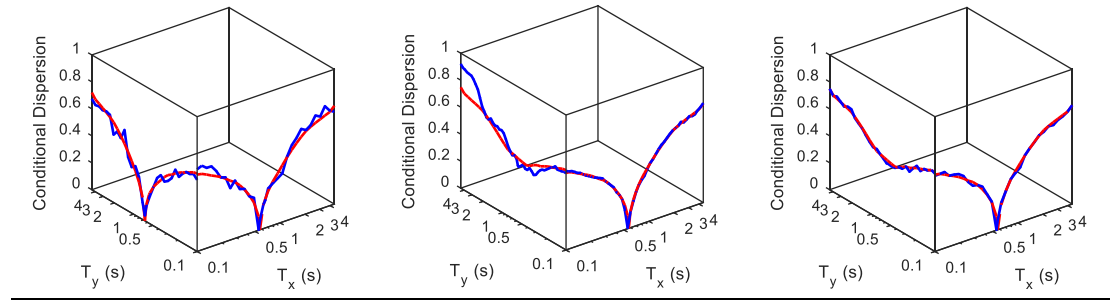


**Figure 4: Illustration of the CS record sets used for the analysis of the 3-story building excerpted from Kohrangi et al. (2019). Top: target CS and ground motion response spectra; Middle: target and candidate match of mean CS; Bottom: target and candidate match of standard deviation**

In the methods described so far, the vertical component of the ground motion is neglected although it may be relevant for the response of some structures (e.g., dams, reinforced concrete precast structures, specific components in nuclear power plants). Recently, Bazzurro et al. (2020) extended the methodology of Kohrangi et al. (2019) to select records compatible with both horizontal and vertical components of the hazard.

They first considered the standard CS method where scalar  $IM$  is used. To derive the lognormal model that includes vertical component, it was necessary to develop correlation coefficients of horizontal and vertical spectral ordinates (Kohrangi et al., 2020). They then considered CS for a vector  $\mathbf{IM} = \{IM_h, IM_v\}$ , where  $IM_h$  is the geometric mean of the two horizontal components and  $IM_v$  is the vertical component. These two methods were compared using a liquid storage tank located in Elesfina, Greece. They showed that ignoring the impact of the vertical component of the ground motion results in an underestimation of the maximum uplift demand. These findings, however, may be structure-specific and their generality is currently under investigation.

## 2. Recorded and synthetic ground motions for engineering analyses

The previous section discussed different rock-hazard-consistent ground motion selection methodologies such as *CS*, *CMS*, *CS – MR*, and *GCIM*. In all of these cases, it is essential to ensure that the response spectra of the selected record sets match the *CS* targets so that no significant bias is introduced into the ensuing structural response. To achieve this objective, it is paramount to have sufficient records to ensure that these *CS* targets are matched at all intensity levels. However, the number of available ground motions recorded on rock is not plentiful. The problem caused by the scarcity of rock ground motions (especially severe ones) in record selection can be circumvented by either i) using real recordings on both rock and soil conditions (the latter group utilized either as-is or sometimes deconvolved to rock conditions) appropriately scaled to the amplitude levels desired by the application at hand, or ii) by using synthetic rock ground motions, or iii) by adopting a combination of the previous two. These practical alternative approaches need to be scrutinized before their adoption in rock-hazard consistent ground motion selection applications, such as this one, is recommended.

Hence, in the context of record selection for assessing a structure's risk, we investigate three critical aspects:

1. Is the use of soil ground motions blended with rock ones legitimate?
2. Given the scarcity of severe ground motions, is amplitude scaling of weaker signals to match the target *CS* a legitimate operation or does it create ensembles of ground motions that cause bias in the structural response?
3. Can we blend synthetic and real ground motions?

To address these three questions, we consider as a case study a common suite of SDOFs systems that, for illustration purposes, we locate in Central Italy. We devise a battery of seismological and engineering tests to investigate whether the response of these suites of SDOF systems to the selected sets of hazard-consistent records are statistically and seismologically distinguishable from those caused by the ground motions recorded on rock, which are real and, to the extent possible, unscaled.

The following sections describe the assembled database of real and synthetic ground motions from which hazard-consistent ground motions are extracted for response estimation. Regarding the synthetic ground motions we first describe the procedure utilized for producing them and show the seismological tests run to check their adequacy in terms of simulated vs. real *IM* - distribution matching. Then we present the comparison of the responses of SDOFs to hazard-consistent ground motions for each one of the three cases mentioned above.

### 2.1. Database of real motions

To assemble the database of real ground motions to be used for the studies defined in the previous chapter and, later, for fragility analysis in WP6, we used the flatfiles from different data repositories. More specifically, we used the Engineering Strong-Motion (ESM) database (<https://esm-db.eu>) (Lanzano et al., 2019), NGA-West2 ([NGA West 2 | Pacific Earthquake Engineering Research Center \(berkeley.edu\)](https://ngawest2.berkeley.edu/)) (Ancheta et al., 2014), New Zealand Strong-Motion database ([Home - GNS Science](https://www.gns.govt.nz/research/strong-motion/)) (here referred to as GNS) (Van Houtte et al., 2017), and finally, we complemented the data with the updated version of worldwide NEar-Source Strong-motion (NESS) ([INGV/RELUIS NESS flat-file](https://www.ingv.it/reluis/ness/)) (Sgobba et al., 2021). The ground motions from the NGA-West2 and NESS databases are retained if recorded at stations outside the geographical area covered by the other two databases to avoid double-counting. As the available information in the different flatfiles varies, we merged them into one Matlab (mat) file and one Python (pickle) file with common fields. As spectral acceleration ordinates in these databases were reported at different vibration periods, we interpolated them to obtain the same array of periods that corresponds to the one available in the ESM database. A representation of the structure of the final mat file (Figure 5) can be separated into six different blocks: intensity measures, event metadata, station metadata, source metadata, source-to-site distance metrics, and waveform metadata. One should keep in mind that, if necessary, depending on the application, more information about these ground motions could

## D5.1 Methodology for selecting ensembles of rock-hazard consistent ground motions for fragility curve computations and datasets for WP6

be added to the mat file. In Figure 6, one can see the map of the epicenters of the earthquakes with a magnitude  $M_w > 5$ .

In total, a suite of 34107 3-component ground motions were assembled. In Figure 7, we show the distribution of magnitude (moment magnitude, if available, and local magnitude otherwise),  $V_{s30}$  (measured if available, calculated otherwise), and Joyner and Boore distance ( $R_{jb}$ ).

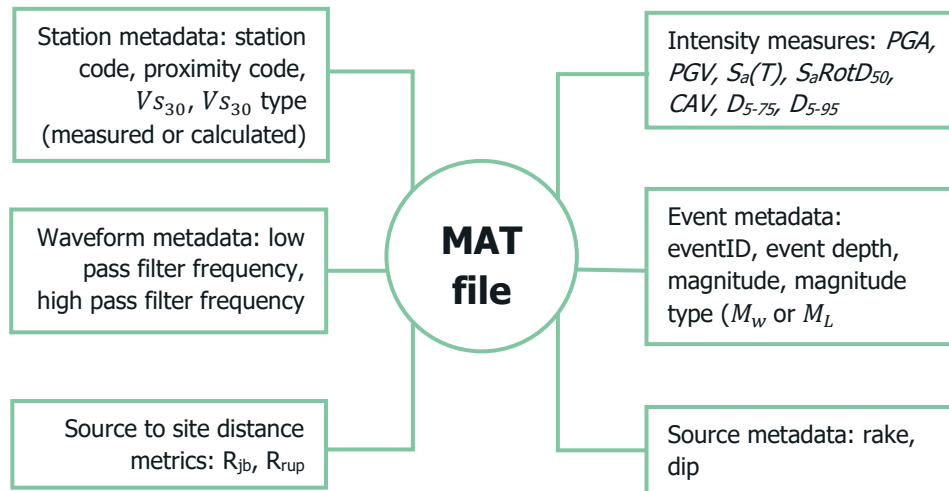


**Figure 5: Schematic structure of the MAT file that contains all considered ground motions.**

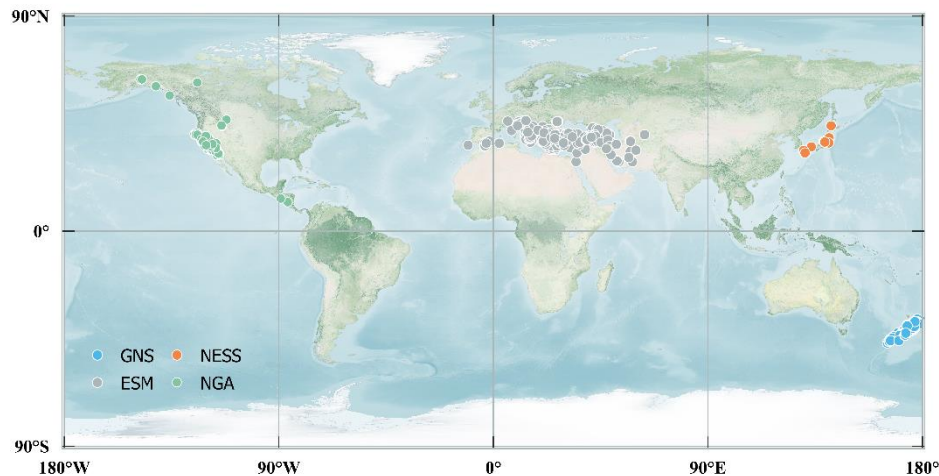


**Figure 6: Map of epicenters of the earthquakes included in the assembled dataset, color-coded based on the original databases.**

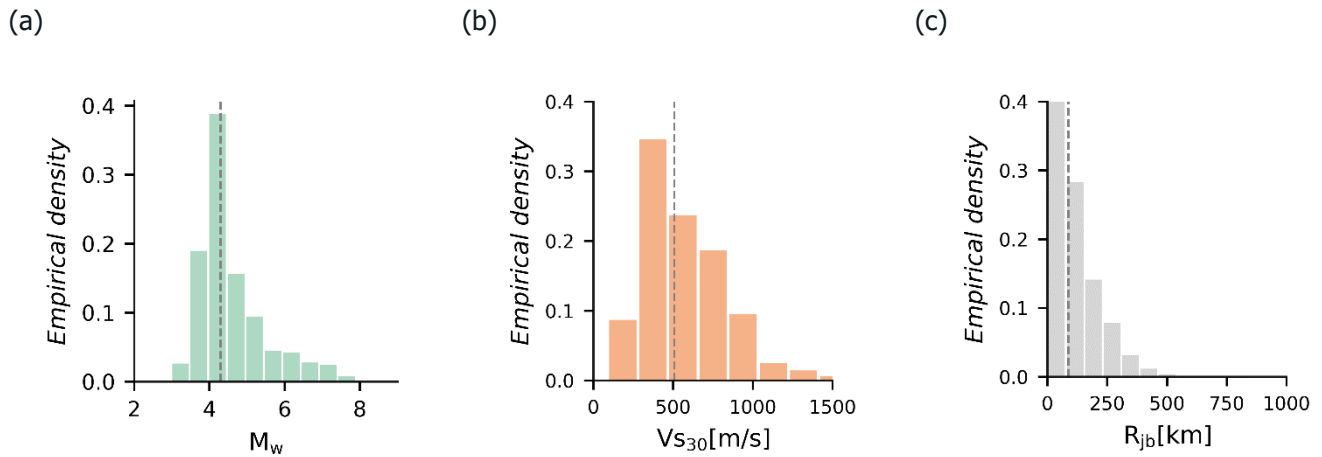


**Figure 7: – Distribution of (a) magnitude, (b)  $V_{s30}$  and (c) Joyner and Boore distance. Vertical dashed line refers to the median values.**

## 2.2. Database of synthetic motions

One of the key objectives in the use of simulated ground motions is to provide accelerograms for earthquake scenarios that are either missing or insufficiently populated in the databases of recorded ground motions. Before using them for structural response assessment, however, these simulated ground motions must be proven to be realistic when compared to those recorded from earthquakes having the same event/site causative parameters, namely:

- Moment magnitude ( $M_w$ )
- Source-to-site distance, in this case considered as the hypocentral distance ( $R_{hypocentral}$ )
- Hypocentral depth ( $Z$ )
- Site characteristics, in this case considered with the average shear wave propagation velocity of the upper 30m ( $V_{s30}$ )

In this section we summarize the generation of a database of simulated ground motions, called the SDB, which, by design, is made consistent with (a subset of) the Engineering Strong-Motion (ESM) database (Lanzano et al., 2019). This subset includes ground motions caused by events with magnitudes from 4 to 8 ( $4 \leq M_w < 8$ ), hypocentral distances below 100 km ( $R \leq 100 \text{ km}$ ) and recorded at sites with  $V_{s30} \geq 400 \text{ m/s}$ . The definition of these constraints corresponds to the limits of performance of the simulation method, as explored in the upcoming publication (Alvarez et al., 2022b). A graphical representation of the distribution of these features is shown in the upcoming Figure 10.

As shown in the following sections, we first provide general information about the simulation technique used to generate the synthetic scenarios. Next, we proceed to calibrate the technique to reproduce different  $IMs$  of interest from the reference ESM subset scenarios. Finally, we generate the SDB to be consistent with the ESM subset in terms of ground motion features of interest.

### 2.2.1. Stochastic ground motion simulation methodology (SGMSM)

The ground motions in the SDB were simulated with the Stochastic Ground Motion Simulation Method (SGMSM) proposed by Otarola & Ruiz (2016) and later modified by Alvarez et al. (2022a). This SGMSM distinguishes itself from other stochastic methods, such as those proposed in (Conte & Peng, 1997; David M. Boore, 1983; Motazedian & Atkinson, 2005; Papageorgiou & Aki, 1983; Pousse et al., 2006; Sabetta et al., 2021; Sabetta & Pugliese, 1996) by modelling the full body-wave field spectra of the earthquake ground motions, i.e., P, SV, and SH-waves, thus resulting in coherent three-component time histories. The latest modifications of the SGMSM by Alvarez et al. (2022a) include the coupling of the original stochastic simulation technique with a kinematic representation of the source rupture and the addition of the Fourier Amplitude Spectrum (FAS) correlation structure to all three orthogonal components.

A full description of the SGMSM may be found in Alvarez et al. (2022a). That study also features a complete description of the input required to simulate ground motions, and the sensitivity of the method to each of them. Finally, an evaluation of the implementation of the SGMSM, for its use as a substitute for GMPEs for specific scenarios is currently in progress by Alvarez et al. (2022b). These studies present comparisons of the simulated ground motions with reference recorded ground motions and statistical models calibrated from databases of recorded ground motions.

### 2.2.2. Calibration of the SGMSM

The complete description of the SGMSM requires the definition of a source (given by the geometry of the fault, slip distribution and location of the hypocenter), a 1D regional velocity model describing the characteristics of the crust, and finally the values of parameters used in the construction of the ground motion spectrum. See Alvarez et al. (2022a) for a full description of the input and sensitivity of the SGMSM to each of these inputs.

For this implementation of the SGMSM, and due to the lack of site-specific information, we resorted to generic descriptions of the source and regional velocity models. For the source, we defined the dimensions of the fault based on the regression model proposed by Wells & Coppersmith (1994).

## D5.1 Methodology for selecting ensembles of rock-hazard consistent ground motions for fragility curve computations and datasets for WP6

Moreover, the distribution of the slip in the source was specified based on a uniform spatial density function, thus allocating the scenario-consistent slip with equal probability in each of the considered sub-sources (all sources are discretized into 100 sub-sources). The regional velocity model was taken as the generic rock velocity model defined in Boore & Joyner (1997). Finally, the input variables defining the ground motion spectrum were taken from the characterization of the Fourier Amplitude Spectrum (FAS) of the scenarios contained in the ESM database conducted by Bindi & Kotha (2020). In their study, the authors used the Generalized Inversion technique to parameterize the FAS of earthquake ground motions contained in the complete ESM database. Their description of the ground motions, however, focused on the FAS and did not account for the duration or the shape of the acceleration time histories (modelled through the modulating window-functions, see Boore (2003)). Furthermore, the FAS model considered in the inversion procedure differs from our SGMSM because it only considers SH-waves and point source models. These discrepancies resulted in initial simulated ground motions with unrealistic durations and overly large high-frequency content (due to the differences in the description of the source in the model considered in the inversion). Considering these initial results, we adapted the values of the parameters provided in Bindi et al. (2020) to our SGMSM and defined the modulating functions with an iterative approach. The calibration of the adequacy of the simulated ground motions was conducted by comparing the error between the median values of the  $IMs$  from the reference subset and those from the simulated one. The following list summarizes the  $IMs$  considered in the computation of the error:

- The ordinates of the response spectra of the geometrical mean of the horizontal components (at  $PGA$ , 0.1, 0.3, 0.5s and 1.0s),  $Sa_{GM}(t)$
- The Peak Ground Acceleration of the vertical component,  $PGA_{UD}$
- The Husid duration of the geometrical mean of the horizontal components,  $Husid_{GM}$
- The Arias intensity itself of the geometrical mean of the horizontal components,  $AI_{GM}$ .

The combination of the errors for each of the previously mentioned  $IMs$  was done considering a weighting scheme. Equation (7) shows this computation:

$$Error = 0,2\varepsilon_{Husid,GM}^2 + 0,2\varepsilon_{AI,GM}^2 + 0,1\varepsilon_{PGA,UD}^2 + 0,1\varepsilon_{PGA,GM}^2 + 0,1\varepsilon_{Sa(0.1s),GM}^2 + 0,1\varepsilon_{Sa(0.3s),GM}^2 + 0,1\varepsilon_{Sa(0.5s),GM}^2 + 0,1\varepsilon_{Sa(1.0s),GM}^2 \quad (7)$$

Acknowledging the fundamental differences introduced in ground motion by magnitude, distance, and site-specific conditions, we calibrated the SGMSM for different reference groups of scenarios within the ESM subset. Specifically, we considered a total of 12 groups for the calibration. These are defined by the following criteria:

- Magnitude:  $4 < M_w \leq 5$ ,  $5 < M_w \leq 6$  and  $M_w \geq 6$
- Hypocentral distance:  $R_{hypocentral} \leq 50 \text{ km}$  and  $50 \text{ km} < R_{hypocentral} \leq 100 \text{ km}$
- Site:  $400 \text{ m/s} \leq V_{s30} < 600 \text{ m/s}$  and  $V_{s30} \geq 600 \text{ m/s}$

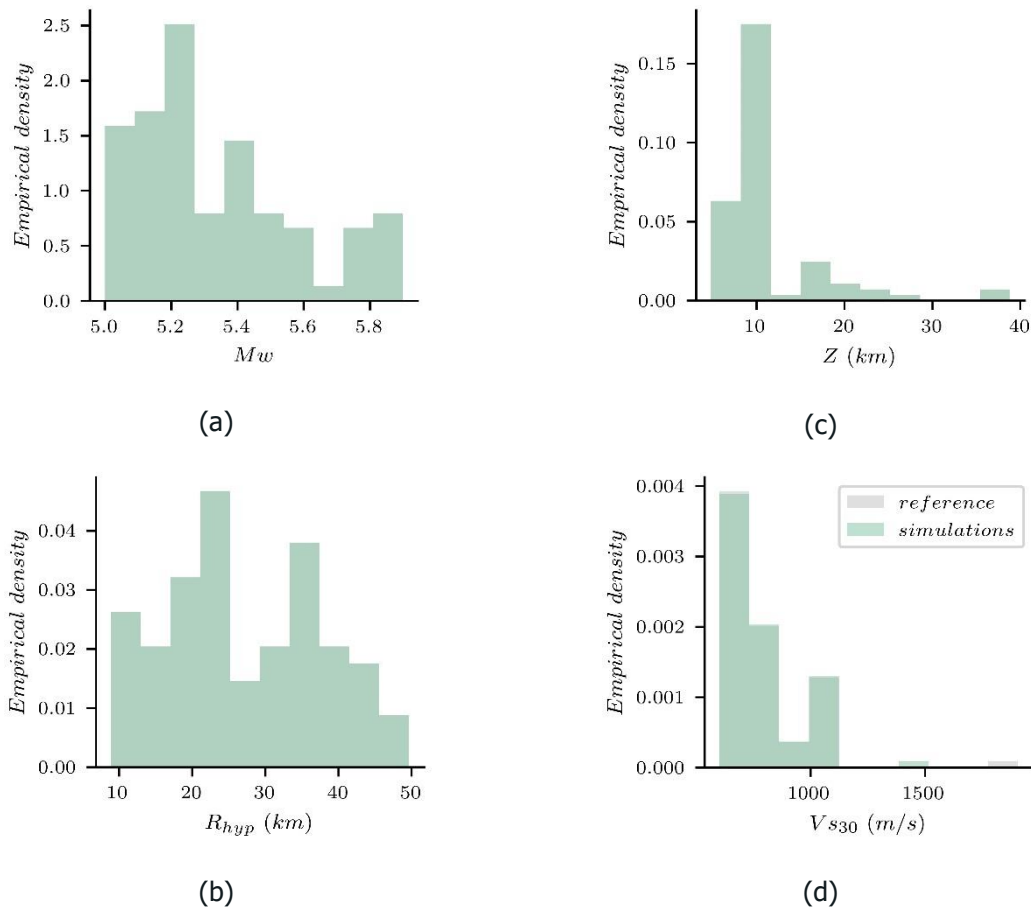
To directly compare the reference (ESM subset group) and simulated scenarios, the calibration of the SGMSM was done by reproducing the magnitude, hypocentral distance and hypocentral depth of the scenarios in each reference group. Site effects were considered by sampling site-specific elastic transfer functions, given the reference  $V_{s30}$ , from a database generated with the transfer function computed with the soil profiles of sites registered in the Japanese network (National Research Institute for Earth Science and Disaster Resilience, 2019). Other input, such as dip, strike, and rake of the source (not included in the description of the references) were sampled as random variables with uniform distributions. The ranges of variation of these variables were considered as  $10^\circ$ - $90^\circ$  for the dip,  $0^\circ$ - $360^\circ$  for the strike and  $0^\circ$ - $90^\circ$  for the rake. At the end of the calibration procedure, we obtained a set of parameters and a description of the modulating function for each of the defined groups.

Figure 8 shows a comparison of the ground motion features of the reference and simulated scenarios for the calibration group characterized by  $5 < M_w \leq 6$ ,  $R_{hypocentral} \leq 50 \text{ km}$  and  $V_{s30} \geq 600 \text{ m/s}$ . From the figure we observe the match of the replicated ground motion features (i.e.,  $M_w$ ,  $R_{hypocentral}$  and



Z). Small discrepancies are observed in the comparison of the distribution of site characteristics ( $V_{S30}$ ), due to the limitation of the database of considered transfer functions.

Figure 9 shows the comparison of the IMs for the events inside the bin defined for scenarios with  $5 < M_w \leq 6$ ,  $R_{hypocentral} \leq 50 \text{ km}$  and  $V_{S30} \geq 600 \text{ m/s}$ . This figure shows a close fit of the spectral shapes (given high importance in the weighting scheme), more important differences are noticed in the distribution of Husid duration and Arias intensity. The importance of each IM considered in the calibration procedure may be adjusted by considering different weighting schemes. For this application, however, we prioritize the spectral shape considering that the initial implementations of our simulated ground motions are based on record selection schemes considering only this IM. Figure 9e shows the comparison of the waveforms for one of the simulated scenarios (randomly selected). This type of comparison allows for the evaluation of features such as the distribution of the amplitude of the motion over the duration of the record.



**Figure 8: Comparison of reference and simulated ground motion features for scenarios inside the calibration for group with  $5 < M_w \leq 6$ ,  $R_{hypocentral} \leq 50 \text{ km}$  and  $V_{S30} \geq 600 \text{ m/s}$ . (a) Moment magnitude ( $M_w$ ), (b) – Hypocentral distance ( $R_{hypocentral}$ ), (c) – Hypocentral depth ( $Z$ ), and (d) -  $V_{S30}$ . The figures display the perfect match, by design, of  $M_w$ ,  $R_{hypocentral}$ , and  $Z$ . Discrepancies are noticed in  $V_{S30}$  for large velocities.**

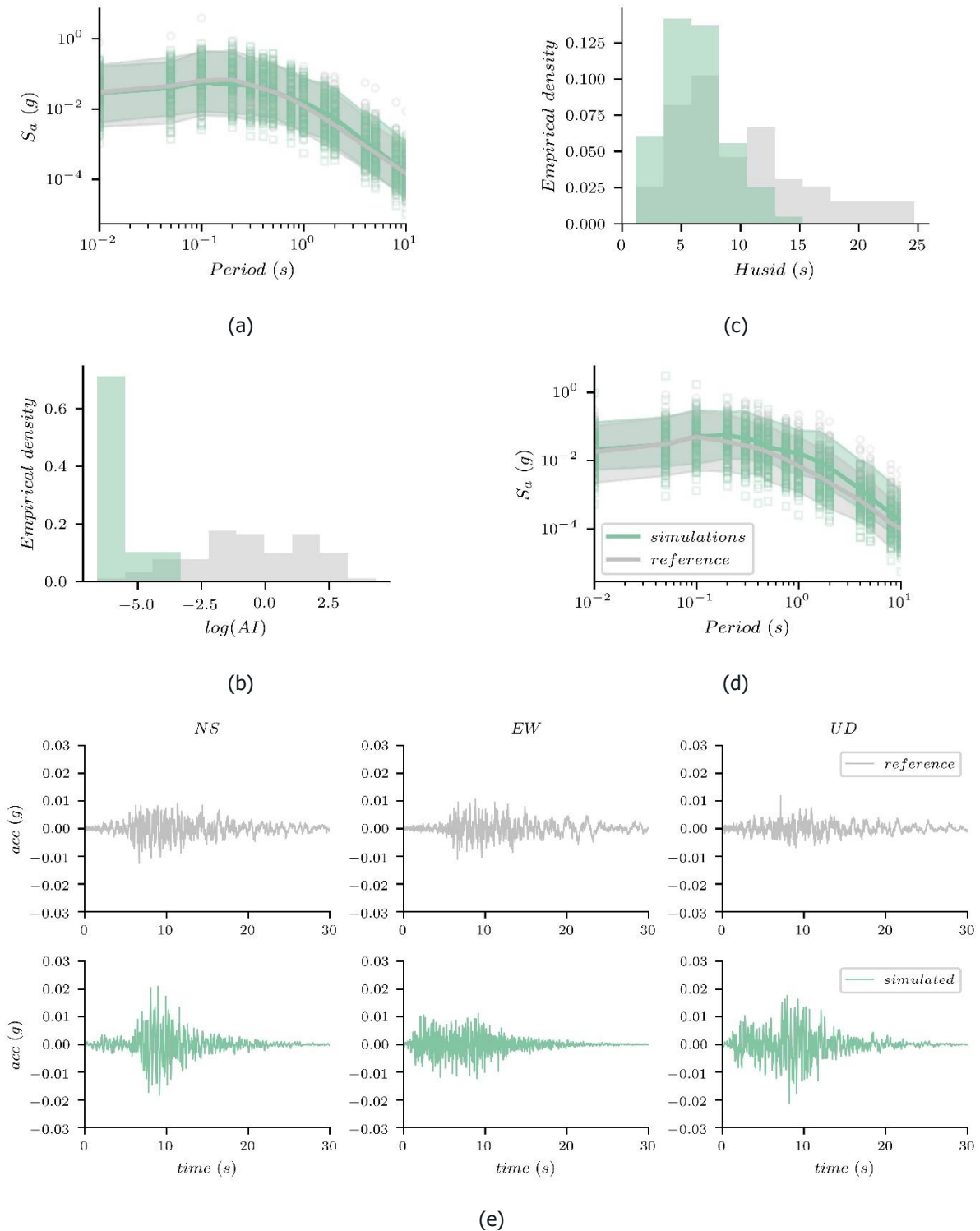


**Figure 9: Comparison of reference and simulated distributions of the IMs of interest considered during the calibration process of scenarios for group with  $5 < M_w \leq 6$ ,  $R_{hypocentral} \leq 50$  km and  $V_{s30} \geq 600$  m/s. (a) – Geometric mean of the horizontal response spectra, (b) – Geometrical mean of the horizontal Husid durations, (c) – Geometrical mean of the horizontal AI, (d) – Response spectra of the vertical component, and (e) Comparison of time histories for one of the scenarios replicated scenarios ( $M_w = 5.90$ ,  $R_{hypocentral} = 41.78$  km,  $Z = 7.50$  km,  $V_{s30} = 1100$  m/s)**



### 2.2.3. Generation of a simulated database

After the calibration of the SGMSM, for each of the different groups defined within the ESM subset, we generated our simulated database, SDB. The SDB was populated by Monte Carlo sampling of the joint probability density function of the ground motion features of interest from the entire ESM subset ( $M_w$ ,  $R_{hypocentral}$  and  $Z$ ). Same as for the calibration procedure, site effects were included by sampling of the previously mentioned database of transfer functions. This procedure allows use to generate a new database whilst preserving, to the extent possible, the fractions in each bin of the joint probability mass function of the ground motion features of interest. Figure 10a and Figure 10b show the magnitude-distance distribution ( $M_w$ ,  $R_{hypocentral}$ ) of the ESM subset and the SDB, respectively. Figure 10c shows the comparison of the median response spectra for the geometrical mean of the horizontal components, and Figure 10d shows a comparison of the distribution of sites ( $V_{s30}$ ) for both databases.

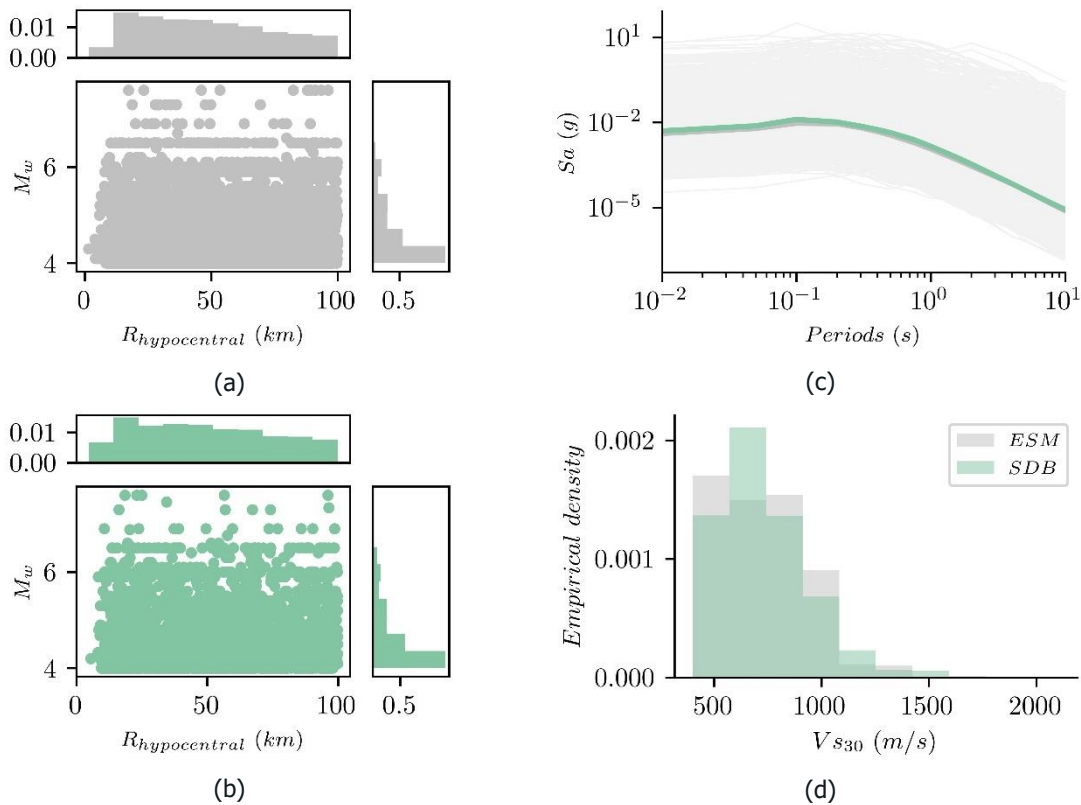


**Figure 10: Comparison of the Magnitude and site hypocentral distance for (a) – ESM and (b) – SDB. (c) – Comparison of the ESM and SDB response spectra of the GM component for all scenarios (median spectra are shown in green and grey, while individual spectra in light grey), and (d) – Distribution of the  $V_{s30}$  characterizing the scenarios in each database .**

## 2.3. Identification of rock ground motions

### 2.3.1. Reference Site Classification Methods

Given the purposes of this study and the increasing number of recordings at permanent and temporary seismic networks and stations, accurate criteria to identify what constitutes a reference site (i.e., a site not affected by local amplification effects), which for simplicity was called “rock” earlier, are essential. To distinguish rock ground motions from the rest of the waveforms present in the databases of real ground motions considered here (ESM, NESS, GNS, and NGA) we use three approaches:

- ***V<sub>s30</sub> method*** -where sites are classified according to the reported  $V_{s30}$  value – sites with  $V_{s30}$  values lower than 400 m/s are classified as soil and values above 800 m/s as rock. No other proxies for classifying the reference site are used. This method is self-explanatory and will not be discussed any further below.
- ***Complex method***, which classifies sites following proxy-based procedures where all records not classified as rock or reference sites according to their database-related proxy method are assumed to be soil (see Subsection 2.3.2). This method combines the works from different sources (Kaiser et al., 2017; Lanzano et al., 2020), which adopt criteria beyond the use of only a  $V_{s30}$  value, according to the available station metadata for each database.
- ***Pilz’s method***, a data-driven method that identifies reference rock sites in two ways: a) applying five criteria designed to capture soil amplification and b) machine learning (see Subsection 2.3.3).

### 2.3.2. Complex Method

This method classifies the stations at which the ground motions in the ESM database were recorded as rock or soil sites following the Lanzano et al. (2020) approach. This approach seeks to improve reference site identification by going beyond the use of  $V_{s30}$  as a sole method for classification and instead employs seven different proxies, inferred from seismological analysis, geophysical and geological data. The method analyses each station, taking into account its location, housing and surface conditions, alongside its recordings to verify that no significant amplification exists. All the proxies are then scored according to their compliance with the rock conditions (shown in Table 1) and a set of hierarchal values that weight each parameter, defining a final classification for the stations.

We adopt another proxy-based method to classify the station sites for the GNS database (Kaiser et al., 2017), which considers four key parameters to define a rock site: the site soil classification, the fundamental period at the site (derived from the recordings), the depth of a hard rock shear wave velocity and the  $V_{s30}$  for the cases in which the quality of the depth of hard rock measurements is low or missing. The conditions for these methods are summarized in Table 1. Additionally, given the lack of additional metadata for the NESS database, the rock stations are classified only by the NEHRP classes of rock and hard rock. It must be noted that, while this method is based only on  $V_{s30}$ , it uses different values to the  $V_{s30}$  method to classify the rock stations and is adopted to keep the same total number of records through both methods. While this may be a simplified assumption, low number of ground motions that are within this category ensures that they will not introduce any bias to the results. Finally, the classification for the NGA database was done using an adjusted Lanzano et al. (2020) approach (since some proxies were missing). Several proxy-based methods are used because not all databases provide the same station data, and it is not possible to use a single method for all of them.

Lanzano 2020		Kaiser 2017	
Proxy	Condition for rock	Proxy	Condition for rock
Housing	Limited interaction with other structures (free field)	Site Classification	Rock or hard rock according to NZS1170.5 Site Class
Topographic condition	Slope < 15°	Fundamental period at site	To be either <0.2s or a flat HVSR
Surface geology	EC-8A or B	Depth to a shear wave velocity of 1000 m/s	0 m
$V_{S30}$	$V_{S30} > 750$ m/s	$V_{S30}$	$V_{S30} > 760$ m/s
HVRS of acceleration spectra	Flat		
Site-to-Site term of the horizontal components	Must be negative or close to 0 across all periods		
Database	ESM, NGA (considered without surface geology)	Database	GNS
This method uses a set of weights to classify the station as rock whenever a value is obtained		This method will consider a rock site once all conditions are met	

**Table 1: Conditions for rock on the complex method**

### 2.3.3. Pilz's Method

The reference site should exhibit neither resonances due to shallow low-stiffness layers nor amplification from local topographic or basin-induced effects. Additionally, a reference site should not introduce significant modulation of the high-frequency spectral content of ground motion due to site-specific attenuation. From the stations identified as rock sites of the Italian accelerometric data set, Bindi et al. (2011) identified 23 out of 47 sites as reference sites, concluding that about half of the rock sites in Italy (a typical host region for European ground motion) show non-negligible amplifications at variable frequencies, possibly due to the presence of weathered rock or thin soft layers above more consistent rock and potential interaction with surface topography effects. Laurendeau et al. (2018) reported similar conclusions for KiK-net stations corresponding to stiff soil or rock sites. Pilz et al. (2019) extended these approaches by developing a set of homogeneous criteria for identifying reference site conditions.

The approach is based on large pan-European data sets, i.e., we only rely on harmoniously mapped and fully data-driven approaches. We propose the use of five criteria for the identification of outcrop reference sites covering the full frequency spectrum of engineering interest. While a sufficient number of earthquake recordings are required at each site, the application of the proposed measures does not require the availability of site-specific information like velocity profiles or site-specific metadata, which are not available everywhere. As described in Pilz et al. (2019) the criteria comprise:

- Surface geology taken from the harmonized pan-European surface geological map (European Geological Data Infrastructure, EGD1 2017, scale 1:10<sup>6</sup>) for 21 European countries.

## D5.1 Methodology for selecting ensembles of rock-hazard consistent ground motions for fragility curve computations and datasets for WP6

- ▶ Slope of topography, discarding all stations with an average slope of more than 15° (Paolucci, 2002) which is also in agreement with several building codes like EC8 (CEN, 2004) and the recent Italian Technical Norms (NTC, 2008).
- ▶ Flat horizontal-to-vertical spectral ratios at low and intermediate frequencies between 0.2 and 30 Hz with an amplitude less than 3 for avoiding any influence of impedance contrasts at depth as well as surficial amplification due to weathering calculated from the S-wave window (following the criteria proposed by Bard et al. (2004) and verified by a larger number of subsequent studies).
- ▶ Similarity of the site-specific high-frequency decay of the S-wave window ( $\kappa_0^{AH}$ ) and coda waves ( $\kappa_0^{coda}$ ) for minimizing the influence of near-surface scattering effects affecting the high-frequency range (Pilz et al., 2019).
- ▶ Negative local magnitude station correction following Bindi et al. (2019). Besides a characterization of the regional attenuation characteristics, such station corrections allow identifying sites more affected by local ground-motion modification effects than all other studied sites.

The criteria have been applied to 2330 sites and corresponding data for events between January 2000 and December 2018 that have been downloaded from the EIDA (European Integrated Data Archive) data centres. In the end, 348 086 three-component waveforms, originating from 24 234 earthquakes, were analysed. Table 2 is providing an overview for the quality criteria applied for each site attribute investigated.

Site attribute	Records	Events	Magnitude	Number of sites fulfilling quality criteria
Geology				2,330
H/V	348,086	24,234	$\geq 3.0$	1,920
$\kappa_0$	87,384	10,732	$\geq 3.5$	1,384
MI correction	205,300	12,721	$\geq 2.5$	2,271

**Table 2: Number of records and analysed sites for each data set considered.**

Geological information is available for all the 2330 sites: 1366 sites are located on rock while 964 are located on soft material, mainly in Central and Eastern Europe. Among the 1366 rock sites, 54 are characterized by slope values larger than 15° and are therefore excluded. For the H/V spectral ratios there is a remarkably large number of rock sites with significant amplification at frequencies around and higher than 1 Hz, confirming the results of previous studies, which have proven that a large number of rock sites will have a non-negligible site response in the high-frequency range. Of the rock sites, only 736 sites show an H/V spectral ratio less than 3 over the entire frequency range. For  $\kappa_0$  only for 614 of 1366 sites with a sufficient number of recordings, an adequate similarity between  $\kappa_0^{AH}$  and  $\kappa_0^{coda}$  is found. t-statistics (not shown here) indicate the selection of sites and, therefore, the similarities in  $\kappa_0$ , are statistically significant. For 2237 stations at 914 sites a negative station correction has been obtained, meaning that for these sites the local amplification is lower than the average of all site amplifications.

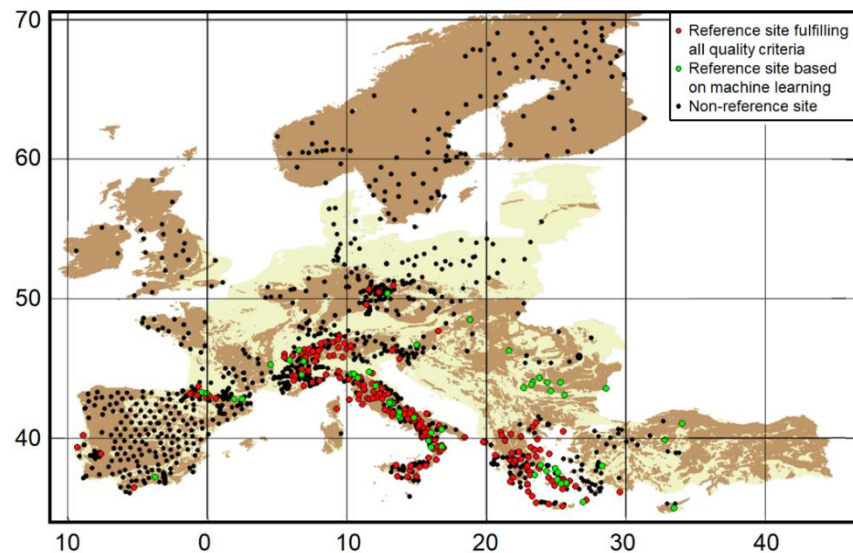


**Figure 11: Distribution of considered stations. Stations fulfilling all reference-site criteria outlined in the text are shown as red dots. Green dots represent additional reference site identified through machine learning. Black dots represent all analysed stations while yellow dots indicate stations for which fewer than 10 events with sufficient SNR have been recorded. Brown colour represents rock conditions from a surface geologic map while soft soils are shown in ochre.**

In the end, only 200 sites simultaneously fulfil all five criteria on amplification, high-frequency attenuation and magnitude station correction. These 200 sites are shown as red dots in Figure 11. The relatively low number is partially due to the fact that not all classification attributes are simultaneously available for all sites. However, we also emphasize that the attributes concern different frequency bands of the spectrum.

We also apply a multiple-training machine learning algorithm to all remaining sites that were not classified before as rock but that fulfil all quality criteria for which a sufficient number of records is available. These site classification rules add another 51 reference stations (indicated in green in Figure 1). The figure also indicates that a large number of sites, especially in Northern Europe, did not qualify as reference sites due to an insufficient number of recordings with a sufficiently high signal to noise ratio (SNR). Although  $V_{S_{30}}$  alone cannot capture the whole features of a specific site response, our selection of reference sites coincides with sites having high  $V_{S_{30}}$  values. Although  $V_{S_{30}}$  alone cannot capture the whole features of a specific site response, our selection of reference sites coincides with sites having high  $V_{S_{30}}$  values.  $V_{S_{30}}$  values (both measured and interpolated) are available for 350 sites. Of these 350 sites, only 57 did qualify as reference sites. For all of these 57 sites,  $V_{S_{30}}$  values are larger than 360 m/s and for 42 of these 57 sites,  $V_{S_{30}}$  is larger than 760 m/s.

#### 2.3.4. Rock ground motions

After an evaluation of the three methods, we realized that Pilz's method does not lend itself well for record selection since its strict restrictions on the number of sites classified as rock stations leave too few rock records eligible for further processing. Additionally, this criterion is not readily applicable to all the four ESM, NESS, GNS, and NGA databases utilized here. Therefore, we utilized only the  $V_{S_{30}}$  and the Complex Method for partitioning rock and soil records in the entire database comprising all four ground motion repositories. This exercise resulted in the identification of four groups of ground motions: the *rock*  $V_{S_{30}}$ , the *soil*  $V_{S_{30}}$ , the *rock complex* and the *soil complex* groups.

More precisely, out of more than 34000 available records, this operation identified 8037 3-component rock ground motions according to the  $V_{S_{30}}$  method, while 10113 comply with the complex classification method. However, most of the complex rock records were caused by earthquakes in a magnitude range lower than that of the causative scenarios of the  $V_{S_{30}}$  rock records. Hence, the mean response spectrum

## D5.1 Methodology for selecting ensembles of rock-hazard consistent ground motions for fragility curve computations and datasets for WP6

of the former is lower than both the mean response spectrum of the  $V_{S30}$  rock records and of that of the full database (see Figure 12).

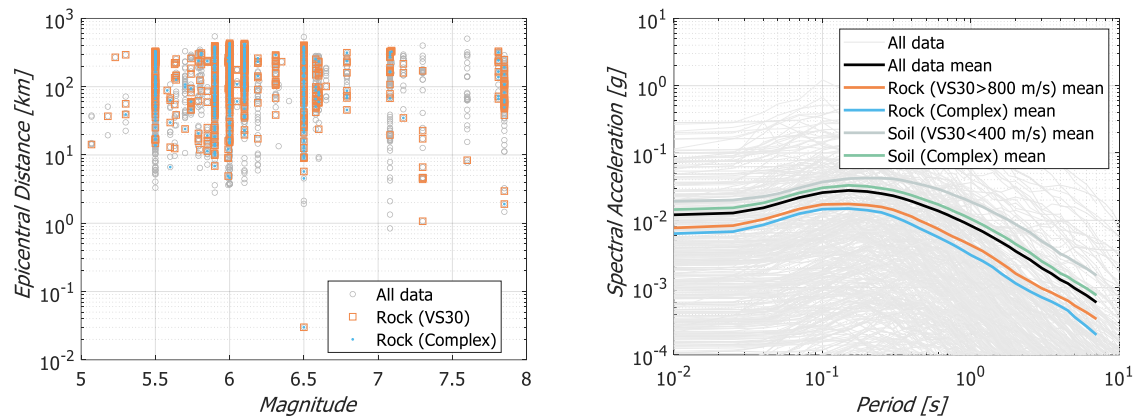


**Figure 12: Magnitude distance distribution (left) and full response spectra (right)**



### 3. Selection procedure of hazard-consistent ground motions

The procedure adopted for assessment of the adequacy of using different sets of records (soil, scaled rock, and synthetic) in lieu of unscaled rock ground motions (benchmark) for structural response assessment is the *CS* method. The statistics of the responses caused by the *CS*-consistent benchmark set will be compared and contrasted with the statistics of the responses caused by the other 3 sets of ground motions selected to be consistent with the same *CS*. To test the adequacy for both nearly linear and severely nonlinear responses, we selected hazard consistent records for ten intensity levels (*IMLs*) of increasing severity. For this evaluation, we chose a site in Perugia, Italy, located in 43.11°N and 12.39°E on rock with  $V_{s30}=800$  m/s. The 10 *IMLs* correspond to values ranging between 0.2% poe in 50 years (i.e., return period of 25000 years) to 70% poe in 50 years (i.e., return period of 40 years). The first necessary step is to perform PSHA for the selected site to identify the *IMLs* corresponding to the desired poe's. For the calculations, we used the Boore and Atkinson (2008) GMPE, the area source model developed for the SHARE project<sup>1</sup>, and the OpenQuake software (Pagani et al., 2014).

Table 3 summarizes the different IM values corresponding to the 10 poe's for the four selected *IMs*: spectral acceleration at 0.2s, 1.0s and 2.0s (namely  $S_a(0.2s)$ ,  $S_a(1s)$  and  $S_a(2s)$ ) and average spectral acceleration in the 0.2s to 2.0s range computed for steps of 0.1s, namely  $AvgS_a(0.2:0.1:2.0s)$ , while Figure 13 shows the corresponding rock hazard curves. The next step for the computation of the *CS* consists of carrying out hazard disaggregation analysis to identify the events (in terms of their magnitude, distance, and epsilon values) most contributing to the hazard at each intensity level (Figure 14).

IML	poe in 50 years [%]	Return period	$AvgS_a$	$S_a(0.2s)$	$S_a(1s)$	$S_a(2s)$
1	70	42	0.040	0.2	0.042	0.017
2	50	72	0.053	0.26	0.057	0.023
3	30	140	0.075	0.35	0.08	0.034
4	<u>10</u>	<u>475</u>	<u>0.136</u>	<u>0.58</u>	<u>0.146</u>	<u>0.064</u>
5	5	975	0.190	0.78	0.203	0.091
6	2	2475	0.285	1.12	0.305	0.139
7	1.5	3310	0.320	1.25	0.343	0.158
8	1	4975	0.375	1.44	0.402	0.187
9	0.6	8310	0.450	1.71	0.485	0.229
10	0.2	24975	0.635	2.12	0.697	0.337

**Table 3: Values of the four *IMs*,  $S_a(0.2s)$ ,  $S_a(1s)$ ,  $S_a(2s)$  and ,  $AvgS_a(0.2:0.1:2s)$  at the 10 poe levels at the Perugia site. *IML* 4 corresponds to the 10% in 50 years level (i.e., 475 yr return period, which is used for design.**

<sup>1</sup> www.share-eu.org

## D5.1 Methodology for selecting ensembles of rock-hazard consistent ground motions for fragility curve computations and datasets for WP6

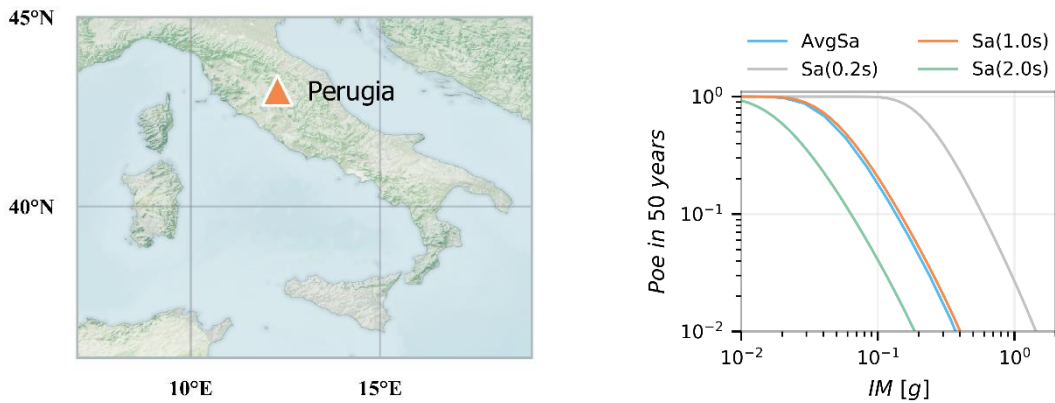


**Figure 13: (a) location of the site used as case study and (b) rock hazard curves for different IMs**

Having defined the main events, we compute a target conditional spectrum for each intensity level. The target spectra is computed using the mean of the causative parameters at all hazard levels. The correlation coefficient between spectral ordinates at any pair of periods is estimated following the correlation model of (Baker & Jayaram, 2008)

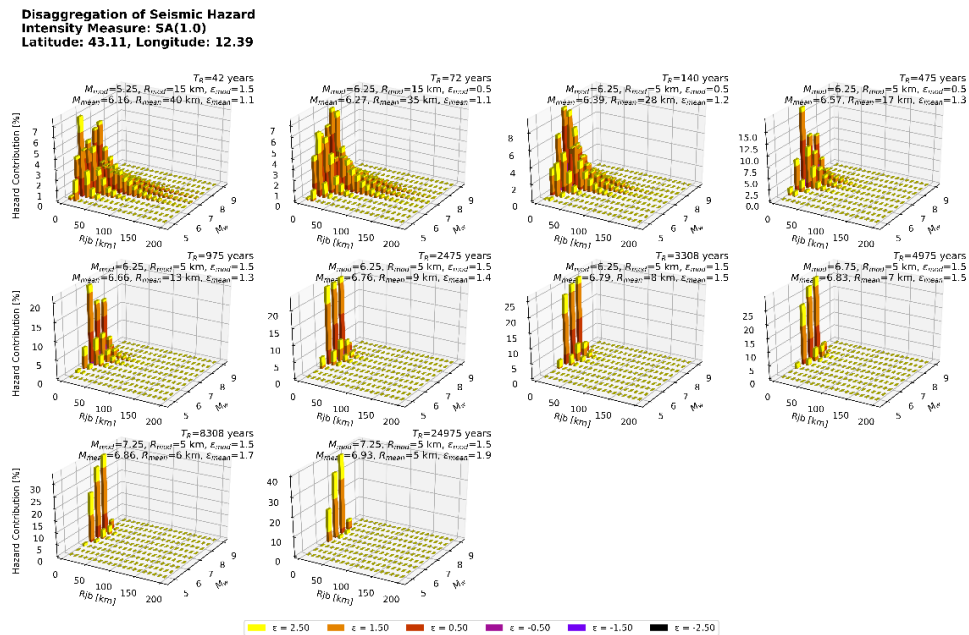


**Figure 14: Hazard disaggregation at site for the ten  $SA(1.0s)$  levels**

Record selection was performed following the procedure and algorithms proposed by Jayaram et al. (2011) at all  $IMLs$ . This algorithm selects and scales arbitrary records and tests their compliance with the target's mean and variance. For the records selected using  $AvgS_a$  as conditioning  $IM$ , this process was done following Kohrangi et al. (2017), who employ a modified version of the previously mentioned algorithm.

A relevant issue that should always be considered during the record selection, and that might impact the results shown in the following sections, is the accuracy in matching the target spectrum or, in other words, how much hazard-consistent the selected ground motions really are. Poor matching may mask differences in the responses that may be caused by intrinsic differences in the ground motions. That said, to quantify the goodness of fit with the target spectrum for the selected sets of records, we used



## D5.1 Methodology for selecting ensembles of rock-hazard consistent ground motions for fragility curve computations and datasets for WP6

the weighted sum of squared errors in the spectra's mean and dispersion,  $SSE_s$  (Baker & Lee, 2018), at the spectral ordinates of interest shown in Equation (3). Based on our implementations, and through visual inspection of the selected sets, a good fit of the target can be considered up to a limit of  $SSE_s$  of 0.1.

After selection, each record set was subjected to a series of tests to assess whether their seismological characteristics and the structural responses they caused were statistically indistinguishable from those of the benchmark cases.

The seismological tests mainly consisted of evaluating, for each family of selected records, the distribution of causative parameters (i.e., magnitude and distance) and the distribution of intensity measures, such as  $PGA$ ,  $Husid$  duration,  $CAV$ ,  $AI$  and spectral intensity ( $SI$ ), not made explicitly hazard-consistent in the  $CS$  approach. Possible differences in the distributions of these other  $IMs$ , if any, may cause systematic differences in the responses by  $CS$ -consistent records of different groups.

The seismic response of structures is evaluated through a set of SDOF systems, with different fundamental periods, to encompass a wide array of possible structures and estimate if there are differences in the record sets that can be sensitive to the structures' fundamental frequency. The SDOF systems are modelled using the OpenSees software (McKenna et al., 2000). Additionally, the systems were modeled with two hysteretic force-displacement behaviors, namely the pinching model with cyclic and in-cycle degradation, and the (non-degrading) elastic-hardening model shown in Figure 15.

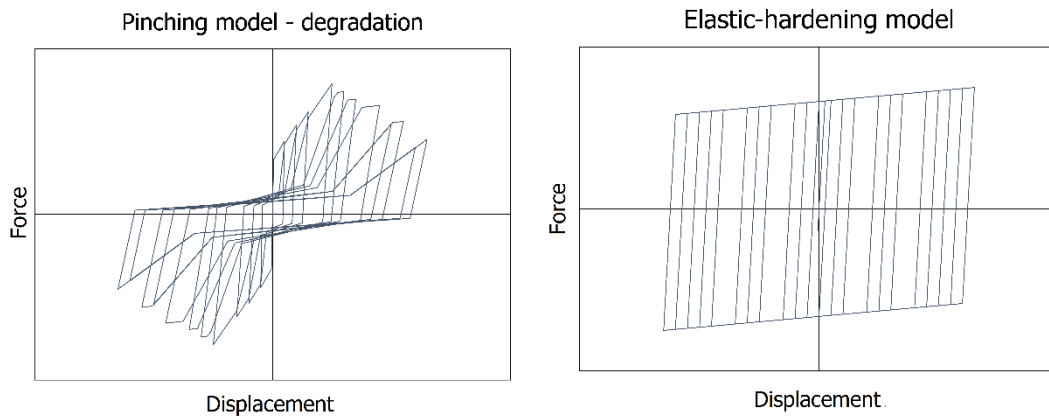


**Figure 15: Material models of the SDOF systems**

The characteristics of the different models are summarized in Table 4. These systems were designed with a lateral strength equivalent to that of the PSHA-based spectral acceleration value of 10% in 50 years ( $IML$  4) at the fundamental period of the SDOF. The corresponding yield base shear coefficient  $C_y$ , i.e., the yield base shear  $V_y$  normalized by the weight  $W$ , numerically equivalent to the yield spectral acceleration  $Sa_y$  in units of  $g$ , namely  $Sa_y/g = V_y/W$ , is obtained by  $C_y = Sa_{des}(T_1) \cdot \Omega/q \cdot g$ , where  $Sa_{des}(T_1)$  is the design spectral acceleration at  $T_1$ ,  $q$  is the behavior factor assumed equal to 4.0 for new ductile buildings, and  $\Omega = 2$  is the over-strength factor. Accordingly, the corresponding yield displacement,  $\delta_y$ , of the SDOF is obtained by  $\delta_y = Sa_y \left[ \frac{T_1}{2\pi} \right]^2$

SDOF models were subjected to  $NLTHA$  assuming a 5% mass proportional Rayleigh damping and using different record sets as an input. The responses in terms of peak displacements (and ductility), peak accelerations, peak velocities, and total hysteretic energy were monitored on all the structural systems for all records. A ductility value of 8 or larger was considered as collapse for all the structural systems considered. Here, the displacement, acceleration, and velocity demands are taken as the maximum absolute value found in the analysis, while the hysteretic energy is computed by integrating the force-displacement response throughout.

T [sec]	Material model	T [sec]	Material model
0.2	Elastic-hardening	0.2	Degrading
0.5	Elastic-hardening	0.5	Degrading
1.0	Elastic-hardening	1.0	Degrading
1.5	Elastic-hardening	1.5	Degrading
2.0	Elastic-hardening	2.0	Degrading

**Table 4: Numerical models summary**

The responses of SDOF systems to different groups of *CS*-consistent records were screened for any statistical or systematic differences through visual inspection aided by hypothesis testing, as discussed in the following subsections.

### 3.1. Soil and rock ground motions for CS-based hazard

This section investigates the possible effects of using *CS*-consistent ground motions recorded at soil stations in place of (or in addition to) rock ground motions for structural response assessment of SSCs. In the application at hand, PSHA and disaggregation are performed for rock site conditions and, consequently, rock ground motions should be used for developing fragility curves for SSCs, as these sites do not present any amplification due to soil effects. However, ground motions recorded on rock sites are not plentiful and this scarcity of rock records can negatively impact the matching of the target *CS*-spectrum leading to fragility curves that are not hazard-consistent and, therefore, inaccurate for site-specific risk assessment. Here, we investigate whether any statistically significant differences in the response of SDOF systems arise when one uses *CS*-consistent suites of ground motions recorded either on rock or on soil.

#### 3.1.1. Record sets and selection

The ground motions in the database were first classified into soil and rock records according to both definitions of rock sites adopted here: the  $V_{S30}$  and the Complex methods. The final ground motion groups considered here for record selection are: Rock/ Soil Complex, Soil  $V_{S30}$  ( $V_{S30} < 400$  m/s) and Rock  $V_{S30}$  ( $V_{S30} > 800$  m/s). Additional sets of more extreme cases ( $V_{S30} < 300$  m/s or long-duration records) were also evaluated but did not alter the conclusions presented herein.

From these four groups, we extracted different suites of ground motions matching the *CS* for the site in Perugia at the 10 different *IMLs* discussed earlier. As *IMs*, we considered  $AvgS_a$  and  $S_a(T_1)$ , as listed in Table 3. For the following tests, from each one of these 4 groups we selected sets of 40 records per *IML* allowing a maximum scaling factor of 10. This generous scaling range allowed us to select suites of records that achieved a statistically robust *CS* match even at high IM levels. Using more than 40 records would be impractical for any engineering application. As an illustrative example, Figure 16a shows the  $SSE_s$  error, calculated using Equation (3) for all 10 *IMLs* when  $AvgS_a$  was used as conditioning IM. While  $SSE_s$  values for the record sets selected from the soil databases remain lower than the good-fit 10% threshold value through all the *IMLs*, the corresponding record sets selected from the rock databases for the highest three *IMLs* exceed the threshold. This happens mainly due to the scarcity of rock records for high intensities, as highlighted in the previous section. Figure 16b compares the selected mean and mean  $\pm 2\sigma$  versus the corresponding  $AvgS_a$ -based *CS* target for *IMLs* 2, 6 and 10. Notice that, despite the  $SSE$  being larger than the 10% threshold, the match at *IML* 10, at least in the mean, is still visually pretty accurate.

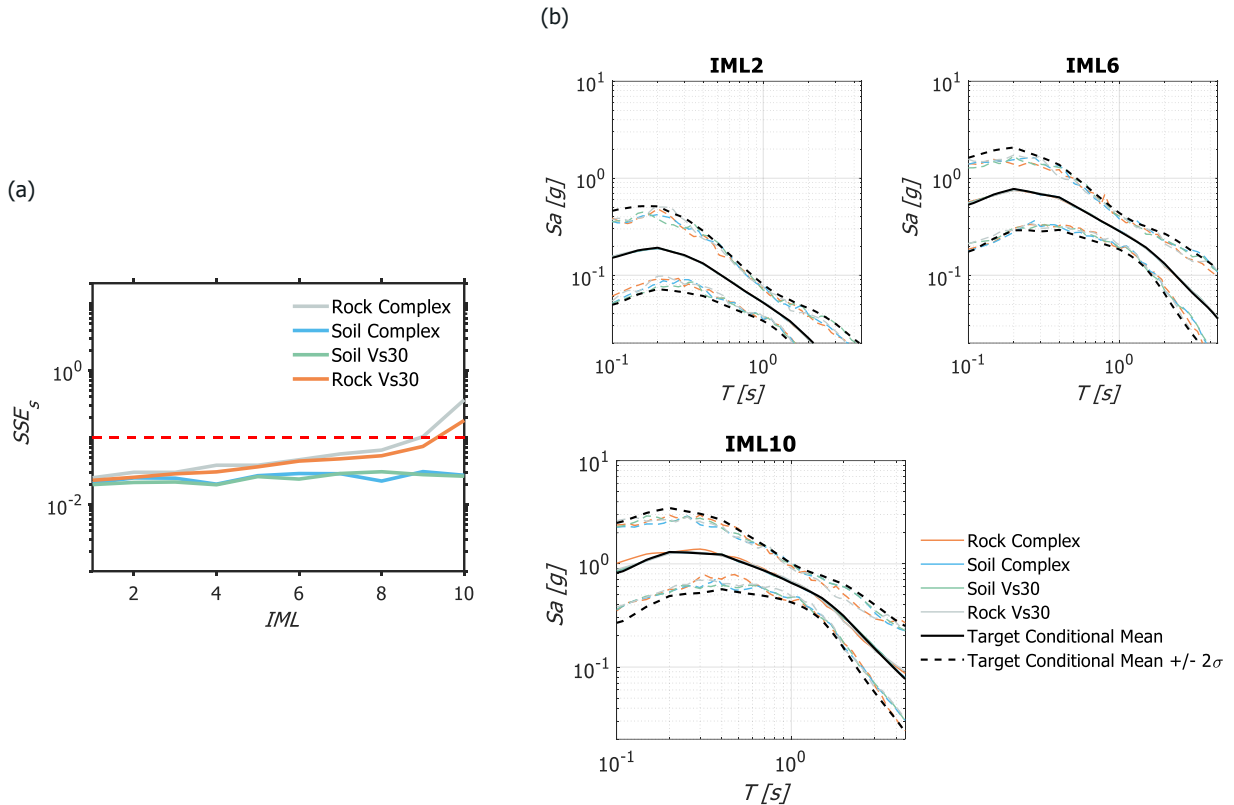


**Figure 16: comparison (a)  $SSE_s$  test, and (b) spectral shape for  $AvgS_a$ -based CS selection of rock and soil records**

Although a discussion on scaling factors is not the focus of this section, the results shown in Figure 17 indicate that, generally, higher scaling factors are required to achieve a good fit for the case of rock ground motions since they have lower spectral accelerations overall. This consideration is relevant since limiting the scaling factors would reduce the number of records available at a given  $IML$ , which would negatively impact the target match at higher intensities.

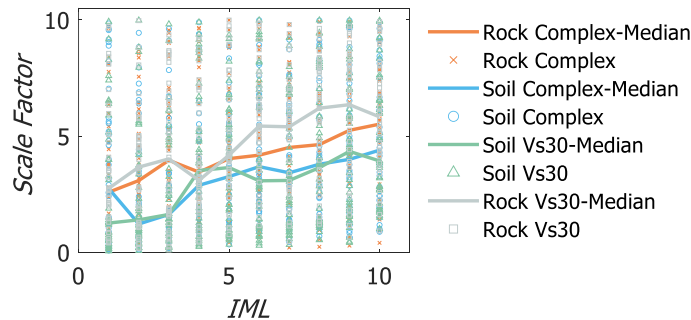


**Figure 17: Scale factor for  $AvgS_a$ -based CS-consistent soil and rock ground motions at the 10  $IMLs$**

### 3.1.2. Structural Response to CS based hazard consistent records

Generally, none of the results, across all the period ranges and structural systems, show any significant differences in the responses for all the tested metrics perhaps with the exception of the highest  $IMLs$  for the rock complex case. However, the differences observed at the highest  $IML$  can be attributed more to the imperfections in matching the target spectrum rather than to intrinsic differences in rock vs. soil records.

This can be seen in Figure 18, which shows the ductility response of the structures to the ground motions consistent with the  $AvgS_a$  – based CS across all  $IMLs$ . One should note that the cases where ductility is

higher than 8 are treated as collapse cases and are lumped in the figure on the dashed horizontal grey line. Of course, when more than 50% of data points are collapse cases, the median ductility is infinite and hence it is omitted in the figure. Both the mean and dispersion for all four cases are practically the same, as confirmed by hypothesis testing where the null hypothesis could not be rejected at the 5% significance level between all groups for most *IMLs*. It can be noticed from these figures that the system with degradation shows higher dispersion overall once the nonlinear behavior starts (*IML* > 4). Additionally, the degradation systems do exhibit cases where collapse is assumed to happen ( $\mu \geq 8$ ), this is most noticeable in the system with a  $T = 0.2s$ , where after *IML* 5 the majority of analyses exceed this limit and, hence, the curve stops at that level. While not shown here, the same considerations apply to the  $Sa(T_1)$  – based *CS* selection at the different fundamental periods of the SDOF systems, no significant differences were found in any of those cases as well.

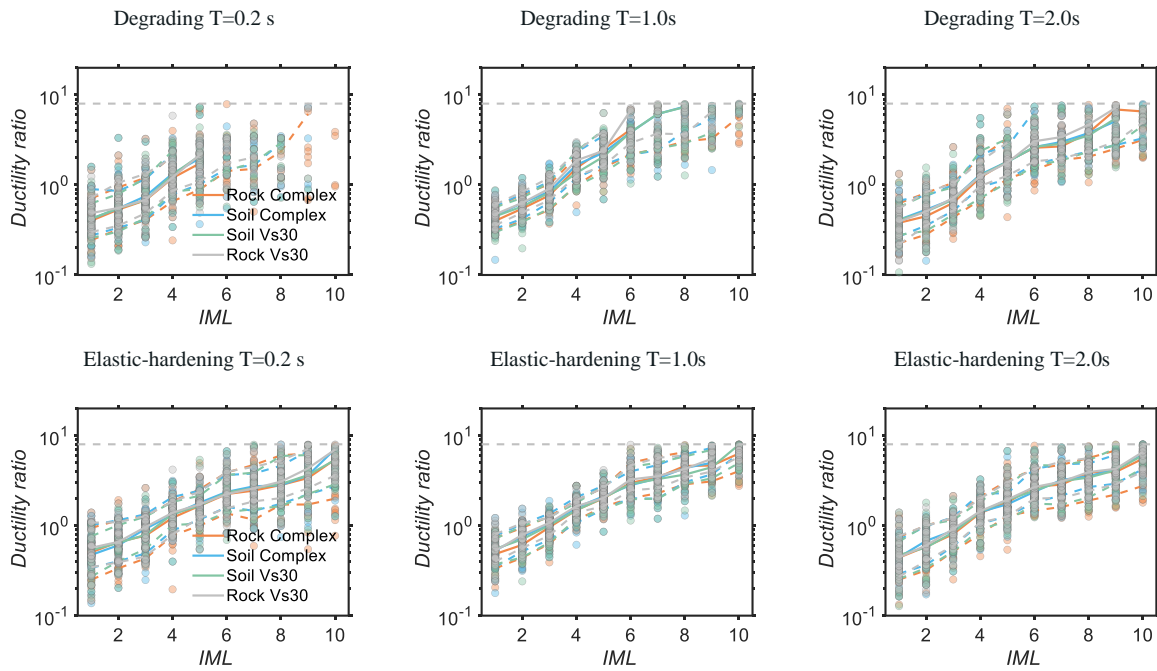


**Figure 18: Ductility response of SDOF systems**

Figure 19 and Figure 20 lead to the same conclusions overall, as no significant differences can be observed on the figures both in terms of mean and dispersion for peak acceleration and velocity on any of the SDOF systems. Similarly, hypothesis testing confirmed that the distributions are statistically indistinguishable for all the acceleration responses and the null hypothesis was rejected at the 95% confidence level only at the highest *IML* for the  $T=1s$  velocity responses for the system with degradation.

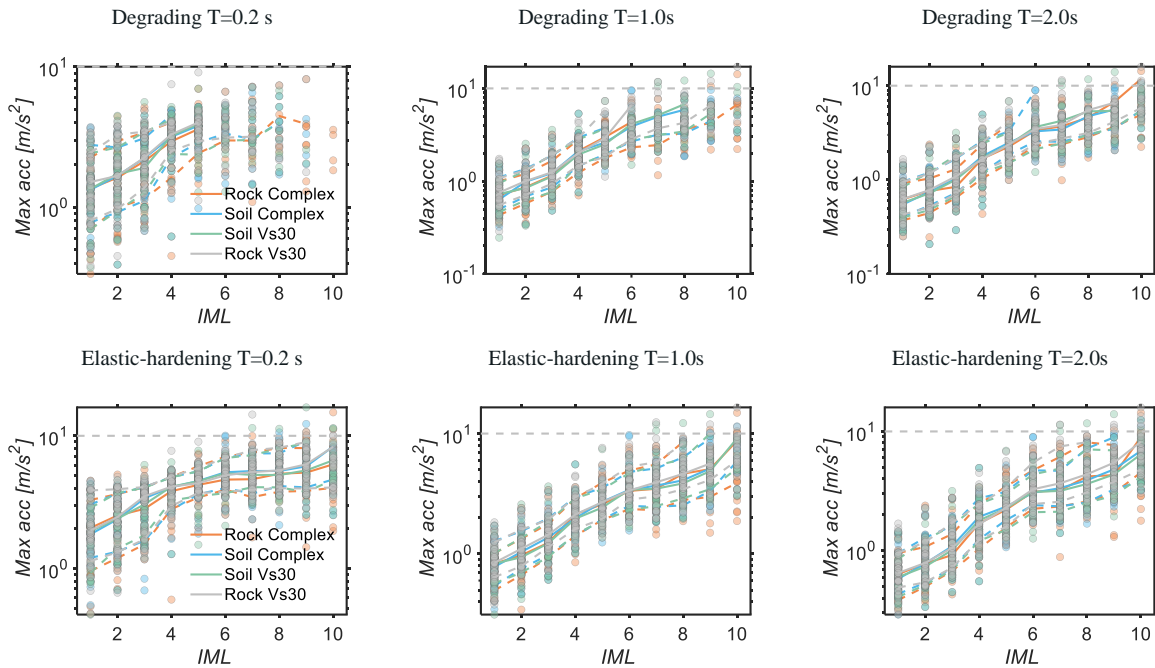


**Figure 19: Peak acceleration response of SDOF systems**

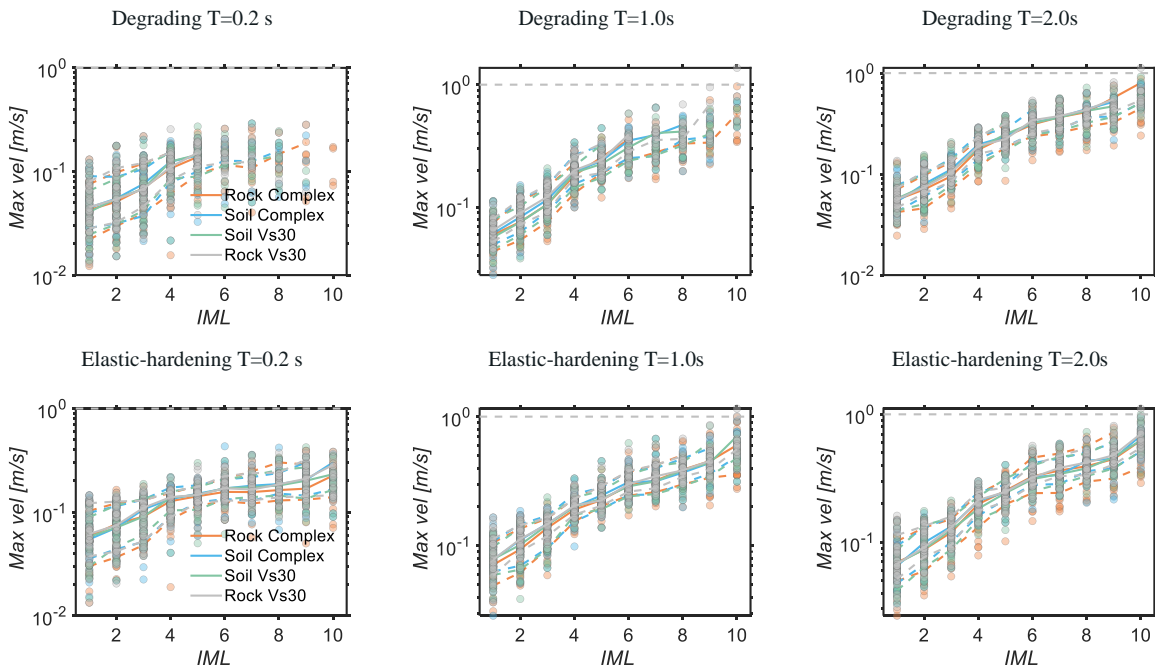


**Figure 20: Peak velocity response of SDOF systems**

Finally, we evaluate the possible differences in the energy response, normalized by the system's equivalent monotonic energy, which are shown in Figure 21. This EDP chosen was computed to investigate whether the longer duration normally found on soil records, could have an impact despite having the same distribution of spectral ordinates as the rock records. Findings show, somewhat unexpectedly, no significant differences, a consideration that was confirmed both visually and through hypothesis testing.

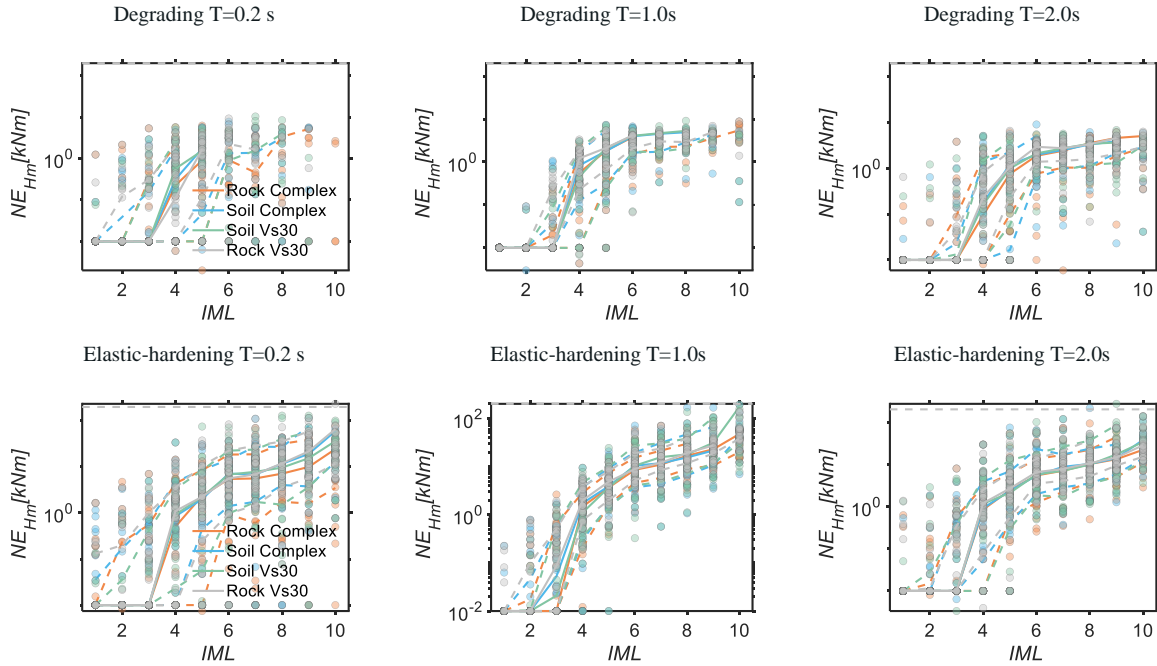


**Figure 21: Hysteretic energy response of SDOF systems**

These findings are in contrast with those, for example, of Chandramohan et al. (2016), who have tested the influence of duration on the collapse of structures and concluded that longer duration has a significant impact on structural collapse, a phenomenon expected to be captured by the dissipated energy. The reason we do not observe this in our results is that the two distributions of significant duration of rock and soil records selected to be *CS* – consistent are very similar (Figure 19): the mean duration of records is only longer by a couple of seconds, which is a difference much smaller than that of what people in the literature have called long and short duration records. According to Chandramohan et al. (2016), typically records would be classified as short duration when their  $D_{5-75}$  is lower than 25s. Figure 22 shows that overall, the selected records have a significantly shorter mean duration when compared to the entire database, which indicates that *CS*, while enforcing the target's spectral shape to be consistent with the rock *CS*, automatically filters out longer records.

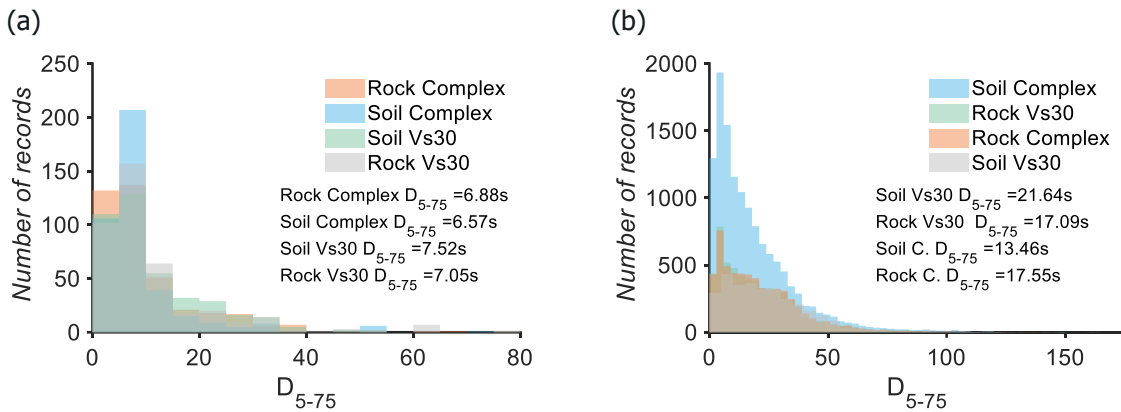


**Figure 22: Duration distribution of (a) selected records and (b) full database**

The difference between rock ground motion average response spectrum and that of soil ground motion of different durations can be appreciated by inspecting Figure 23, which displays the average spectra, normalized to  $PGA = 1g$ , of selected rock (target) and soil ground motions (classified through  $V_{s30}$ ) from the full database of increasing  $D_{5-75}$  duration. The shape of the response spectra of ground motions of long durations (30s and above) differs significantly from the shape of (usually shorter) rock ground motions. Therefore, the record selection algorithm with rock *CS* as a target tends to preferentially select



shorter rather than longer soil records and this explains the reason why the distributions of energy dissipated in the response of these SDOF systems is very similar.

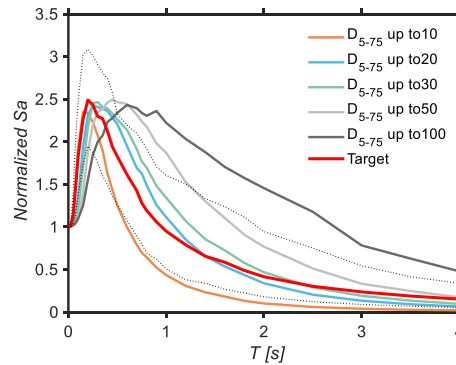


**Figure 23: Spectral shape for different durations of soil records**

### 3.1.2.1. Evaluation of Fragility Curves

Fragility functions (see Figure 24) are derived for three ductility-based damage states (DS): onset of damage (DS1) at  $\mu \geq 2$ , moderate damage (DS2) for  $\mu \geq 5$  and near collapse (DS3) defined by ductility values  $\mu \geq 8$ . Fragility curves are very sensitive to the tails of the distributions of the responses at each stripe of the analyses and, therefore, they may uncover differences between structural responses of rock and soil records not obvious in the analysis of mean and dispersions conducted in the previous subsection.

All estimates of the median capacity for DS1 are practically the same for all structures (with some slight differences in the dispersion). Across most  $CS - AvgSa$  curves, the lowest estimate of the median capacity for all DS is that obtained from the Soil  $V_{s30}$  group, with the exceptions of the elastic-hardening systems at  $T$  of 0.2 and 2 s where the Soil complex and Rock complex estimate becomes the lowest, respectively. This implies that fragility curves estimated through  $CS$  – consistent selection of pure soil records are slightly more conservative (i.e., higher probability of exceedance) than those obtained with rock-like ground motions. This is especially true for collapse fragility curves of elastic-hardening SDOFs, although for these structures the scarcity of collapse cases, even at the highest  $IML$  (note the continuous curves in Figure 18), makes the estimate of the fragility parameters for DS3 less precise. Note also that the increase of the variability in both median capacity and slope of the  $T=0.2$  and  $2.0s$  systems is also a product of using structures with periods that are on the extremes of the  $AvgSa$  range. This statement is corroborated by the results of  $CS - Sa(T_1)$  (shown below) which display less prominent discrepancies.

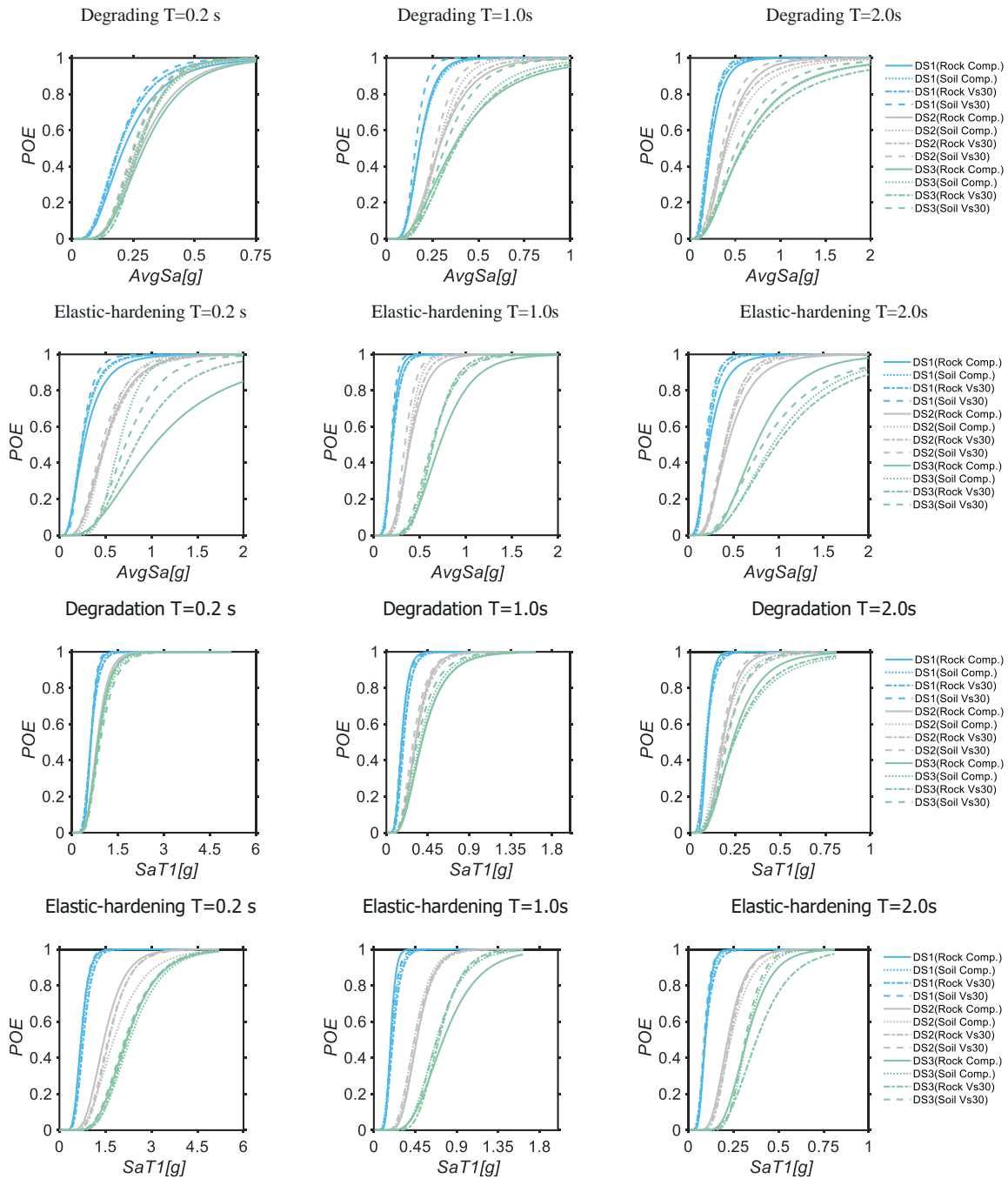


**Figure 24: Fragility functions for DS1 ( $\mu \geq 2$ ) and DS2 ( $\mu \geq 8$ ) for  $AvgSa_a$ (Top) and  $Sa(T_1)$  (Bottom).**

### 3.1.3. Structural Response to pairwise rock-soil ground motion records

The comparison of  $CS$ -based results is statistically robust but more work is needed to investigate the reason of the small differences in the responses that occur in some cases. Therefore, we designed an experiment where we paired 135 unscaled rock ground motions with 135 soil ground motions (scaled between a factor of 0.5 and 5) in such a way that a) the magnitude and distance of the rock record ( $M_r$  and  $R_r$ ) are very similar to those of the soil record ( $M_s$  and  $R_s$ ) and b) the spectral shape of the soil record in a any pair matches, to the extent possible, that of the rock record in the same pair. Figure 25 shows one such a pair. The iterative procedure adopted for matching the soil records to a similar rock record is akin to that proposed in Chandramohan et al. (2016) for short and long duration records.

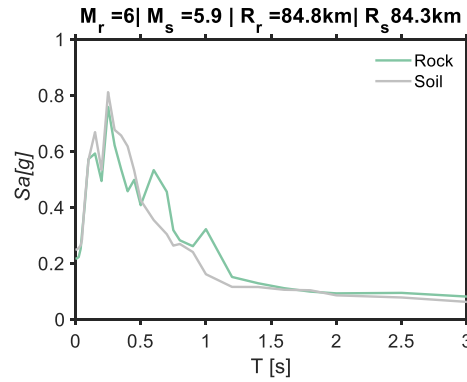


**Figure 25: Example of paired (i.e., spectrally similar) rock and soil motions**

Then, the response of the same set of SDOF structures considered earlier is computed via nonlinear time history analysis for the rock and soil record pairs and the performance is monitored using the same EDPs. Figure 23 shows for each pair the ratio of the maximum drift caused by the soil ground motion,  $\delta_{max,s}$ , to that of the rock ground motion,  $\delta_{max,r}$ . The same Figure contains also the ratios computed for the other three EDPs. While differences in the responses do exist across the various SDOF systems, the median value for all of these EDP ratios is close to 1.

These results support the conclusion that, while there are differences in the responses for a single rock and soil motion pair, on a large assessment, using a record set that was selected through using *CS*, the median responses are expected to be very similar for either rock or soil motions provided that the spectral shapes are consistent.

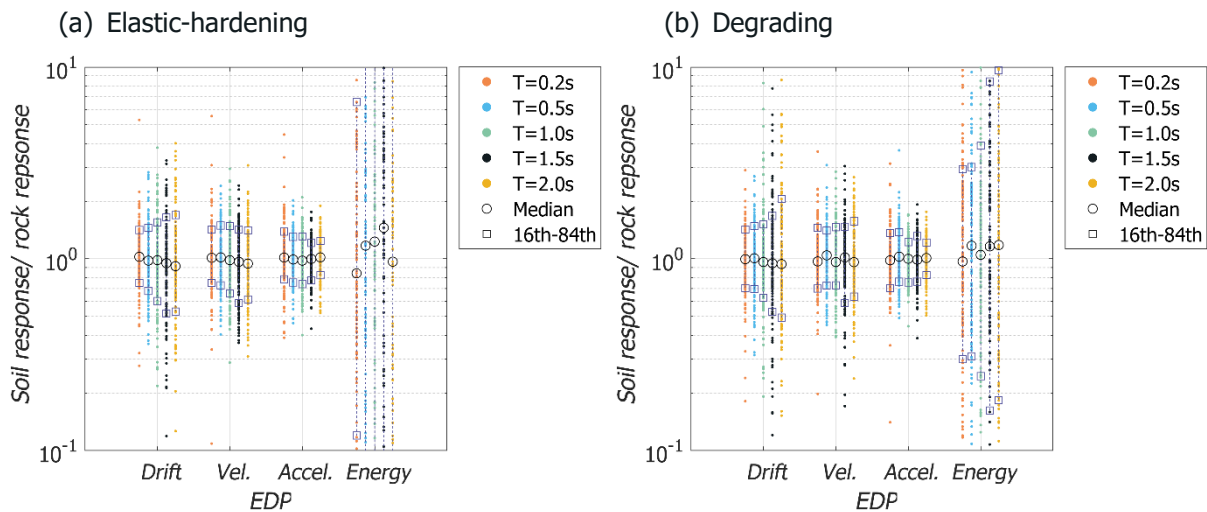


**Figure 26: Ratios of soil to rock responses measured by maximum drift, acceleration, velocity and dissipated energy computed using the pairwise record analyses**

### 3.1.4. Seismological parameter comparisons

The selected record sets were subjected to a set of seismological tests aiming at identifying possible systematic differences of other IMs and of characteristics of the causative events that could perhaps be responsible for the (small) response discrepancies that were found in the previous subsections.

Figure 27 shows the magnitude-distance scattergram of all the events that generated the ground motions in the different record sets color-coded by *IML*. The most noticeable difference here is the larger spread of the scattergram for the soil cases compared to the rock ones. The rock Complex and, to a lesser extent, the rock  $V_{s30}$  groups seem to have records of similar magnitude and distance bins per *IML*. Notice also the lack of rock ground motions from high magnitude event recorded at a short distance. Contrarily, the soil groups use records from a wider array of magnitude and distance bins for

all *IML*, with high-intensity records coming from an assortment of *M* and *R* combinations. This consideration matters if one were to use the *CS – MR* variant of the conditional spectrum approach, which imposes restrictions on the causative parameters to ensure consistency with the parameters of the events most contributing to the hazard. The selection of rock records will encounter more limited options.

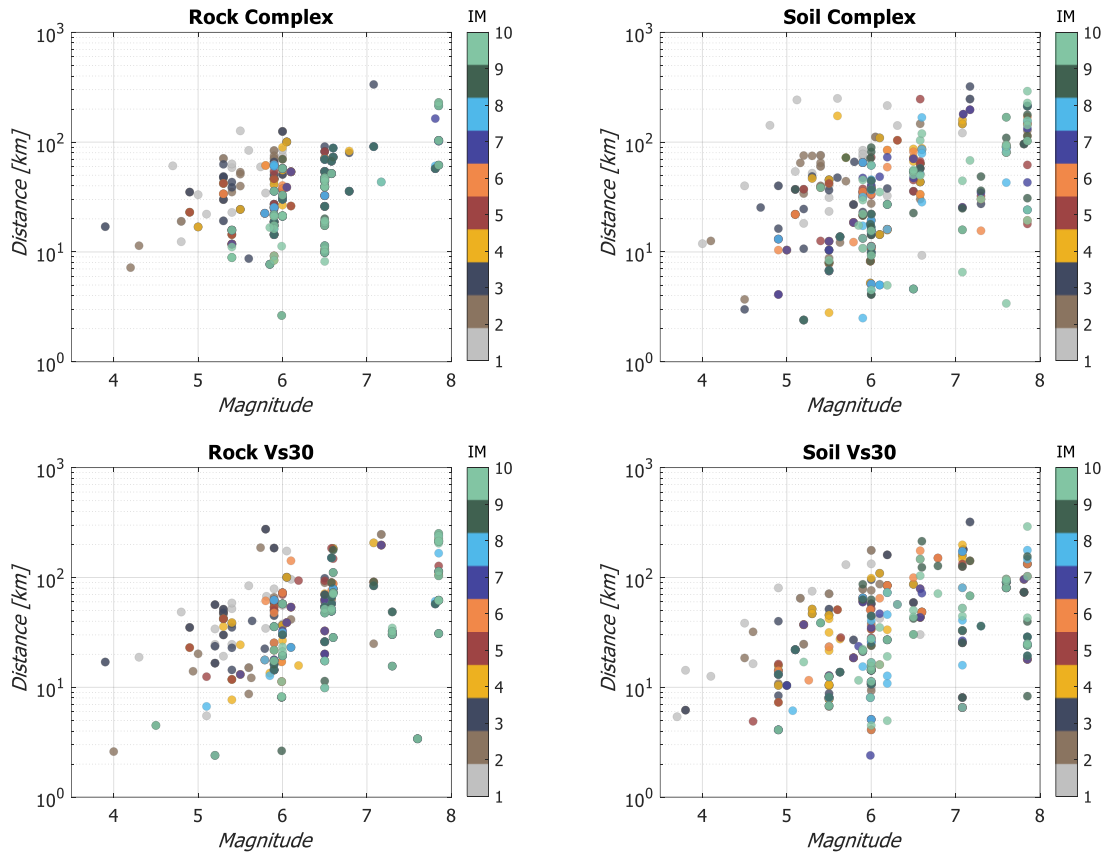


**Figure 27: Magnitude-distance scattergram of the causative earthquakes of the four record sets, colours indicate IM level**

Figure 28 shows the differentiation between rock and soil records in terms of  $V_{s30}$ , which is imposed by design.  $V_{s30}$  is one of the criteria used to separate soil from rock sites in the complex classification scheme and the only criterion in  $V_{s30}$  classification scheme. It is still worth noting that some of the records from the soil and rock complex groups have  $V_{s30}$  values that would normally not be associated to sites of that soil type (e.g., Rock motions of  $V_{s30} < 600\text{m/s}$ , soil motions with  $V_{s30} > 700\text{m/s}$ ).

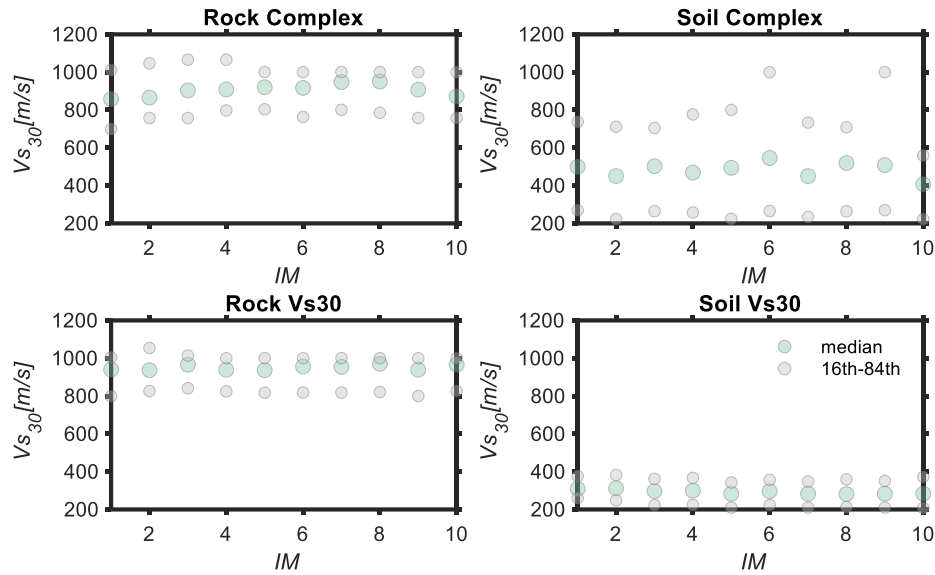


**Figure 28:  $V_{s30}$  distribution for the selected record sets arranged by  $L$  .**

Figure 29 shows the median and dispersion values for all these considered metrics for each record group for the ten  $IML$ s. Observations in terms of both visual inspection and hypothesis testing are presented next.

The results in terms of  $PGA$  show that all records share the same median value across all intensities and types, with the exception of  $IML$  10, where there is a substantial difference between rock records and soil records. This difference can be attributed to the imperfect matching of the target  $CS$  spectrum at that  $IML$  when only rock records are used. Husid duration is the metric that shows the largest difference among groups for all  $IML$ s. The soil record group with an average lower  $V_{s30}$  has the highest values of Husid duration across all  $IML$ s, while the rest are equal according to hypothesis testing. This finding suggests that the soil ground motions recorded at sites with very low  $V_{s30}$  tend to have longer durations than that those of other groups but not sufficiently longer to change the structural response in a noticeable way. The  $CAV$  results, based on both visual and hypothesis tests, show that they are equal in almost all  $IML$ s for all groups, with few minor exceptions in the soil  $V_{s30}$  group. The  $AI$  values remain the same across all soil and rock types for all  $IML$ s, except for the rock complex case at  $IML$  10 where, again, the changes can be attributed to the issues in matching the target for that record set. The same conclusions can be drawn for the  $SI$  values.

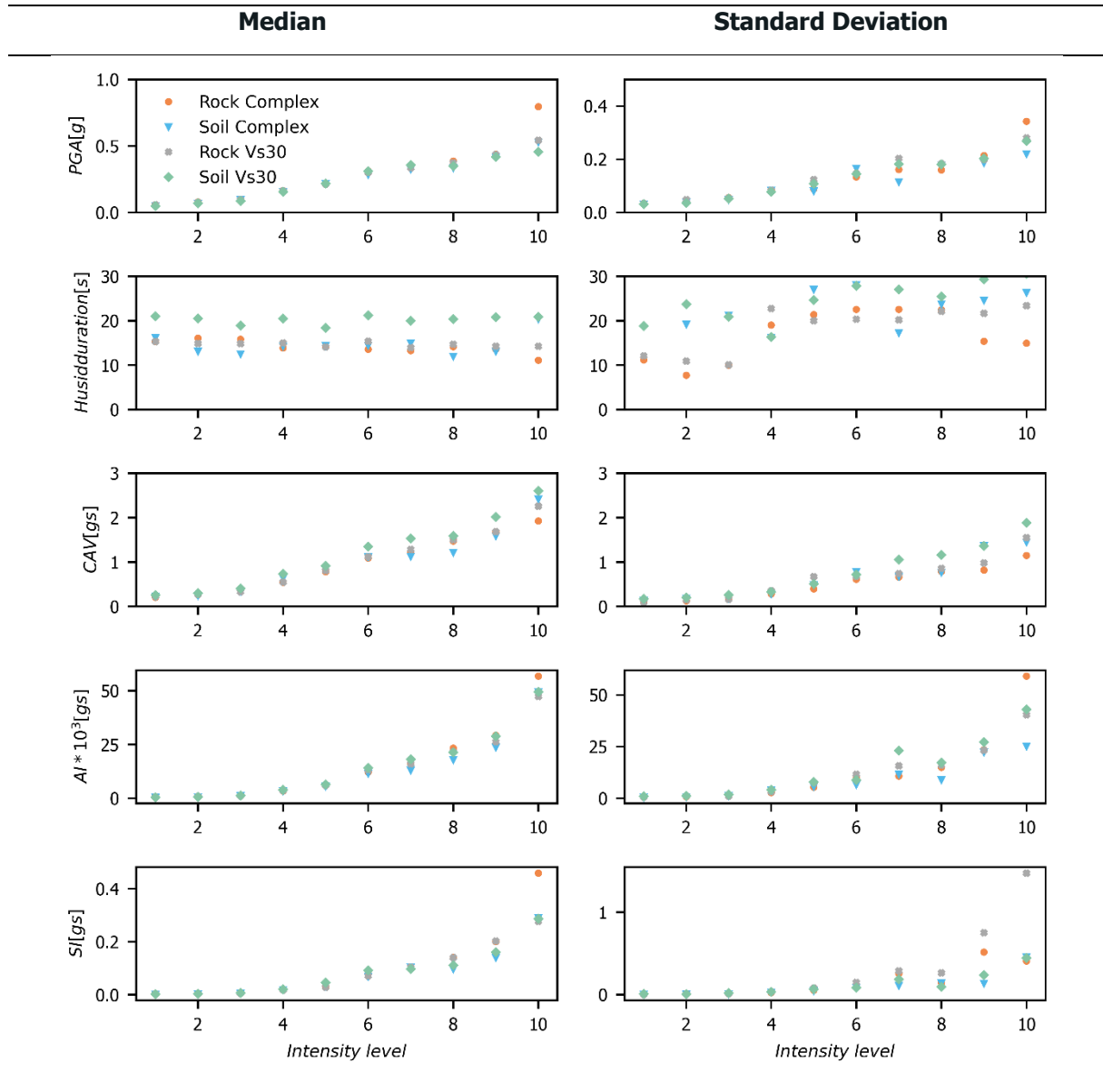


**Figure 29: Distribution of different  $IM_s$ , namely peak ground acceleration ( $PGA$ ), Husid duration, Cumulative absolute velocity ( $CAV$ ), Arias intensity ( $AI$ ), and Spectral intensity ( $SI$ ), from first to the last row, respectively, in terms of median and standard deviation for the case of  $AvgSa$ .**

These tests confirm the previous observations, reinforcing the notion that using a  $CS$ -based ground motion selection scheme, which enforces the hazard consistency in terms of spectral shape, produces a family of records that are statistically very similar. The small differences noted are not large enough that the hazard-consistent sets of selected records from soil or rock stations cause any significant differences to the SDOF responses studied here. While some of the event's characteristics, such as causative parameters or  $V_{S30}$ , have may have some differences, the  $IM_s$  that are better correlated with the response EDPs do not. Therefore, ground motions coming from different sources other than reference stations are not expected to alter any of the results in a significant way, as long as there is a careful selection and a sufficiently good match of the target  $CS$ . Of course, it remains to be seen how these findings will scale up to a multi-degree-of-freedom NPP model.

## 3.2. Scaled ground motions for CS-based hazard

With the rise of the methods for record selection, several studies investigated using different methods to check whether amplitude scaling might introduce bias in structural response estimates. Luco and Bazzurro (2007) used different SDOF and MDOF systems to show that ground motion scaling can bias the nonlinear drift response. They anticipated that this bias might be avoided once the spectral shape is accounted for within the record selection, as confirmed later by Baker (2007), who used *CMS* for record selection. On the contrary, Dávalos and Miranda (2019) recently claimed that high scaling factors could induce bias in displacement demands and collapse estimates when records are selected using the *CMS*.

That said, this section proposes a methodology to test whether scaling the records, selected with *CS*, can lead to biased results. For every *IML*, and every considered SDOF system, we define two groups of records: (1) minimally scaled group with a scaling factor between 1 and 2 (low scaling factor, or LSF, in the following text), and (2) group with high scaling factors, between 7 and 10, (HSF in the following text). As in Section 3.1 these two sets of records are subjected to a battery of engineering and seismological tests. We consider here only SDOFs with degrading behavior (Figure 15).

### 3.2.1. Record sets and selection

We select 40 hazard-consistent records using  $Sa(T_1)$  as the *IM* for the two defined groups and three different conditioning periods:  $T_1 = 0.2s$ ,  $T_1 = 1s$ , and  $T_1 = 2s$ , for all *IMLs*. Figure 30 shows the  $SSE_s$  error, calculated with Equation (3) for different conditioning periods. The threshold of 0.1 is defined as an acceptable error level, as explained in the previous section. One can note that the match in all cases is good except for *IML* 10 and  $T_1 = 2s$ , where small exceedance of the threshold is observed.

The records are selected using the GMRotI50 (the orientation-independent measure) to be consistent with the selected GMPE of Boore and Atkinson (2008) used for hazard analysis. For each chosen record, we run NLTHA for each of the ground motion components. In this manner, we run 80 analyses for every stripe and every SDOF system.

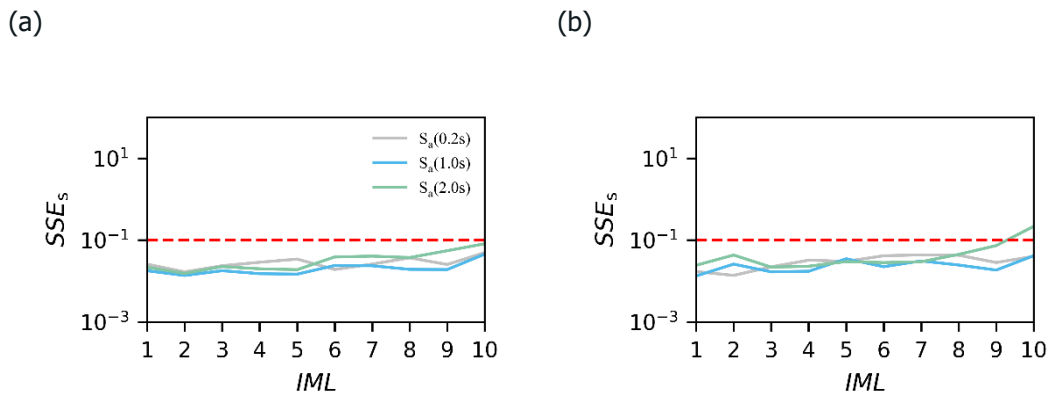


**Figure 30:  $SSE_s$  for the (a) LSF and (b) HSF record sets for different conditioning periods**

### 3.2.2. Structural response to CS-based hazard consistent records

Figure 31 presents the median results of the nonlinear time history analysis for the LSF and HSF sets of selected records in terms of the same four different EDPs considered earlier for the three SDOF systems. Sub-figures (a) to (d) show ductility, maximum acceleration, maximum velocity, and dissipated energy, respectively. A visual inspection of these figures indicates that the set of records with high scaling is yielding higher responses in all cases; however, these differences are not significant as the results of the hypothesis tests across all EDPs and *IMLs* indicate that the null hypothesis (i.e., that the differences are equal to zero) could not be rejected at the 5% significance for all SDOFs.

As stated in previous sections, the cases where the obtained ductility is higher than 8 are treated as collapse cases and are lumped in the figure on the dashed horizontal grey line.



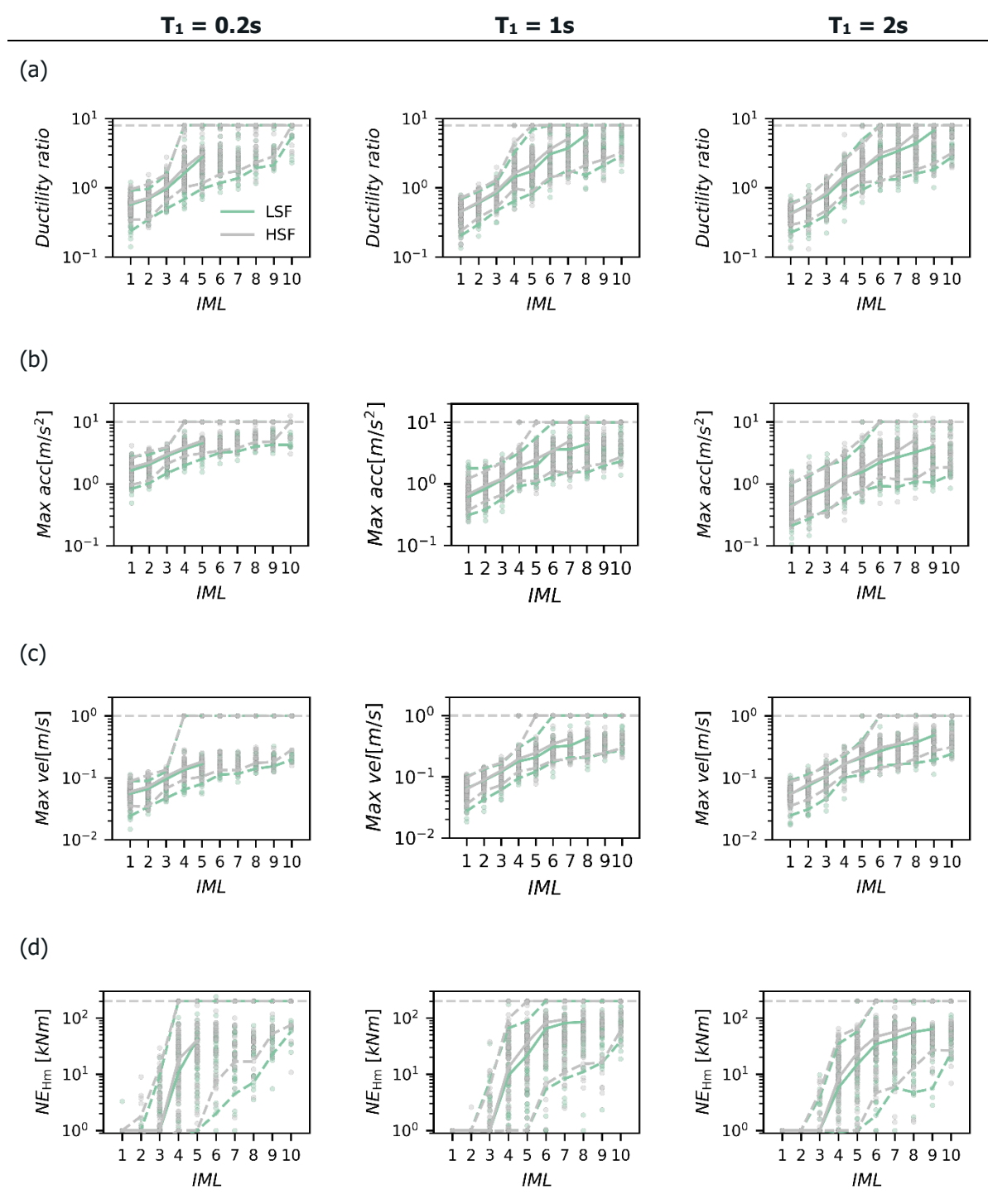


**Figure 31: Results of nonlinear time history analysis using 40 selected records at each IML, for the LSF and HSF sets of ground motions. Median (solid line) and 5<sup>th</sup> and 95<sup>th</sup> percentiles (dashed lines) are illustrated for different EDPs: (a) max ductility, (b) max acceleration, (c) max velocity, and (d) hysteretic energy.**

Going a step further, we show in Figure 32 the probabilities of exceeding different ductility levels ( $\mu=2$ , 5 and 8) of the considered SDOFs when experiencing ground motions of increasing severity. These results could be interpreted as fragility curves for three different damage states, such as onset of damage, moderate damage, and near collapse. One can notice that for all SDOFs the HSF group yields higher exceedance probabilities for all ductility levels. For ductility level of  $\mu=2$ , these differences are

## D5.1 Methodology for selecting ensembles of rock-hazard consistent ground motions for fragility curve computations and datasets for WP6

very small for SDOFs with  $T_1 = 1\text{s}$  and  $T_1 = 2\text{s}$  (i.e., increase in median  $Sa(T_1)$  in LSF is  $\sim 8\%$ ), while for the stiffer SDOF with  $T_1 = 0.2\text{s}$  a slightly higher difference can be observed (i.e., increase in median  $Sa(T_1)$  in LSF is  $\sim 14\%$ ). For ductility level of  $\mu=5$ , however, the highest difference is observed for the SDOF with  $T_1 = 2\text{s}$  (i.e.,  $\sim 22\%$ ) while  $T_1 = 0.2\text{s}$  and  $T_1 = 1\text{s}$  show smaller discrepancies. Lastly, for the near collapse case ( $\mu=8$ ), a similar trend is observed for SDOFs with  $T_1 = 1\text{s}$  and  $T_1 = 2\text{s}$  with the increase of  $\sim 24\%$ , while stiffer system shows smaller differences of  $\sim 13\%$ .

The better understand these differences we run the battery of seismological parameter comparisons in the following section.

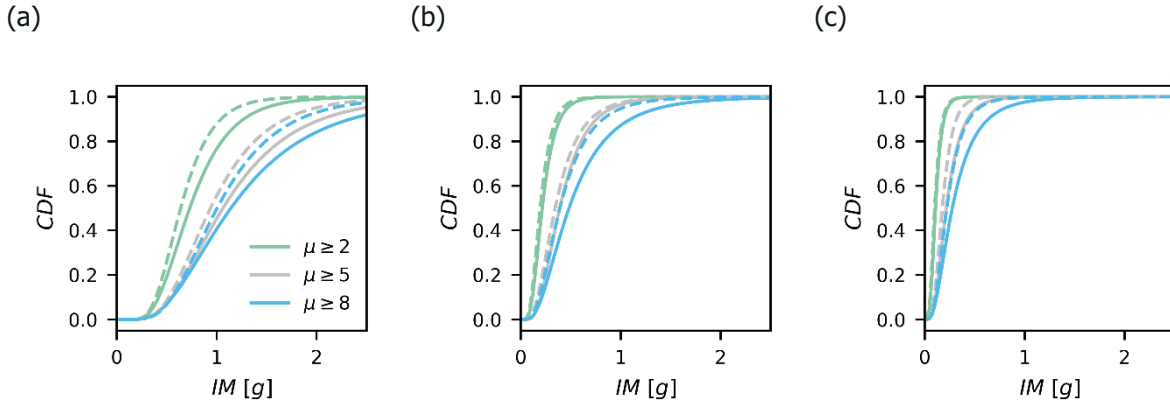


**Figure 32: Comparison between the fragility curves obtained from LSF (solid line) and HSF (dashed line) groups for three different ductility levels and SDOF with: (a)  $T_1=0.2\text{s}$ , (b)  $T_1=1\text{s}$  and (c)  $T_1=2\text{s}$ . Label on the x axis refers to  $Sa$  [g] at the fundamental period of the corresponding SDOF system.**

### 3.2.3. Seismological tests

We first look at the distribution of  $M_w$ ,  $V_{S30}$  and  $R_{jb}$  for the two sets of records. We show here only results for the conditioning period of  $T=1\text{s}$ , for brevity, as similar results were observed in other cases. It is noticeable that for the first 7  $IMLs$ , the median  $M_w$  of selected records is higher for the set with lower scaling factors, a finding that does not come as a surprise. To achieve the same intensity level with a lower scaling factor, the original ground motions must have been generated, on average, by larger magnitude events. For the very high  $IMLs$ , however, these differences vanish as even with the considerable scaling of the HSF group, ground motions generated by high magnitude events are necessary to reach the desired large  $IMLs$ . Similarly, the median  $R_{jb}$  of the HSF records is higher than the one of the LSF record set due to the same reasons. Regarding the differences in median  $V_{S30}$  there is no clear pattern as the two sets yield very similar results for some IM levels while for others (e.g.,  $IMLs$  7-9) there are some more noticeable differences.

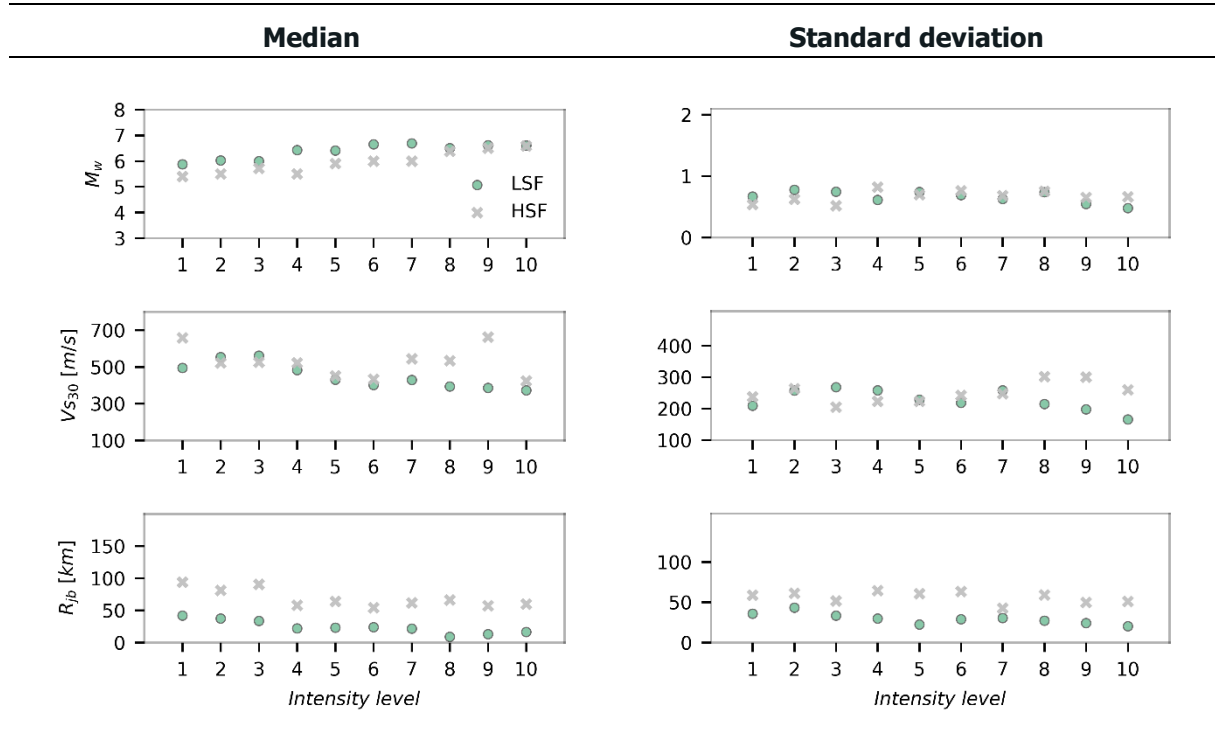


**Figure 33: Distribution of  $M_w$ ,  $V_{s30}$  and  $R_{jb}$  in terms of median and standard deviation for the case of  $T_1=1s$ .**

$IMs$  other than spectral quantities are not controlled by the  $CS$  approach. Similarly, as in the case of structural response, we performed hypothesis tests for seismological parameters across all  $IMLs$ , finding that the null hypothesis could not be rejected at the 5% significance for  $PGA$  and  $SI$ . In the case of Husid duration,  $CAV$ , and  $AI$ , however, the hypothesis was rejected (the HSF group has consistently higher values across all  $IMLs$ ). Even though the duration is not directly affected by the scaling (i.e., scaled and unscaled records have the same duration), the differences obtained can be attributed to the fact that records in the HSF group originate from events with higher  $R_{jb}$  values, seen in Figure 33. These higher  $R_{jb}$  values are due to the fact that HSF group requires high scaling factors and hence naturally weak ground motions (that are usually associated with lower magnitudes and higher distances).

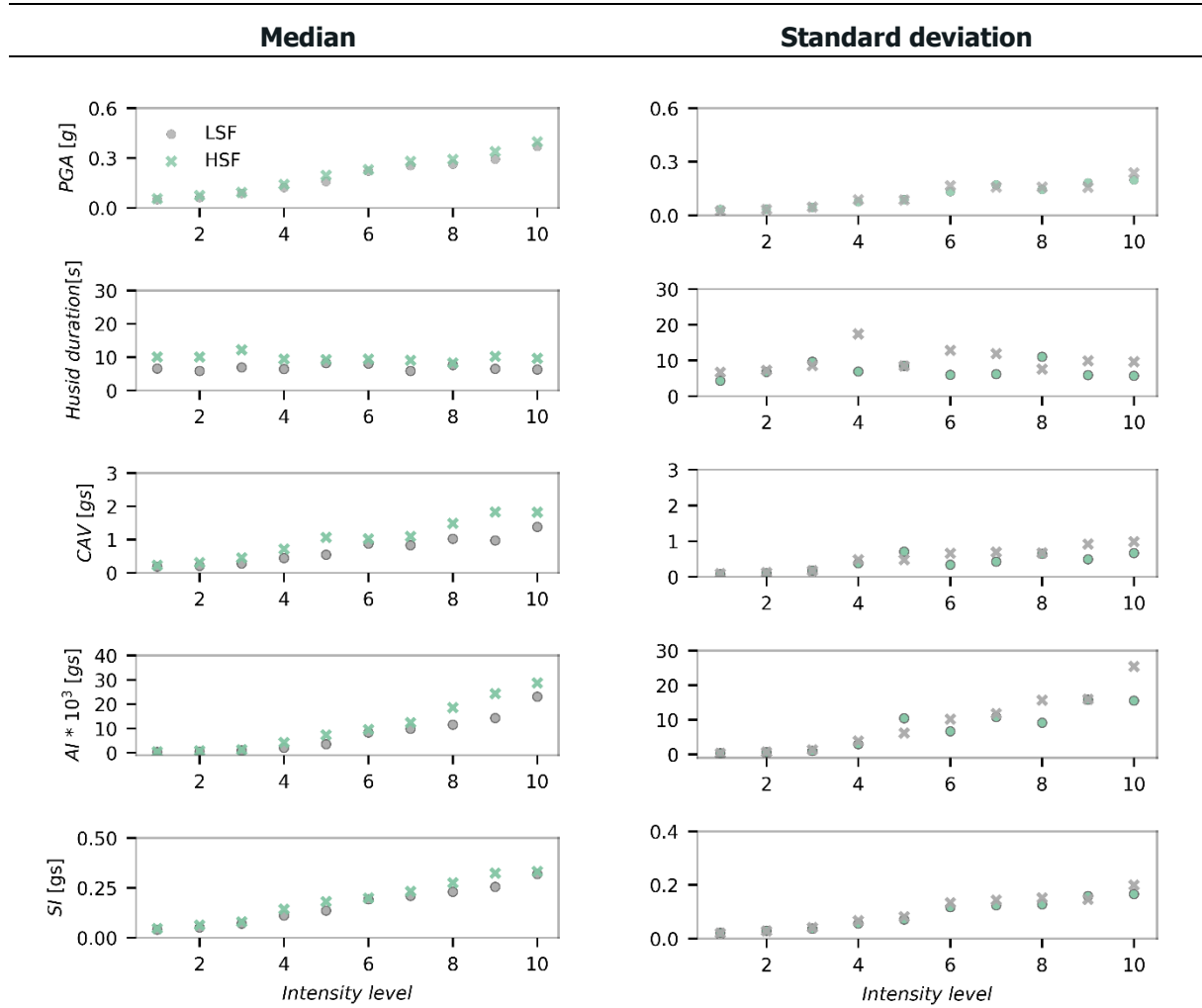


**Figure 34: Distribution of different  $IMs$ , namely peak ground acceleration ( $PGA$ ), Husid duration, Cumulative absolute velocity ( $CAV$ ), Arias intensity ( $AI$ ), and Spectral intensity ( $SI$ ), from first to the last row, respectively, in terms of median and standard deviation for the case of  $T=1s$ .**

### 3.2.4. Hazard consistent record selection accounting for duration and Arias intensity

The results discussed in the previous subsections imply that the differences observed in the fragility functions (i.e., higher probabilities for the group or records with high scaling factor; see Figure 32) might be due to the lack of sufficiency, i.e., the response of the considered systems does not depend solely on the spectral shape that is accounted for by the  $CS$ . For the case of a record set selected using  $T_1 = 0.2s$  and  $T_1 = 1s$  as the conditioning period, the  $CAV$  and  $AI$  show the most significant differences among considered  $IMs$ , while in the case of the  $T_1 = 2s$  duration varies the most. This implies that the response might be affected by the differences in these  $IMs$ . To confirm these assumptions, we select the records using the modified version of the  $CS$  that was altered by adding  $AI$ , in the case of  $T_1 = 0.2s$  and  $T_1 = 1s$  ( $CS(AI)$  in the following text), and  $D_{5-75}$ , in the case of  $T_1 = 2s$  ( $CS(D)$  in the following text), as an extra intensity measure to a vector of response spectral ordinates at different periods. In line with the previous sections, the quality of fit for the considered  $CS$  and  $AI$ (or  $D_{5-75}$ ) vector is assessed by means of the SSEs. In Figure 35 one can see that in the SSEs is below the 0.1 threshold for  $T_1 = 0.2s$  and  $T_1 = 1s$ , while for the  $T_1 = 2s$  there are some discrepancies for higher  $IMLs$ .

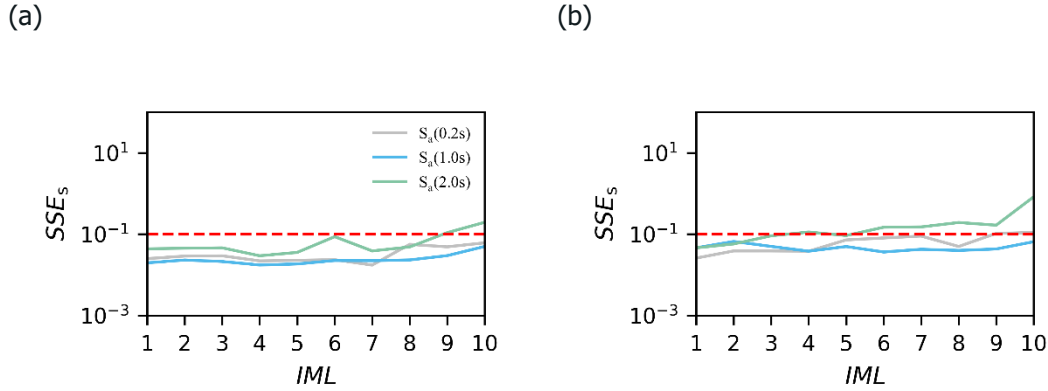


**Figure 35:  $SSE_s$  for the (a) LSF and (b) HSF records sets, selected using the modified  $CS$  that accounts for AI (i.e.,  $CS(AI)$ ), for different conditioning periods**

Figure 36 compares the fragility functions obtained with the  $CS$  and those obtained with  $CS(AI)$  for the  $T_1=0.2s$  for the three considered ductility levels. One can see that there are nearly no differences between the fragility curves of the LSF and HSF groups when selected with  $CS(AI)$ .

Similar trend is observed for SDOF with  $T_1=1s$ , as illustrated in Figure 37, where there are even smaller differences between the LSF and HSF group of the records selected with  $CS(AI)$ . These curves match the fragility curves obtained for LSF group selected with  $CS$ .

Lastly, in Figure 38, we compare the the fragility functions obtained with the  $CS$  and those obtained with  $CS(D)$  for SDOF with  $T_1=2s$  where one can see that the differences between the LSF and HSF are reduced when one uses  $CS(D)$ . The differences, however, still exist in this case, which might be due to either a poor match to the target spectrum (see Figure 35) or to the fact that other  $IM$ s beyond duration and spectral shape affect the system's response.

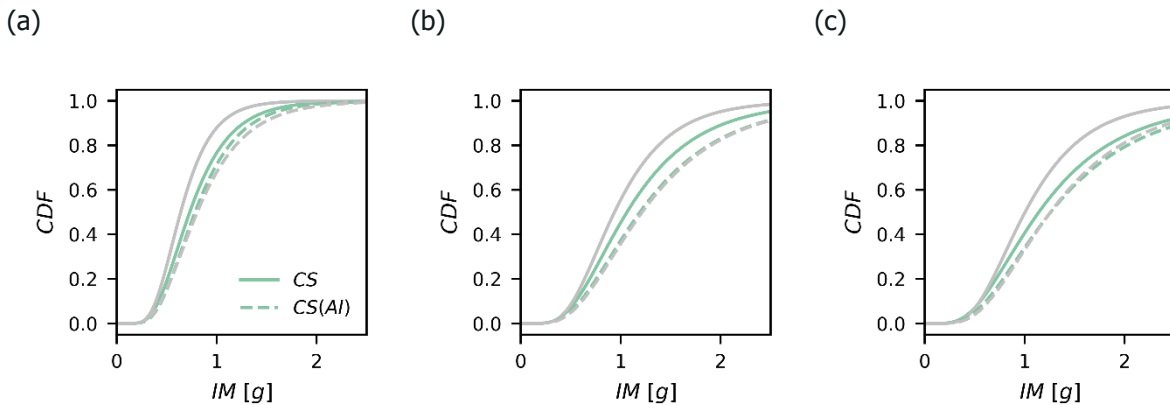


**Figure 36: Comparison between the fragility curves obtained from LSF (green line) and HSF (grey line) groups using  $CS$  and  $CS(AI)$  for ductility levels of: (a)  $\mu=2$ , (b)  $\mu=5$  and (c)  $\mu=8$ . Label on the x axis refers to  $S_a$  [g] at the fundamental period of the corresponding SDOF system, i.e.,  $S_a(T_1 = 0.2s)$ .**

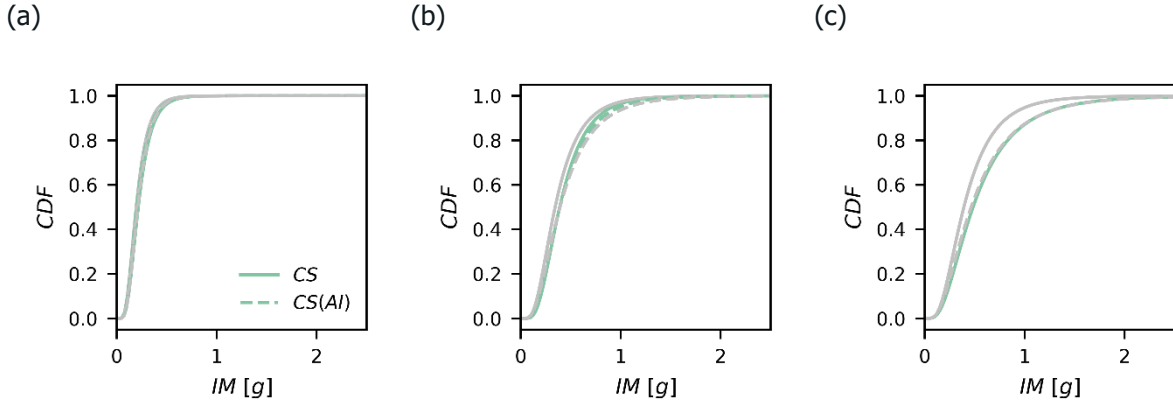


**Figure 37: Comparison between the fragility curves obtained from LSF (green line) and HSF (grey line) groups using  $CS$  and  $CS(AI)$  for ductility levels of: (a)  $\mu=2$ , (b)  $\mu=5$  and (c)  $\mu=8$ . Label on the x axis refers to  $S_a$  [g] at the fundamental period of the corresponding SDOF system, i.e.,  $S_a(T_1 = 1s)$ .**

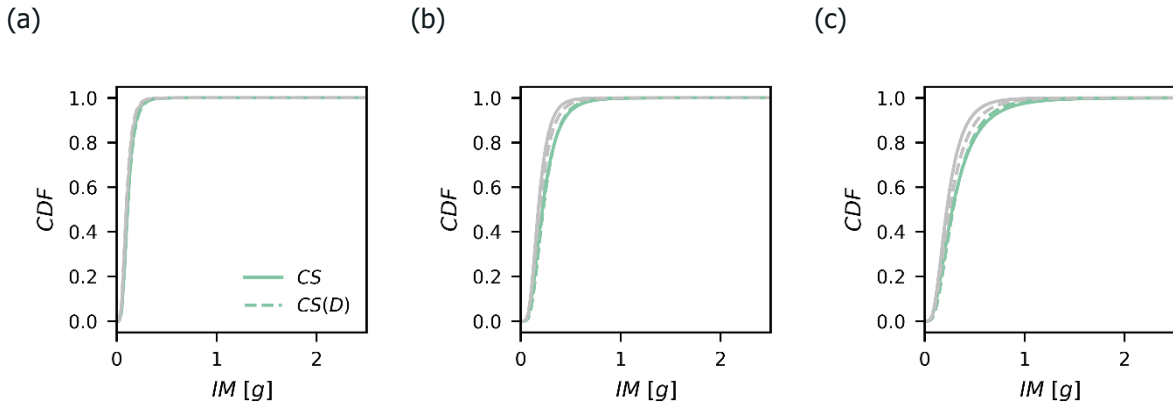


**Figure 38: Comparison between the fragility curves obtained from LSF (green line) and HSF (grey line) groups using  $CS$  and  $CS(D)$  for ductility levels of: (a)  $\mu=2$ , (b)  $\mu=5$  and (c)  $\mu=8$ . Label on the x axis refers to  $S_a$  [g] at the fundamental period of the corresponding SDOF system, i.e.,  $S_a(T_1 = 2s)$ .**

### 3.3. Synthetic ground motions for CS-based hazard

Ground motion simulation methodologies have been an active research field for over fifty years. Motivated by an ever-incomplete ground motion database and constantly improving knowledge on rupture and propagation mechanisms, such approaches show more and more promising results in the generation of nature-consistent ground motion time histories. This capacity to "mimic" nature-observed ground motions becomes especially useful in areas where certain events of interest have not yet been observed or measured. These methodologies, however, are still a simplified representation of a complex phenomenon and, therefore, they require validation before they can be confidently used in real-life engineering applications. On the other hand, recent investigations, i.e., (Hollender et al., 2020) show that recorded ground motion suffer in many cases from not fully controlled site conditions that can have non negligible impact on frequency content and bias the analysis.

This section presents the results obtained from the comparison of sets of recorded and simulated ground motions, obtained from the ESM database (Section 3.1.1) and the simulated database SDB (Section 3.1.2), respectively. Like the previous sections of this document, comparisons are made in terms of intensity measures of interest, and engineering demand parameters obtained from the response of SDOF systems for different intensity levels.

#### 3.3.1. Record sets and selection

We selected sets of 40 records from the ESM and SDB databases to be compatible with  $CS(Sa(T_1))$  for the site of interest in Perugia for all 10  $IMLs$  and three conditioning periods:  $T_1=0.2s$ ,  $T_1=1s$ , and  $T_1=2s$ . Minimum and maximum scaling factors of 0.25 and 6, respectively, were considered for this exercise. A more detailed description of this procedure is provided in Section 3.1.1 of this document.

Figure 39 shows the  $SSE_s$  error, calculated with Equation (3) for different conditioning periods. Same as for previous sections, the threshold of 0.1 is defined as an acceptable level of error. The figure shows that an adequate fit is obtained for all conditioning periods and  $IMLs$ , nevertheless, we observe that the error increases with the  $IML$ , as more extreme ground motions and events are required to fit the target  $CS$ .

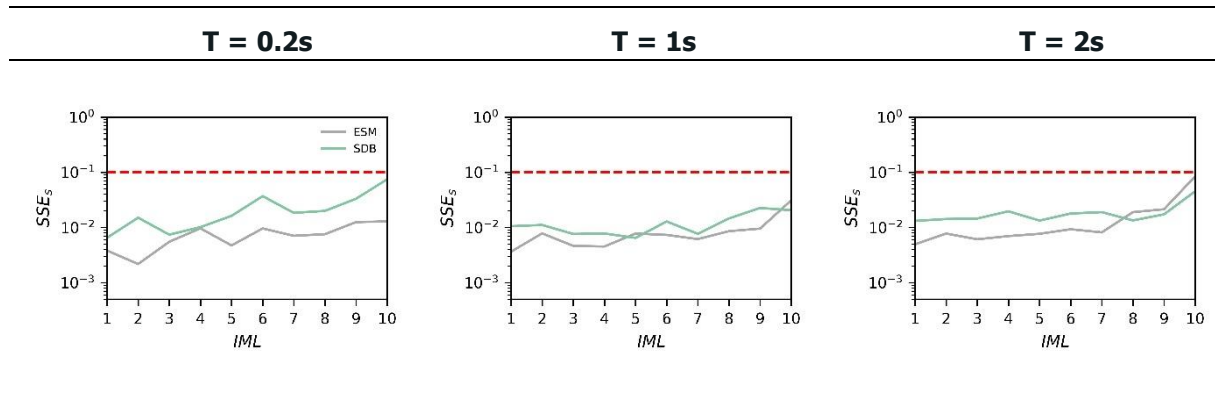


**Figure 39:  $SSE_s$  error for the LSF and HSF records sets and different conditioning periods**

We complement the evaluation of the record selection process by studying the distribution of magnitude ( $M_w$ ), soil shear velocity ( $V_{s30}$ ), and Joyner and Boore distance ( $R_{jb}$ ) for the two sets of records. The comparison of the causative parameters of the records selected for  $T_1=0.2s$  is shown in Figure 40. For this conditioning period, we observe similar distributions of  $M_w$  and  $R_{jb}$ , specifically in terms of median values (standard deviations are also comparable and the observed differences show no appreciable pattern). For  $V_{s30}$ , on the other hand, we observe a systematic difference for  $IMLs$  above 6. For these  $IMLs$ , the record selection process consistently selects scenarios with larger  $V_{s30}$  for the case of ESM (reaching a maximum difference in the median of 150 m/s). Considering that all other ground motion features are similar, this observation seems to indicate that site effects for the largest scenarios (required to fit this intensity level) may not be very well captured by the transfer functions considered in the construction of the SDB.



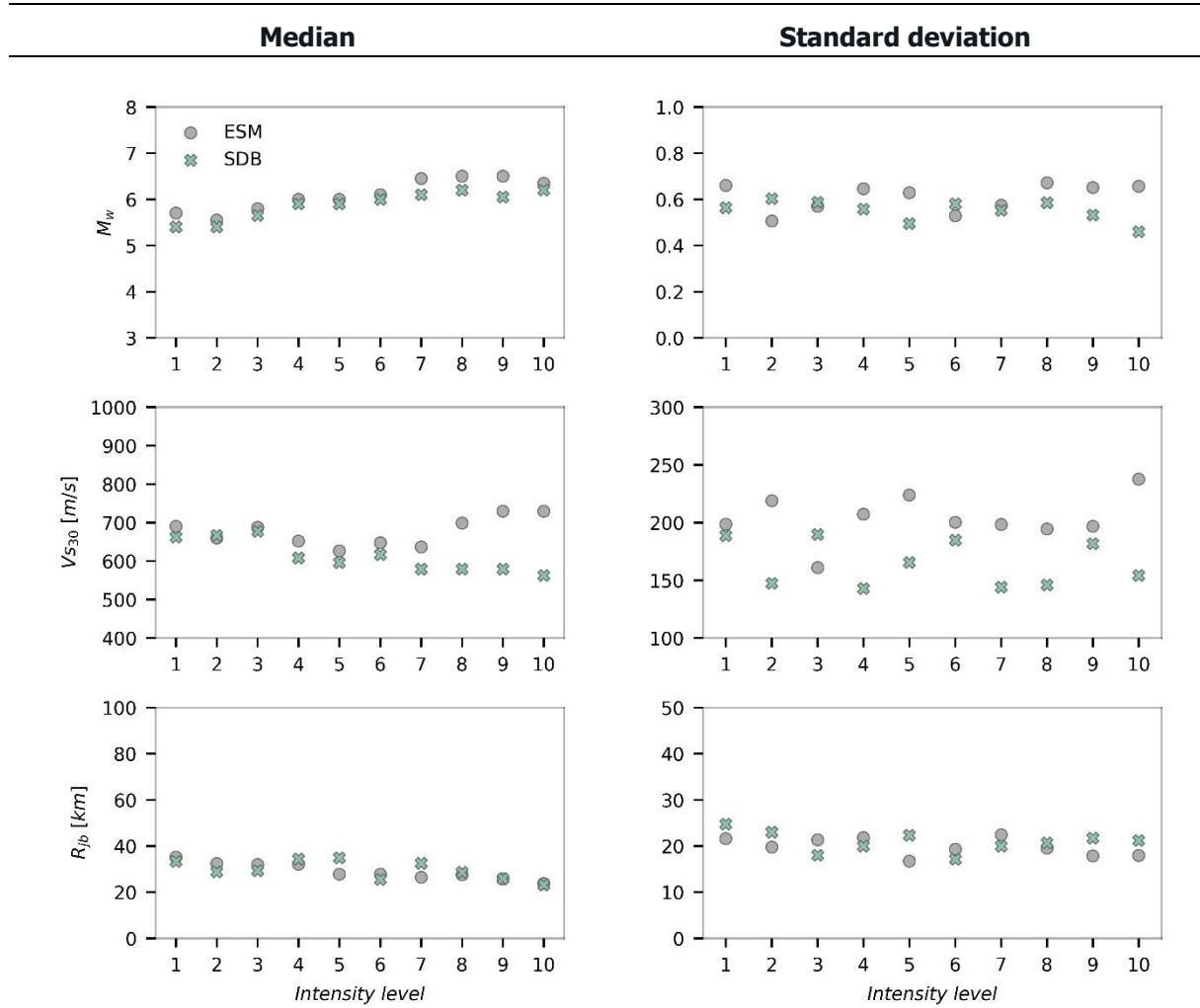


**Figure 40: Distribution of  $M_w$ ,  $V_{s30}$  and  $R_{jb}$  in terms of median and standard deviation for the case of  $T=0.2s$**

The comparison of ground motion features for  $T_1=1s$  is shown in Figure 41. Like the case of  $T_1=0.2s$ , we observe very similar distributions for  $M_w$  and  $R_{jb}$ . The comparison of the distributions of  $V_{s30}$ , on the other hand, does not present the systematic differences found for the higher  $IMLs$  and  $T_1=0.2s$ . Instead, we observe small differences showing no distinctive pattern. This observation seems to indicate that the differences in  $V_{s30}$  decrease with the spectral demand imposed by the target CS, and thus may be related to the amplitude of the ground motion. Further evidence of this is the fact that differences increase with the  $IML$ , as it may be noticed in Figure 40. We attribute these differences to the limitation of the considered site effects within our simulation scheme. These were computed considering a linear approach and hence we expect to see differences for the higher levels of ground motion amplitude, i.e. highest  $IML$  and for the 0.2s conditioning period (highest spectral acceleration, as shown in Table 3). Similar conclusions were drawn for the comparison of ground motion features for  $T_1=2s$  (not shown here).

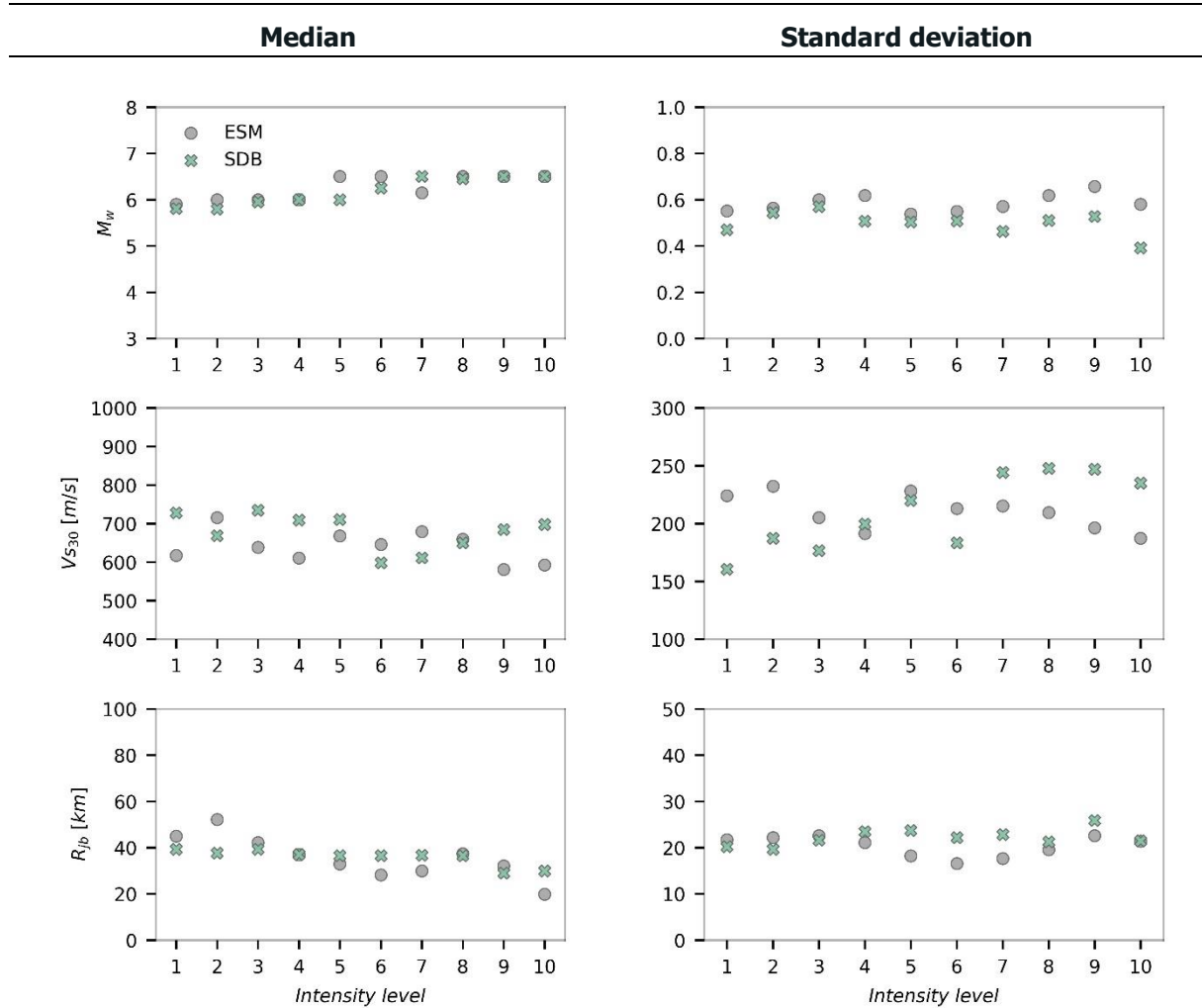


**Figure 41: Distribution of  $M_w$ ,  $V_{s30}$  and  $R_{jb}$  in terms of median and standard deviation for the case of  $T=1.0s$**

### 3.3.2. Distribution of IMs

Figure 42 shows the distribution of IMs for  $T_1=1s$ . This figure presents the median and standard deviation of the distributions for IMs other than spectral acceleration and not controlled by the *CS* record selection approach. Our results show a close fit for the median and standard deviation of *IMs* related to the spectral content of the ground motions, i.e., *PGA* and *SI*. The median of the distributions of the IMs related to duration of the ground motions show differences for *IMLs* above 6.0. As it can be seen in Figure 40 and Figure 41, these *IMLs* are related to the highest magnitude scenarios within the considered databases, thus indicating that the duration of these records was not very well captured during the calibration of the SGMSM for the selected scenarios. The differences in the distributions of these *IMs* are also noticeable in the comparison of standard deviations where the SDB-selected records show a consistently larger dispersion.

The differences in the duration related parameters were noticed to be not so important for the case of  $T_1=2s$  shown in Figure 43. Specifically, we noticed a closer match in terms of the standard deviation of the distributions of almost all considered *IMs*.

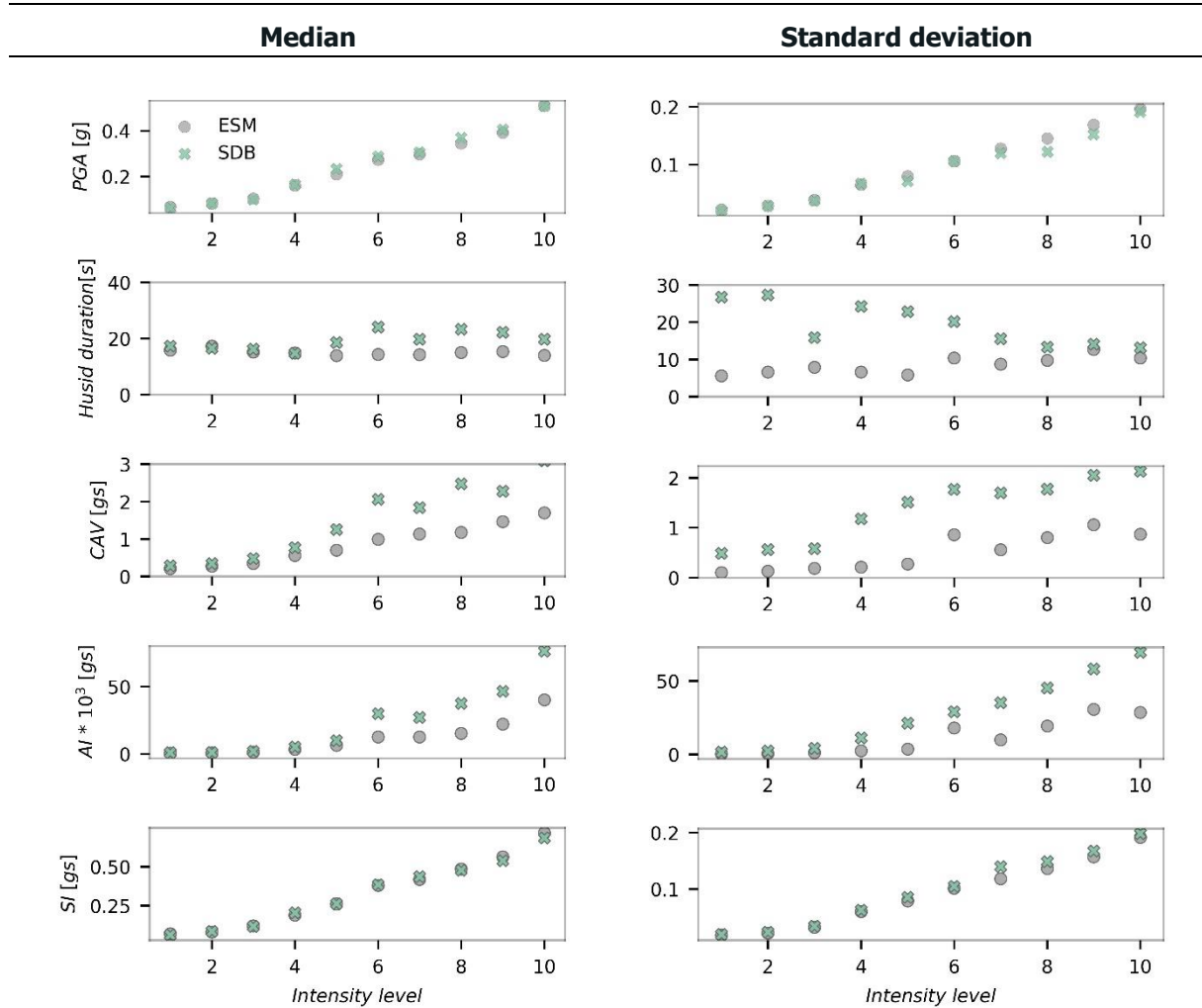


**Figure 42: Distribution of different IMs, namely peak ground acceleration (PGA), Husid duration, Cumulative absolute velocity (CAV), Arias intensity (AI), and Spectral intensity (SI), from first to the last row, respectively, in terms of median and standard deviation for the case of T=1s.**

It is important, to highlight a couple of aspects related to the discrepancies in the duration related IMs:

- i) From the definition of the weighting scheme used in the calibration procedure detailed in section 2.2, we recall the relative importance given to the spectral content over duration. In other words, if the procedure herein proposed is considered, the user can give priority to the fitting of specific IMs of interest during the calibration procedure, thus targeting specific uses for the simulated scenarios.
- ii) The number of events considered for the calibration of the group containing the largest magnitudes is the smallest within the reference ESM subset, thus limiting the available information for its characterization.
- Finally, iii) The use of transfer functions sampled only by  $V_{S30}$  does not guarantee similar changes in the phase of the ground motions. This is because different distributions of soil layers may result in comparable  $V_{S30}$  but completely different phase modifications, in other words,  $V_{S30}$  is not a sufficient variable to describe site effects.

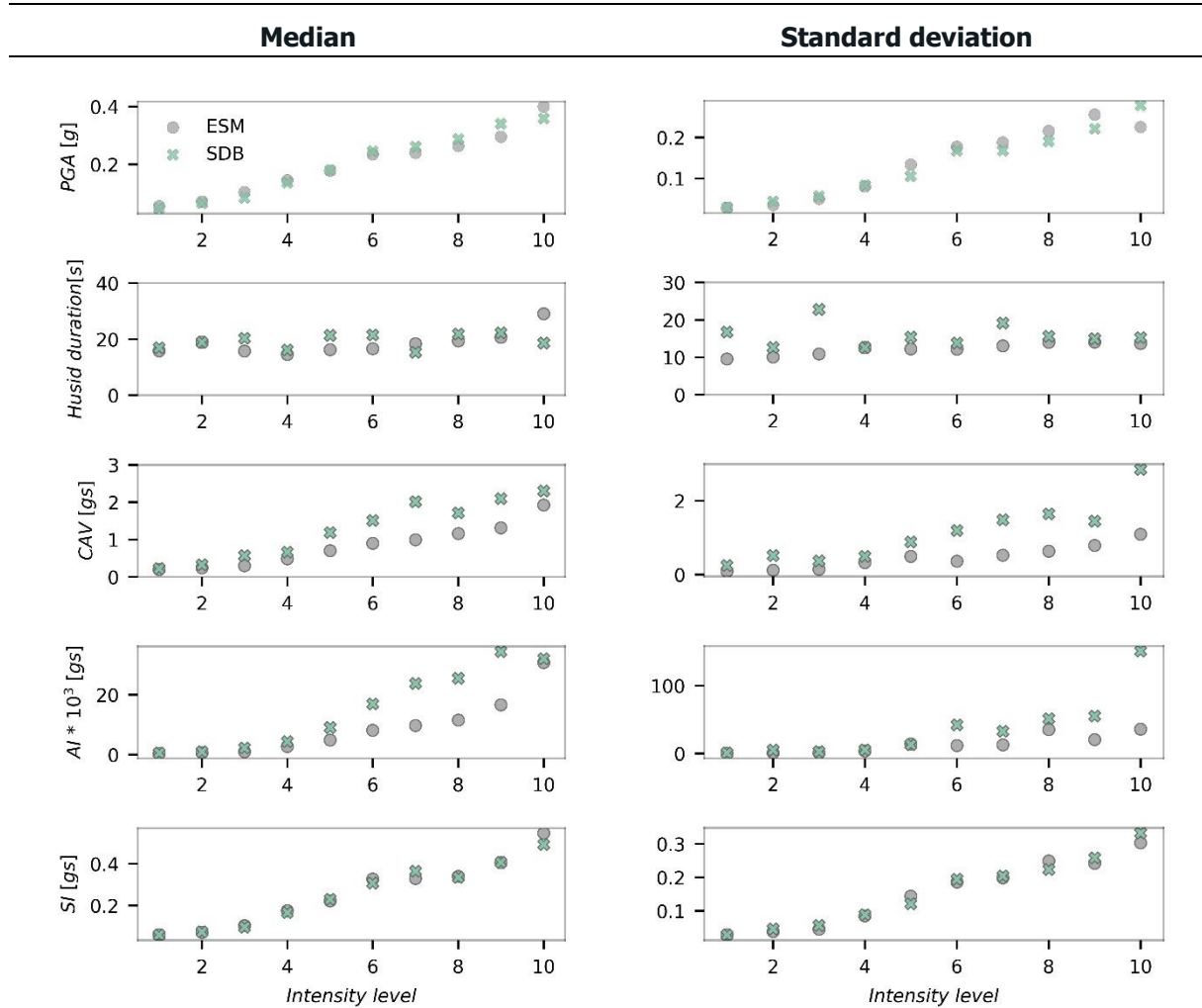


**Figure 43: Distribution of different IMs, namely peak ground acceleration (PGA), Husid duration, Cumulative absolute velocity (CAV), Arias intensity (AI), and Spectral intensity (SI), from first to the last row, respectively, in terms of median and standard deviation for the case of  $T=2s$ .**

To complement the previously discussed comparisons, we performed hypothesis tests across all *IMLs*, finding that the null hypothesis could not be rejected at the 5% significance for *PGA* and *SI* for all *IMLs*. In the case of *Husid duration* and *CAV*, the hypothesis was rejected for all *IMLs*. Finally, for *AI*, the hypothesis was rejected for *IMLs* above 4.

### 3.3.3. Structural Response

The comparison of the nonlinear time history analysis response of the SDOF systems is shown in Figure 44. The shown subfigures were generated with the same considerations as for the previous sections of this document. Overall, we observe very similar responses for the cases where the number of collapses allows the estimation of the different percentiles. We observed differences for the response of the  $T_1=2s$  system, specifically for the *IMLs* resulting in high ductility estimates, which may be caused by the limitation of the SGMSM to describe the long period range of ground motions [a constraint of stochastic simulation methodologies discussed in studies such as Otarola & Ruiz (2016) and Alvarez et al. (2022a)]. Furthermore, the period elongation experienced by the SDOF due to its inelastic response accentuates these discrepancies.

Additionally, we performed hypothesis tests across all EDPs and *IMLs*, finding that the null hypothesis could not be rejected at the 5% significance for all of the considered SDOFs and considered EDPs.

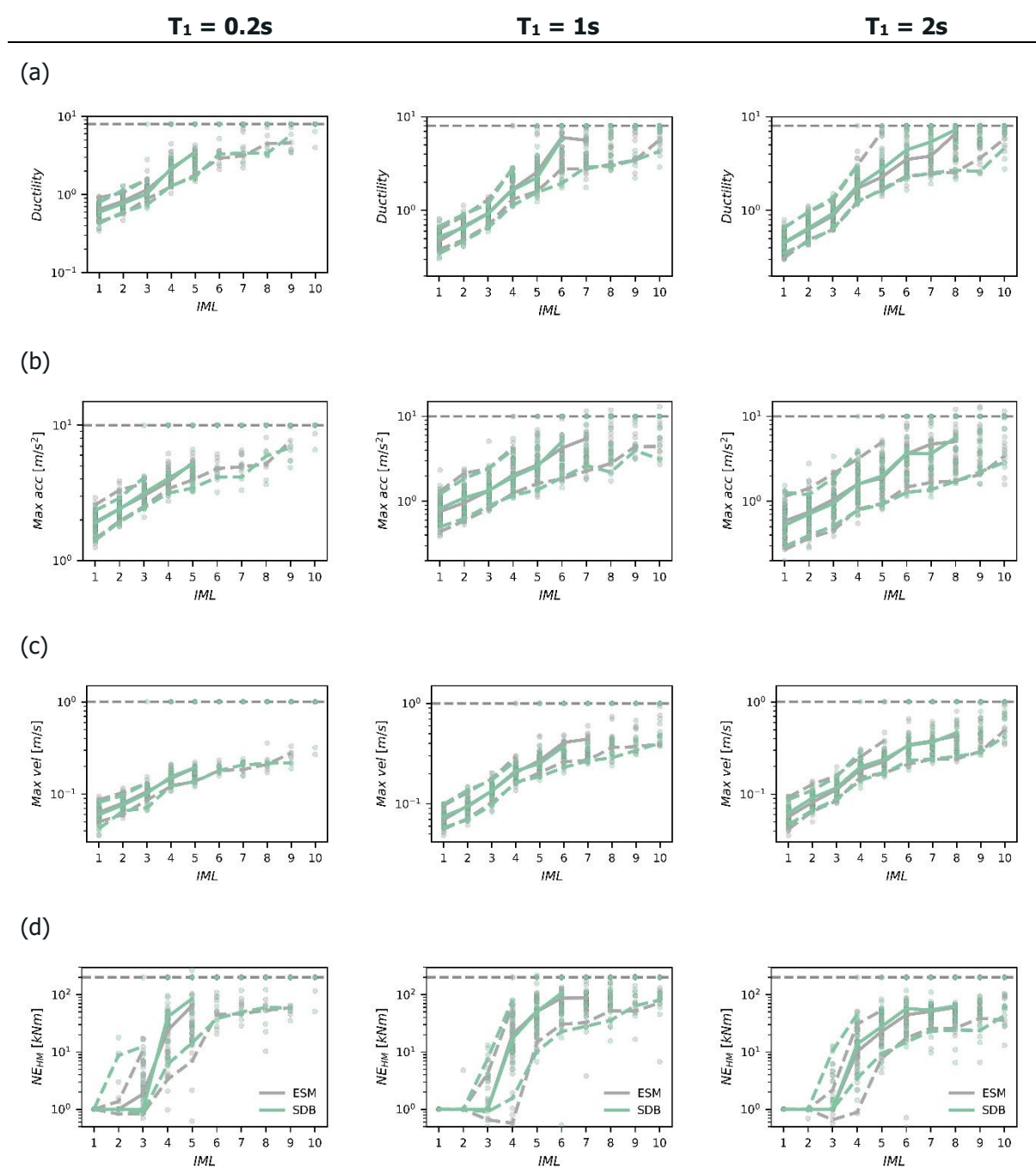


**Figure 44: Results of nonlinear time history analysis using 40 selected records at each IML, for the ESM and SDB sets of ground motions. Median is illustrated for different EDPs: (a) max ductility, (b) max acceleration, (c) max velocity, and (d) hysteretic energy. The dashed lines represent the 5<sup>th</sup> and 95<sup>th</sup> percentiles of the distributions**

Finally, Figure 45 shows the comparison of the fragility functions computed based on the probabilities of exceeding different ductility levels determined in previous sections of this report ( $\mu=2, 5$  and  $8$ ). Inspection of these figures shows that the curves describing the onset of damage are nearly identical for the two considered cases. This is expected as we focused our calibration of the SDB on the spectral content.

### D5.1 Methodology for selecting ensembles of rock-hazard consistent ground motions for fragility curve computations and datasets for WP6

For the case of  $T_1=0.2s$ , we observe differences in the median of the fragility curves for the major damage and collapse limit states. The capacity estimated from the response to the records select from the SDB database is lower than that of the ESM. This may be explained by the differences in the duration related IMs discussed in previous sections. Overall, the scenarios selected for the highest  $IMLs$  consistently show higher values of  $AI$  and  $Husid$  duration for the SDB-selected ground motions. A similar condition was also noticed for  $T_1=1s$ , where differences between this  $IMs$  is even larger. This is also the case for the major damage state for  $T_1=2s$ . However, fragility curves for the collapse limit state  $T_1=0.2s$  showed negligible differences, which could be explained by the similarity of the IMs selected for the highest  $IML$  of this system, not only in terms of their median but also of their standard deviation.

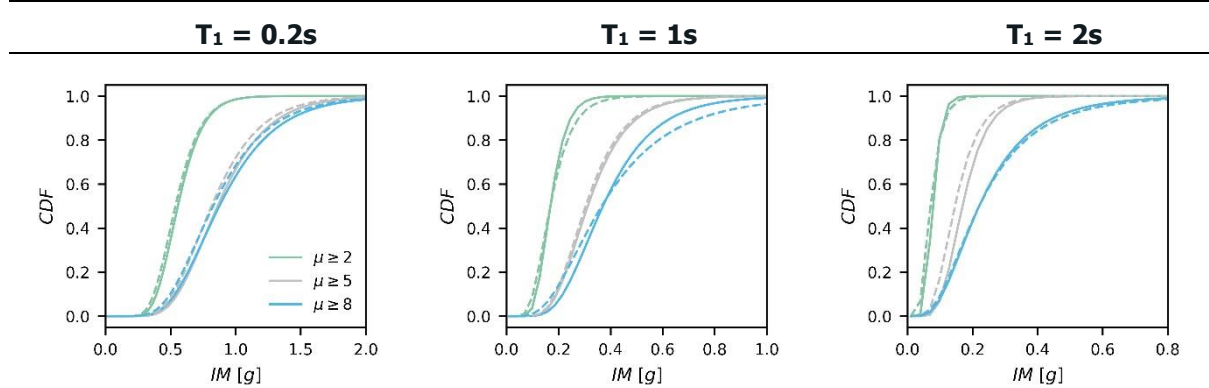


**Figure 45: Comparison between the fragility curves for three SDOFs obtained from ESM and SDB-selected records for: (a)  $\mu \geq 2$ , (b)  $\mu \geq 5$  and (c)  $\mu \geq 8$ . Label on the x axis refers to  $S_a$  [g] at the fundamental period of the corresponding SDOF system. Solid and dashed lines refer to the curves computed with the response from records selected from the ESM and SDB databases, respectively.**



## 4. Conclusions and recommendations

To support ground motion record selection in the METIS project, we assembled a database with a large number of real records from different available sources (i.e., the ESM, GNS, NESS, and NGA databases) that have been standardized and prepared for use. This final database encompasses events from several seismogenic sources and locations, improving the compatibility with a broad set of scenarios, intensities, and possible restrictions. Complementary to the real ground motions database, as part of WP4 we also developed a database of simulated ground motions to be utilized within the record selection procedure described in this document. The simulated database, called SDB, was constructed based on the calibration of the SGMSM for a subset of ground motions contained in the ESM database. The assembled SDB is overall consistent in terms of ground motion features, such as magnitude, source-to-site distance and hypocentral depth of the causative earthquakes and site conditions measured in terms of  $V_{S30}$ , with the ground motions in the reference subset of the ESM database.

We then performed an extensive set of tests to investigate if using records that are either recorded on soil stations (rather than rock ones), extensively scaled (rather than unscaled) or synthetic (rather than real) causes any bias in the structural response. The tests were applied to a case study in Perugia, Central Italy, for which the hazard was computed via OpenQuake. The structures were modelled as SDOF systems and OpenSees was utilized to perform nonlinear response analysis. We considered ten levels of ground motion intensity covering a values corresponding to a range of 0.2% to 70% poe in 50 years at the site. Records were selected using the *CS* approach for the three different cases considered: rock vs. soil, scale vs. unscaled, and real vs. synthetic ground motions. The tests were performed for a comprehensive group of SDOF systems with different fundamental periods and material models to cover a wide range of possible structures with different sensitivities. We first looked at the responses in terms of various EDPs that can be of interest for the SSCs considered in WP6. These EDPs were drift-based (i.e., ductility), acceleration-based, velocity-based, and energy-based (hysteretic energy dissipated). We then derived fragility curves for three different ductility levels (2, 5 and 8) that can correspond to the onset of damage, moderate damage and near collapse state, respectively. Lastly, in order to understand the differences in structural response better, we subjected the different record sets to seismological parameter comparisons, investigating the distribution of different *IMs* (i.e., *PGA*, *CAV*, Husid duration, *AI* and *SI*).

We showed that for the case of using soil recorded ground motions, most of the responses monitored did not show any significant differences in any *IML*, material model, or SDOF vibration period. The same can be said about the different intensity measures obtained through the seismological tests, except for the duration, which, as expected, was longer on soil records, but not by a significant amount. It should be noted that the groups formed exclusively by soil motions exhibited some bias in the fragility curves at the highest levels of damage, mainly due to the *IM* insufficiency, mismatch with the target spectra, and general uncertainty in estimating the response at high levels of inelastic displacement, a condition more evident in the elastic-hardening systems. This situation can be improved by a more adequate *IM* definition, as shown when using  $Sa(T_1)$  for the extreme periods, and by improving the match of the target spectra. Finally, given the scarcity of rock records and their generally 'less aggressive' spectral shape, selection of rock-exclusive ground motions while imposing strict parameters—both in site definition and limiting scaling factors—can result in a poor fit of the target spectrum and, thus, it can compromise the hazard consistency at the higher intensity levels.

Investigating the results of the sets of records with low (LSF) and high (HSF) scaling factors, we observed that the group with HSF always yields, on average, higher values of the different EDPs considered, but that these differences are not significant. Consequently, the HSF group of records produces higher exceedance probabilities for all ductility levels and SDOFs. To better understand the reasons behind this bias, we conducted a battery of seismological tests that showed some significant discrepancies in the values of duration, *AI* and *CAV*. We selected the records again, modifying the original *CS* method to account for these additional *IMs* and we showed that the bias caused by excessive scaling is considerably reduced by accounting for the duration in the case of SDOF with  $T_1 = 2s$  and by accounting for *AI* in the case of SDOF with  $T_1 = 0.2s$  and with  $T_1 = 1s$ .

The selection of ground motions from recorded and simulated databases resulted in comparable distributions of causative parameters for all *IMLs* and SDOF systems. More specifically, no important



differences were noticed in terms of magnitude ( $M_w$ ) or distance ( $R_{jb}$ ). A systematic underestimation of  $V_{S30}$  was noticed, however, for records selected for the SDOF with  $T_1 = 0.2s$  and for the highest *IML*. This range of scenarios corresponds to the largest ground motion intensities within the considered databases. Thus, these discrepancies may indicate that the transfer functions considered in the inclusion of the side effects could not be adequate for this range of scenarios where key issues such as nonlinear response (not modeled) may be crucial for the assessment of the response. From the comparison of IMs of the sets of selected records, we observed a very close fit for the spectral quantities, which were prioritized in the calibration procedure, yet not so much for the duration-related IMs such as CAV and Husid durations. These results may be improved by considering different weighting schemes during the calibration procedure.

From the comparison of responses we observed identical distributions for cases where the number of collapses allows for the computation of the compared statistical percentiles. Some slight differences, however, were noticed in the dissipated energy. These differences may be explained by the dissimilarities in the duration related IMs of the selected records, not only in terms of median but of dispersion, as measured by the standard deviation. The comparison of fragility curves revealed that for the onset of damage limit state the SDB-selected records result in identical responses to that of the ESM-selected records. This is expected as the SGMSM was calibrated to match (on average) the spectral content of the reference ESM subset, and the spectral acceleration at the period of vibration is a sufficient IM to describe the near-elastic response of an SDOF system. Some differences, however, were noticed in the moderate damage and collapse fragility curves. As mentioned in previous sections, these differences may be explained by the discrepancies in the distributions of duration and energy content of the selected synthetic and real ground motions. These differences may impact the severe responses caused by the high-amplitude ground motions.

One should note, however, that all these analyses represent a 'worst-case scenario' since the groups tested were composed, by design, of extreme cases. In real applications, record selection would be made by combining, say, low-scaled and high-scaled records or rock and soil records and this mixing would reduce the slight bias found on the analysis even further. Finally, note that the SDOF systems used here may or may not be appropriate for the SSCs considered in METIS, whose response may be monitored via EDPs not considered here. Hence, when more detailed information about SSCs and EDPs utilized to gauge their performance, including threshold values for damage states of interest, becomes available, the analyses shown here could be more accurately tailored. Nonetheless, the extensive set of systems and EDPs tested here seems to point out that, as long hazard consistency is carefully enforced via a *CS* – method, these additional motions can be adequate for assessing structural responses not significantly in the post-elastic range. However, this is hardly a significant limitation for SSCs of nuclear power plants, which are designed to remain linear elastic for extreme levels of ground motions. On the other hand, the abundance of higher modes in NPPs may offer new challenges.

## 5. Acknowledgments

We want to thank Maria Lancieri for sharing the scripts for processing and calculating the various intensity measures used in the seismological testing of the different sets of ground motions and for downloading the data from the ESM database. Furthermore, her valuable suggestions and comments that improved the quality of this study are gratefully acknowledged. We are also grateful for the insightful comments of Prof. Vamvatsikos and of Dr. Zentner that improved the quality of this report.

## 6. Bibliography

- Afshari, K., & Stewart, J. P. (2016). Physically parameterized prediction equations for significant duration in active crustal regions. *Earthquake Spectra*, 32(4), 2057–2081. <https://doi.org/10.1193/063015EQS106M>
- Alvarez, L., Bonilla, L. F., Bazzurro, P., Aochi, H., Zenter, I., & Senfaunte, G. (2022a). 3D Stochastic Ground Motion Prediction of an earthquake scenario. (*In Process*).
- Alvarez, L., Bonilla, L. F., Bazzurro, P., Aochi, H., Zenter, I., & Senfaunte, G. (2022b). Assessment of a 3D Stochastic Ground Motion Simulation Methodology. (*In Process*).

# D5.1 Methodology for selecting ensembles of rock-hazard consistent ground motions for fragility curve computations and datasets for WP6

- Ancheta, T. D., Darragh, R. B., Stewart, J. P., Seyhan, E., Silva, W. J., Chiou, B. S. J., Wooddell, K. E., Graves, R. W., Kottke, A. R., Boore, D. M., Kishida, T., & Donahue, J. L. (2014). NGA-West2 database. *Earthquake Spectra*, 30(3), 989–1005. <https://doi.org/10.1193/070913EQS197M>
- Baker, J. W., & Cornell, C. A. (2006). Spectral shape, epsilon and record selection. *Earthquake Engineering and Structural Dynamics*, 35(9), 1077–1095. <https://doi.org/10.1002/eqe.571>
- Baker, J. W. (2007). Measuring bias in structural response caused by ground motion scaling. *Pacific Conference on Earthquake Engineering*, 056, 1–6. <https://doi.org/10.1002/eqe>
- Baker, J. W., & Jayaram, N. (2008). Correlation of spectral acceleration values from NGA ground motion models. *Earthquake Spectra*, 24(1), 299–317. <https://doi.org/10.1193/1.2857544>
- Baker, J. W. (2011). Conditional mean spectrum: Tool for ground-motion selection. *Journal of Structural Engineering*, 137(3), 322–331. [https://doi.org/10.1061/\(ASCE\)ST.1943-541X.0000215](https://doi.org/10.1061/(ASCE)ST.1943-541X.0000215)
- Baker, J. W., & Lee, C. (2018). An Improved Algorithm for Selecting Ground Motions to Match a Conditional Spectrum. *Journal of Earthquake Engineering*, 22(4), 708–723. <https://doi.org/10.1080/13632469.2016.1264334>
- Bard, P., Duval, A., Koehler, A., & Rao, S. (2004). *SESAME European research project. D23.12* (December), 62 pp. <http://sesame-fp5.obs.ujf-grenoble.fr/index.htm>
- Bazzurro, P., & Cornell, C. A. (1999). Disaggregation of seismic hazard. *Bulletin of the Seismological Society of America*, 89(2), 501–520.
- Bazzurro, P., & Cornell, C. A. (2002). Vector-valued probabilistic seismic hazard analysis (VPSHA). *7th U.S National Conference on Earthquake Engineering, Boston, MA, July 21-25*.
- Bazzurro, P., Kohrangi, M., Bakalis, K., & Vamvatsikos, D. (2020). Bi-directional conditional-spectra-based record selection for horizontal and vertical ground motions. *17th World Conference on Earthquake Engineering, 17WCEE*.
- Bindi, D., Pacor, F., Luzi, L., Puglia, R., Massa, M., Ameri, G., & Paolucci, R. (2011). Ground motion prediction equations derived from the Italian strong motion database. *Bulletin of Earthquake Engineering*, 9(6), 1899–1920. <https://doi.org/10.1007/s10518-011-9313-z>
- Bindi, D., Zaccarelli, R., Strollo, A., & Di Giacomo, D. (2019). Harmonized local magnitude attenuation function for Europe using the European Integrated Data Archive (EIDA). *Geophysical Journal International*, 218(1), 519–533. <https://doi.org/10.1093/gji/ggz178>
- Bindi, Dino, & Kotha, S. R. (2020). Spectral decomposition of the Engineering Strong Motion (ESM) flat file: regional attenuation, source scaling and Arias stress drop. *Bulletin of Earthquake Engineering*, 18(6), 2581–2606. <https://doi.org/10.1007/s10518-020-00796-1>
- Bojórquez, E., & Iervolino, I. (2011). Spectral shape proxies and nonlinear structural response. *Soil Dynamics and Earthquake Engineering*, 31(7), 996–1008. <https://doi.org/10.1016/j.soildyn.2011.03.006>
- Boore, D. M. (1983). Stochastic simulation of high-frequency ground motions based on seismological models of the radiated spectra. *Bulletin of Seismological Society of America*, 73(6), 1865–1894.
- Boore, D. M., & Joyner, W. B. (1997). Site amplifications for generic rock sites. *Bulletin of the Seismological Society of America*, 87(2), 327–341. <https://doi.org/10.1785/bssa0870020327>
- Boore, D. M. (2003). Simulation of Ground Motion Using the Stochastic Method. *Pure and Applied Geophysics*, 160, 635–676.
- Boore, D. M., & Atkinson, G. M. (2008). Ground-motion prediction equations for the average horizontal component of PGA, PGV, and 5%-damped PSA at spectral periods between 0.01 s and 10.0 s. *Earthquake Spectra*, 24(1), 99–138. <https://doi.org/10.1193/1.2830434>
- Bradley, B. A. (2010). A generalized conditional intensity measure approach and holistic ground-motion selection. *Earthquake Engineering & Structural Dynamics*, 39, 1321–1342. <https://doi.org/10.1002/eqe>
- Bradley, B. A. (2011). Correlation of significant duration with amplitude and cumulative intensity

- measures and its use in ground motion selection. *Journal of Earthquake Engineering*, 15(6), 809–832. <https://doi.org/10.1080/13632469.2011.557140>
- Brendon A. Bradley. (2013). A comparison of intensity-based demand distributions and the seismic demand hazard for seismic performance assessment. *Earthquake engineering and structural dynamics*, Vol. 42, pp. 2235–2253
- CEN. European Standard EN 1998-1. Eurocode 8: Design of structures for earthquake resistance. Part 1: General rules, seismic actions and rules for buildings. European Committee for Standardization, Brussels, Belgium, 2004.
- Chandramohan R, Baker JW and Deierlein GG (2016) *Quantifying the influence of ground motion duration on structural collapse capacity using spectrally equivalent records*. *Earthquake Spectra* 32: 927–950.
- Conte, J. P., & Peng, B. . F. (1997). Fully Nonstationary Analytical Earthquake Ground-Motion Model. *Journal of Engineering Mechanics*, pp. 15-24.
- Cordova, P. P., Deierlein, G. G., Mehanny, S. S., Cornell, C. A. (2000). "Development of a two parameter seismic intensity measure and probabilistic assessment procedure." The Second U.S.- Japan Workshop on Performance-Based Earthquake Engineering Methodology for Reinforced Concrete Building Structures, Sapporo, Hokkaido, 187–206.
- Cornell, C. A., & Krawinkler, H. (2000). *Progress and challenges in seismic performance assessment* (pp. 1–3). PEER Center News, 3. <https://apps.peer.berkeley.edu/news/2000spring/performance.html>
- Dávalos, H., & Miranda, E. (2019). Evaluation of bias on the probability of collapse from amplitude scaling using spectral-shape-matched records. *Earthquake Engineering and Structural Dynamics*, 48(8), 970–986. <https://doi.org/10.1002/eqe.3172>
- De Biasio, M., Grange, S., Dufour, F., Allain, F., and Petre-Lazar, I., 2014. A simple and efficient intensity measure to account for nonlinear structural behavior. *Earthquake Spectra*, 30(4), 1403–1426. DOI: 10.1193/010614EQS006M
- FEMA 274 (1997). NEHRP Commentary on the Guidelines for the Seismic Rehabilitation of Buildings. *Federal Emergency Management Agency, Washington, DC, Developed by the Applied Technology Council, October*.
- Hollender, F. & Roumelioti, Z. & Maufroy, E. & Traversa, P. & Mariscal, A.. (2020). Can We Trust High-Frequency Content in Strong-Motion Database Signals? Impact of Housing, Coupling, and Installation Depth of Seismic Sensors. *Seismological Research Letters*. 91(4):2192–205. <https://doi.org/10.1785/0220190163>.
- Jayaram, N., & Baker, J. W. (2008). Statistical tests of the joint distribution of spectral acceleration values. *Bulletin of the Seismological Society of America*, 98(5), 2231–2243. <https://doi.org/10.1785/0120070208>
- Jayaram, N., Lin, T., & Baker, J. W. (2011). A Computationally efficient ground-motion selection algorithm for matching a target response spectrum mean and variance. *Earthquake Spectra*, 27(3), 797–815. <https://doi.org/10.1193/1.3608002>
- Kaiser, A., Van Houtte, C., Perrin, N., Wotherspoon, L., & McVerry, G. (2017). Site characterisation of GeoNet stations for the New Zealand Strong Motion Database. *Bulletin of the New Zealand Society for Earthquake Engineering*, 50, 39–49. <https://doi.org/10.5459/bnzsee.50.1.39-49>
- Kazantzi, A. K., & Vamvatsikos, D. (2015). *Intensity measure selection for vulnerability studies of building classes*. *Earthq Eng Struct Dyn* 2015;44:2677–94. <https://doi.org/10.1002/eqe.2603>
- Kohrangi, M., Bazzurro, P., & Vamvatsikos, D. (2016). Vector and scalar IMs in structural response estimation, Part II: Building demand assessment. *Earthquake Spectra*, 32(3), 1525–1543. <https://doi.org/10.1193/053115EQS081M>
- Kohrangi, M., Bazzurro, P., Vamvatsikos, D., & Spillatura, A. (2017a). Conditional spectrum-based ground motion record selection using average spectral acceleration. *Earthquake Engineering & Structural Dynamics Earthquake*. <https://doi.org/10.1002/eqe.2876>

## D5.1 Methodology for selecting ensembles of rock-hazard consistent ground motions for fragility curve computations and datasets for WP6

- Kohrangi, M., Vamvatsikos, D., & Bazzurro, P. (2017b). A record selection methodology for vulnerability functions consistent with regional seismic hazard for classes of buildings. *16th World Conference on Earthquake - 16WCEE*.
- Kohrangi, M., Bazzurro, P., & Vamvatsikos, D. (2019). Conditional spectrum bidirectional record selection for risk assessment of 3D structures using scalar and vector IMs. *Earthquake Engineering and Structural Dynamics*, 48(9), 1066–1082. <https://doi.org/10.1002/eqe.3177>
- Kohrangi, M., Papadopoulos, A. N., Bazzurro, P., & Vamvatsikos, D. (2020). Correlation of spectral acceleration values of vertical and horizontal ground motion pairs. *Earthquake Spectra*. <https://doi.org/10.1177/8755293020919416>
- Lanzano, G., Felicetta, C., Pacor, F., Spallarossa, D., & Traversa, P. (2020). Methodology to identify the reference rock sites in regions of medium-to-high seismicity: an application in Central Italy. *Geophysical Journal International Electronic*, 222(3), 2053–2067. <https://doi.org/10.1093/gji/ggaa261>
- Lanzano, G., Sgobba, S., Luzi, L., Puglia, R., Pacor, F., Felicetta, C., D'Amico, M., Cotton, F., & Bindi, D. (2019). The pan-European Engineering Strong Motion (ESM) flatfile: compilation criteria and data statistics. *Bulletin of Earthquake Engineering*, 17(2), 561–582. <https://doi.org/10.1007/s10518-018-0480-z>
- Laurendeau, A., Bard, P. Y., Hollender, F., Perron, V., Foundotos, L., Ktenidou, O. J., & Hernandez, B. (2018). Derivation of consistent hard rock ( $1000 < VS < 3000$  m/s) GMPEs from surface and down-hole recordings: analysis of KiK-net data. *Bulletin of Earthquake Engineering*, 16(6), 2253–2284. <https://doi.org/10.1007/s10518-017-0142-6>
- Lin, T., Harmsen, S. C., Baker, J. W., & Luco, N. (2013a). Conditional spectrum computation incorporating multiple causal earthquakes and ground-motion prediction models. *Bulletin of the Seismological Society of America*, 103(2 A), 1103–1116. <https://doi.org/10.1785/0120110293>
- Lin, T., Haselton, C. B., & Baker, J. W. (2013b). Conditional spectrum-based ground motion selection. Part I: Hazard consistency for risk-based assessments. *Earthquake Engineering & Structural Dynamics*, 42, 1847–1865. <https://doi.org/10.1002/eqe>
- Luco, N., & Bazzurro, P. (2007). Does amplitude scaling of ground motion records result in biased nonlinear structural drift responses? *Earthquake Engineering and Structural Dynamics*, 36, 1813–1835.
- McGuire, R. K. (2004). Seismic hazard and risk analysis, EERI Monograph MNO-10, Earthquake Engineering Research Institute, Oakland, California. ISBN-13:978-0943198019
- McKenna, F., Fenves, G. L., B, J., & Scott M. (2000). *Open system for earthquake engineering simulation*. <http://opensees.berkeley.edu>
- Motazedian, D., & Atkinson, G. M. (2005). Stochastic finite-fault modeling based on a dynamic corner frequency. *Bulletin of the Seismological Society of America*, 95(3), 995–1010. <https://doi.org/10.1785/0120030207>
- National Research Institute for Earth Science and Disaster Resilience (2019), NIED K-NET, KiK-net, National Research Institute for Earth Science and Disaster Resilience, doi:10.17598/NIED.0004
- Norme Tecniche per le Costruzioni (NTC), 2008. Norme Tecniche per le Costruzioni, Decree of the Minister of the Infrastructures, 14 January 2008, Italian Official Gazette no. 29 of 4 February 2008. (n.d.).
- Otarola, C. L., & Ruiz, S. (2016). Stochastic Generation of Accelerograms for Subduction Earthquakes. *Bulletin of the Seismological Society of America*, 106(6). <https://doi.org/10.1785/0120150262>
- Pagani, M., Monelli, D., Weatherill, G., Danciu, L., Crowley, H., Henshaw, P., Butler, L., Nastasi, M., Panzeri, L., Simionato, M., & Vigano, D. (2014). OpenQuake Engine: An Open Hazard ( and Risk ) Software for the Global Earthquake Model. *Seismological Research Letters*, 85(3), 692–702. <https://doi.org/10.1785/0220130087>



## D5.1 Methodology for selecting ensembles of rock-hazard consistent ground motions for fragility curve computations and datasets for WP6

- Paolucci, R. (2002). Amplification of earthquake ground motion by steep topographic irregularities. *Earthquake Engineering and Structural Dynamics*, 31(10), 1831–1853. <https://doi.org/10.1002/eqe.192>
- Papageorgiou, B. Y. A. S., & Aki, K. (1983). A specific barrier model for the quantitative description of inhomogeneous faulting and the prediction of strong ground motion. I. description of the model. *Bulletin of the Seismological Society of America*, 73(3), 693–722. <https://doi.org/10.1086/622062>
- Pilz, M., Cotton, F., Zaccarelli, R., & Bindi, D. (2019). Capturing regional variations of hard-rock attenuation in Europe. *Bulletin of the Seismological Society of America*, 109(4), 1401–1418. <https://doi.org/10.1785/0120190023>
- Pousse, G., Bonilla, L. F., Cotton, F., & Margerin, L. (2006). Nonstationary Stochastic Simulation of Strong Ground Motion Time Histories Including Natural Variability: Application to the K-Net Japanese Database. *Bulletin of the Seismological Society of America*, 96(6), 2103–2117. <https://doi.org/10.1785/0120050134>
- Sabetta, F., & Pugliese, A. (1996). Estimation of response spectra and simulation of nonstationary earthquake ground motions. *Bulletin of the Seismological Society of America*, 86(2), 337–352.
- Sabetta, F., Pugliese, A., Fiorentino, G., & Lanzano, G. (2021). Simulation of non-stationary stochastic ground motions based on recent Italian earthquakes. *Bulletin of Earthquake Engineering*. <https://doi.org/10.1007/s10518-021-01077-1>
- Sgobba, S., Felicetta, C., Lanzano, G., Ramadan, F., & Amico, M. D. (2021). *NESS2 . 0: An Updated Version of the Worldwide Dataset for Calibrating and Adjusting Ground- Motion Models in Near Source*. 111(5), 2358–2378. <https://doi.org/10.1785/0120210080>
- Shome, N., Cornell, C.A. (1999) "Probabilistic seismic demand analysis of nonlinear structures," Report No. RMS-35., John A. Blume Earthquake Engineering Centre, Department of Civil and Environmental Engineering Stanford University
- Spillatura, A., Kohrangi, M., Bazzurro, P., & Vamvatsikos, D. (2021). Conditional spectrum record selection faithful to causative earthquake parameter distributions. *Earthquake Engineering and Structural Dynamics*, 50(10), 2653–2671. <https://doi.org/10.1002/eqe.3465>
- Stewart, J. P., Shyh-Jeng Chiou, Graves, R. W., Somerville, P. G., & Abrahamson, N. (2001). Ground Motion Evaluation Procedures for Performance-Based Design - PEER report 2001/09. *Pacific Earthquake Engineering Research Center, University of California, Berkeley, September 2001*.
- Tarballi, K., & Bradley, B. A. (2016). The effect of causal parameter bounds in PSHA-based ground motion selection. *Earthquake Engineering and Structural Dynamics*, 45(9), 1515–1535. <https://doi.org/10.1002/eqe.2721>
- Van Houtte, C., Bannister, S., Holden, C., Bourguignon, S., & McVerry, G. (2017). The New Zealand strong motion database. *Bulletin of the New Zealand Society for Earthquake Engineering*, 50(1), 1–20. <https://doi.org/10.5459/bnzsee.50.1.1-20>
- Wells, D. L., & Coppersmith, K. J. (1994). New empirical relationships among magnitude, rupture length, rupture width, rupture area, and surface displacement. *Bulletin - Seismological Society of America*, 84(4), 974–1002.